Università degli studi di Genova
Facoltà di scienze Matematiche, Fisiche e Naturali
Scuola di Dottorato in Scienze e Tecnologie
per l'informazione e la conoscenza
XXIV Ciclo, A.A. 2009 - 2011

A Thesis submitted for the degree of
Dottore di Ricerca

The road to the CUORE experiment: research and development for an extremely low background bolometer array

School Coordinator
Prof. Lorenzo Mattera
Università di Genova

Author
Lucia Canonica
Università e sezione INFN di Genova

Advisor
Prof. Marco Pallavicini
Università e sezione INFN di Genova

External Advisor
Prof.ssa Chiara Brofferio
Università e sezione INFN di Milano Bicocca

Area 02 - Scienze Fisiche

Contents

Introduction

The neutrino existence was first postulated in 1930 by Wolfgang Pauli in a famous letter addressed to the *Liebe Radioacktive Damen und Herren*[1], as a "*desperate way out*" to explain the reason why the electrons in beta decay were not emitted with the full reaction energy of the nuclear transition. Pauli, saying "*I have done a terrible thing. I have postulated a particle that cannot be detected*" was somehow concerned for the difficulty of an experimental confirmation of the existence of a neutrally charged particle with no mass. Neutrinos were experimentally detected for the first time 25 years later, when the inverse beta decay produced by anti-neutrino interactions was observed in the Savannah River Experiment by Reines and Cowan. During the past decades, the research in the field of neutrino physics has been particularly intense: the demonstration in 2001 of neutrino flavor oscillations showed how these particles are massive and mixed. The next challenging step is the identification of the new physics responsible of these neutrino properties. Theoretical simplicity suggests oscillations of three massive neutrinos. Nevertheless this scenario cannot explain some recent experimental results and seems to require additional particles, the so called "sterile" neutrinos. The very recent measurement of the neutrino velocity has contributed to make this topic more challenging: a fundamental rethink of the current understanding of the whole particle physics would be required if this result would be confirmed.

Moreover, the progress in Cosmology and Astrophysics has highlighted the critical dependance of the understanding of the Universe on the knowledge of neutrinos: these elusive particles are the most abundant form of matter in the Universe next to radiation, and they contributed to the origin of heavy elements playing a crucial role in nucleosynthesis.

Despite these last developments there is still a lot to understand about

[1] "Dear Radioactive Ladies and Gentlemen". This letter was written on December 4, 1930 and was addressed to a group of nuclear physicists who were going to meet a few days later in Tübingen, Germany.

neutrinos: the values of their masses, for example, are still unknown. Another open issue concerns their nature: being neutrinos truly neutral particles, they could in principle be Majorana particles, namely they could be their own antiparticles. The only realistic way to determine whether neutrinos are Dirac or Majorana particles is to search for neutrinoless double beta decay: the observation of this rare event would establish for these particles a nonvanishing mass of Majorana nature, and would contribute moreover to the determination of the absolute neutrino mass scale. At present there is no experimental evidence for this process: several half life lower limits are available, ranging from 10^{21}y to 10^{25}y, depending on the isotope choice. The experimental search for such a rare process requires a huge amount of source isotopes operated in a very low background detector: these are the specifications of the "next-generation" experiments, which aim to improve the half life sensitivity by about two orders of magnitude with respect to the best limits currently available.

The purpose of the CUORE experiment is to search for neutrinoless double beta decay in ^{130}Te. Using TeO_2 crystals operated as bolometers at a temperature of about 10 mK in a dedicated cryostat, CUORE aims to reach sensitivities of the order of 10^{26} y on the half life of ^{130}Te which would also imply stringent limits for $m_{\beta\beta}$, the effective neutrino Majorana mass.

A prototype of CUORE, CUORICINO, took data at Gran Sasso National Laboratories in the years 2003-2008. Besides demonstrating the feasibility of a large mass bolometric detector, CUORICINO set the best double beta decay half life limit for the neutrinoless double beta decay of ^{130}Te: $2.8{\cdot}10^{24}$ y at 90%C.L., with a corresponding upper bound on the neutrino Majorana mass $m_{\beta\beta}$ in the range (0.30-0.71) eV.

CUORICINO was also a precious tool for the understanding of the key problematics to be solved for the construction of CUORE. The background level measured by CUORICINO in the ^{130}Te neutrinoless double beta decay energy region was $(0.153{\pm}0.006)$ counts/keV/kg/y: in order to reach the sensitivity of 10^{26}y on the half life of ^{130}Te, CUORE must reduce this value to at least 10^{-2} counts/keV/kg/y. Based on the CUORICINO results, particular efforts have thus been devoted to the reduction of the environmental radioactivity and radioactive contaminants in the CUORE detector which can mimic or simulate the double beta decay signal. For this reason, all materials used in the construction of CUORE have been selected according to their radioactive content and dedicated cleaning procedures have been developed.

An intermediate step will precede the beginning of CUORE: its first tower, named CUORE-0, will be cooled-down in the CUORICINO cryostat

and measured as a stand-alone experiment with the data-taking foreseen in the spring of 2012. CUORE-0 will provide a test for the new CUORE assembly procedure, and a high-statistics check of the improvements implemented to reduce the radioactive background and to improve the bolometric behaviour of the detectors. It will also be a powerful experiment on its own, capable of improving the limit on $m_{\beta\beta}$ set by CUORICINO .

One of the main tasks of this PhD activity was the study of the radiopurity of TeO_2 crystals which will be used in the CUORE experiment. The crystals must satisfy very stringent requirements regarding the bulk and surface contamination levels of ^{238}U and ^{232}Th. Due to their radiopurity, the techniques which are usually employed to check the contamination level are not sensitive enough and only bolometric measurements can be used.

The CUORE crystals quality has been checked conducting measurements on groups of four crystals, which have been randomly selected from the batches received at LNGS, instrumented as bolometers and operated in the Hall C cryostat at LNGS dedicated at the CUORE R&D. Since the data on individual crystal runs is statistically too small for checking the crystal surface contamination levels, an analysis based on the summed statistics of the first 5 runs has been performed, involving 18 crystals in total. Even under very conservative assumptions, the analysis showed that background contribution to CUORE in the neutrinoless double beta decay region of interest due to crystal bulk and surface contaminations will be lower than 0.01 counts/keV/kg/y .

Part of this PhD activity was also dedicated to the study of the cleaning and handling procedure of some fundamental parts of the bolometer detectors, in particular the the readout wires and the Teflon holders, which constitute the thermal conductance between the crystals and the heat sink.

The other main task of this PhD thesis was the characterization of the mechanical suspension for the CUORE detector. The detector has to be mechanically decoupled from the external (building structure and cryogenic apparatus) by a suspension system carefully designed in order to suppress the propagation of vibrations to the crystals which would spoil their energy resolution. The suspension system requires at the same time high tensile properties (it holds the detector mass of $\sim$1.2 ton), low thermal conductivity (the detector has to operate at T$\sim$10mK) and low radioactive contamination, being close to the crystals. This PhD activity was devoted to the characterization of both the suspension materials and of the whole system through dedicated vibration measurements.

This manuscript is divided into six Chapters. In Chapter 1, after a general introduction on neutrino physics, the scientific motivations for the

search of neutrinoless double beta decay will be presented. Chapter 2 will describe the experimental techniques for the search of this process: the most important previous, present and future experiments will be also described. The last part of the Chapter is dedicated to the description of the bolometric technique, the experimental approach adopted by the CUORE experiment. In Chapter 3 the CUORE experiment will be described, with particular attention to the improvements with respect to CUORICINO . Chapter 4 is dedicated to the description of the data analysis of the TeO_2 crystals radiopurity, while Chapter 5 will describe the CUORE assembly line, and features and performances of one important component of the cuore detector, the readout wires. The detector suspension, including the characterization of the materials and the vibration measurements, will be detailed in Chapter 6.

Chapter 1

Neutrino Physics and double beta decay

In recent years, the understanding of the fundamental properties of neutrinos has been significantly altered. The discovery of the non zero neutrino mass represented the first significant change in the standard Model of Particle Physics in many years. After the evidence for neutrino oscillations obtained from the results of atmospheric, solar, reactor and accelerator neutrino experiments, raised the challenge for experimentalists to precisely describe additional neutrino properties and behaviors that are made possible by the non-zero mass. However, the experiments studying neutrino oscillations are not sensitive to the nature of neutrino mass (Dirac or Majorana) and provide no information on the absolute scale of the neutrino masses, since such experiments are sensitive only to the difference of the masses. The current interest in neutrinoless double beta decay is driven by the close relation between this process and fundamental aspects of particle physics, which cannot be investigated by means of oscillation experiments, like for example the Majorana or Dirac nature of neutrinos, the lepton number non-conservation, the absolute neutrino mass scale and the type of neutrino mass hierarchy. In this Chapter, after an overview of oscillation results, and a discussion on the possible mechanism for the generation of neutrino masses, the scientific motivation for the search of neutrinoless double beta decay will be presented.

1.1 The Standard Model and neutrino masses

The Standard Model of particle physics is a quantum field theory describing the electromagnetic, weak and strong nuclear interactions of elementary particles. The theory is characterized by the gauge symmetry $\mathrm{SU}(3)_C \otimes \mathrm{SU}(2)_L \otimes \mathrm{U}(1)_Y$.

The fermions entering the Standard Model can be written as:

$$Q_{fL} = \begin{pmatrix} u_{fL} \\ d_{fL} \end{pmatrix} \, , \, u_{fR} \, , \, d_{fR} \tag{1.1}$$

$$L_{fL} = \begin{pmatrix} \nu_{fL} \\ l_{fL} \end{pmatrix} \, , \, l_{fR} \tag{1.2}$$

where the index f runs over the three quark and lepton families.
The three left-handed neutrino fields included the Standard Model are ν_{eL}, $\nu_{\mu L}$ and $\nu_{\tau L}$: they transform, with the corresponding left-handed charged lepton l_L, as a doublet under the $\mathrm{SU}(2)_L$ gauge symmetry. The right handed charged leptons l_R are singlets under $\mathrm{SU}(2)_L$ and there are no right-handed neutrinos in the Standard Model.

Masses for charged quarks and leptons are generated by the spontaneous breaking of the $\mathrm{SU}(2)_L \otimes \mathrm{U}(1)_Y$ symmetry group, through the Higgs mechanism. Bare mass terms are not allowed in the Lagrangian because they would break the gauge invariance of the theory. The Yukawa interaction between fermions and the Higgs field $\phi = \frac{1}{\sqrt{2}} \begin{pmatrix} \phi^+ \\ \phi^0 \end{pmatrix}$ is a gauge invariant term in the Lagrangian. When the electroweak symmetry is spontaneously broken and the Higgs acquires a vacuum expectation value $\langle 0 \mid \phi \mid 0 \rangle = \frac{1}{\sqrt{2}} \begin{pmatrix} 0 \\ v \end{pmatrix}$, the Yukawa interaction generates a mass term for the charged leptons of the form $\lambda v \overline{l_L} l_R$. This kind of mass term involves both left-handed and right-handed fields and it is called a Dirac mass term. Every massive fermion in the Standard Model acquires its mass from such a Dirac mass term. The absence of right-handed neutrinos implies that neutrinos are massless in the Standard Model: the Yukawa interactions that would give rise to neutrino masses do not exist.

But recent experiments have shown that neutrinos are not massless: in the next section will be discussed observations of neutrino oscillations, which demonstrated that at least two neutrinos have nonzero masses.

The straightforward approach to incorporate neutrino masses into the theory is to add right-handed neutrinos to the particle content of the Standard Model by analogy with the charged leptons or quarks. Then, neutrino

masses would be generated by the usual Higgs mechanism. However, the introduction of right-handed neutrinos allows for new terms in the Lagrangian. Since a right-handed neutrino is uncharged under all the gauge symmetries, a mass term $m\overline{(\nu_{lR})^c}\nu_{lR}$ is gauge invariant. This term should be included in the Lagrangian according to the rule of constructing the most general gauge invariant and renormalizable Lagrangian. This type of mass term, involving fields of the same chirality, is called a Majorana mass term. Majorana mass terms are the only one possible for neutrinos because for charged fermions the Majorana mass terms are not invariant under the $U(1)$ gauge symmetry of electromagnetism. A consequence of the existence of a Majorana mass term is that lepton number is not conserved. Conservation of lepton number is not associated with a gauge symmetry, like the conservation of electric charge is for example. Lepton number is an accidental symmetry of the Standard Model; its conservation is a result of the field content and the requirement of renormalizability [1]. The conservation of lepton number is not viewed as inviolable like the conservation of electric charge, and it is broken in many models extending the Standard Model. Lepton number is the only quantum number that distinguishes neutrinos and antineutrinos. If lepton number is not conserved, there is nothing left to distinguish neutrinos and antineutrinos: neutrinos, being identical to antineutrinos, would thus be Majorana fermions, i.e. fermions that are their own antiparticles.

1.2 Neutrino Oscillations

Neutrino oscillations can take place since the neutrinos of definite flavor ν_f ($f = e, \mu, \tau$) produced in weak interaction processes are not necessarily states of a definite mass ν_k ($k = 1, 2, 3$). Flavor eigenstates ν_f are related to mass eigenstates ν_k by the Pontecorvo-Maki- Nakagawa-Sakata (PMNS) neutrino mixing matrix U_{kf}:

$$|\nu_f\rangle = \sum_{k=1}^{3} U^{\star}_{fk}|\nu_k\rangle \tag{1.3}$$

The PMNS mixing matrix is written in the standard parameterization as:

$$U = \begin{pmatrix} c_{12}c_{13} & s_{12}c_{13} & s_{13} \\ -s_{12}c_{23} - c_{12}s_{23}s_{13}e^{i\delta} & c_{12}c_{23} - s_{12}s_{23}s_{13}e^{i\delta} & s_{23}c_{13}e^{i\delta} \\ s_{12}s_{23} - c_{12}c_{23}s_{13}e^{i\delta} & -c_{12}s_{23} - s_{12}c_{23}s_{13}e^{i\delta} & c_{23}c_{13}e^{i\delta} \end{pmatrix} \cdot$$

$$\cdot \begin{pmatrix} e^{i\phi_1/2} & 0 & 0 \\ 0 & e^{i\phi_2/2} & 0 \\ 0 & 0 & 1 \end{pmatrix} \tag{1.4}$$

where $c_{ij} = \cos\theta_{ij}$, $s_{ij} = \sin\theta_{ij}$ and and δ, $\phi_{1,2}$ are respectively the Dirac and Majorana CP phases.

A non-diagonal mixing matrix U leads to the phenomenon known as neutrino oscillation: when a neutrino is produced in a flavor eigenstate of the weak interaction (i.e. a superposition of mass eigenstates), the probability of later detecting that neutrino in the same flavor eigenstate oscillates with the distance traveled (L) over the energy of the neutrino (E). For the simplified case of only two neutrino states (approximately valid in most experimental situations), and assuming CP conservation, this probability is given by:

$$P(\nu_e \to \nu_e) = 1 - \sin^2 2\theta \sin^2\left(1.27\frac{\Delta m^2_{12}}{\mathrm{eV}^2}\frac{L}{\mathrm{km}}\frac{\mathrm{GeV}}{E}\right) \tag{1.5}$$

where θ is the mixing angle and $\Delta m^2_{12} = m^2_1 - m^2_2$ is the mass-squared difference between the two neutrino states. The two neutrino mixing is a valid approximation for practical description of oscillation experiments. This is a consequence of the experimental evidence for a small value of θ_{13} and for a hierarchical ordering of the mass splittings:

$$\left|\Delta m^2_{12}\right| << \left|\Delta m^2_{13}\right| \sim \left|\Delta m^2_{23}\right| \tag{1.6}$$

The oscillation parameters are therefore described in terms of the solar mixing angle, solar mass-squared difference, atmospheric mixing angle, and atmospheric mass-squared difference. These are identified with the parameters of the full three-neutrino oscillation picture described by the mixing matrix 1.4 as $\theta_{solar} = \theta_{12}$, $\Delta m^2_{solar} = \Delta m^2_{12}$, $\theta_{atm} = \theta_{23}$, $\Delta m^2_{atm} = \Delta m^2_{23}$.

The first experimental hints of neutrino oscillations came from experiments detecting neutrinos from the sun, starting with Ray Davis's chlorine experiment at the Homestake mine[2]. The Davis experiment, which ran between 1970 and 1994, utilized the reaction $\nu_e + {}^{37}\mathrm{Cl} \to \mathrm{e}^- + {}^{37}\mathrm{Ar}$ to measure the flux of neutrinos produced in the sun. It was designed to test

models of the chain of nuclear reactions that power the sun. Rather than confirming the solar models by finding the expected flux of neutrinos, the Davis experiment measured a flux of neutrinos that was only about one-third of what was predicted. This deficit of solar neutrinos was confirmed by the GALLEX [3] and SAGE [4] experiments, which utilized the reaction $\nu_e + {}^{71}\mathrm{Ga} \rightarrow \mathrm{e}^- + {}^{71}\mathrm{Ge}$, although the measured flux in these gallium experiments was about one-half, rather than one-third, of the expected flux. It is know now that the difference in electron neutrino fluxes between the chlorine and gallium experiments is due to the lower energy threshold of the gallium experiments and the energy dependence of neutrino oscillations. The solar neutrino deficit was also observed by the Super-Kamiokande experiment via neutrino-electron scattering in a water Cherenkov detector [5].

The deficit of ν_e from the sun hinted that the ν_e were oscillating into other flavors, but the conclusive evidence that neutrino oscillations were the correct solution to the solar neutrino deficit came from the Sudbury Neutrino Observatory (SNO) experiment [6, 7]. The SNO experiment was the first experiment that could detect the appearance of ν_μ and ν_τ, not just the disappearance of ν_e. The SNO detector was a water Cherenkov detector that used heavy water, D_2O, instead of ordinary water. In addition to elastic scattering and charged-current interactions of neutrinos, thanks to the use of heavy water, SNO was also sensitive to neutral current interactions, $\nu_l + d \rightarrow \nu_l + p + n$, which can happen for any neutrino flavor with equal cross sections. The neutral-current interactions allowed SNO to measure the total flux of solar neutrinos of all flavors, and the total flux agrees with the value predicted by solar models for ν_e production (Fig. 1.1). Together with the reduced flux of ν_e measured in charged-current interactions, the SNO neutral-current rate demonstrates that electron neutrinos produced in the sun oscillate into different flavors on their way to the earth.

The values of the solar mixing angle and mass-squared difference have been measured by combining SNO data with data from the KamLAND reactor antineutrino experiment. The KamLAND experiment measured the flux of electron antineutrinos from nuclear reactors [8]. The KamLAND liquid scintillator detector in the Kamioka mine in central Japan is located at an average distance of ≈180 km from many commercial power reactors. Electron antineutrinos produced in the beta decay of fission products in the reactors are detected when they induce inverse beta decay, $\nu_e + \mathrm{p} \rightarrow \mathrm{e}^+ + \mathrm{n}$, in the KamLAND detector. The delayed coincidence between the prompt signal from the positron and the delayed signal from the capture of the neutron is used to separate antineutrino events from backgrounds. Oscillations measured by KamLAND are characterized by the same mixing angle, θ_{12},

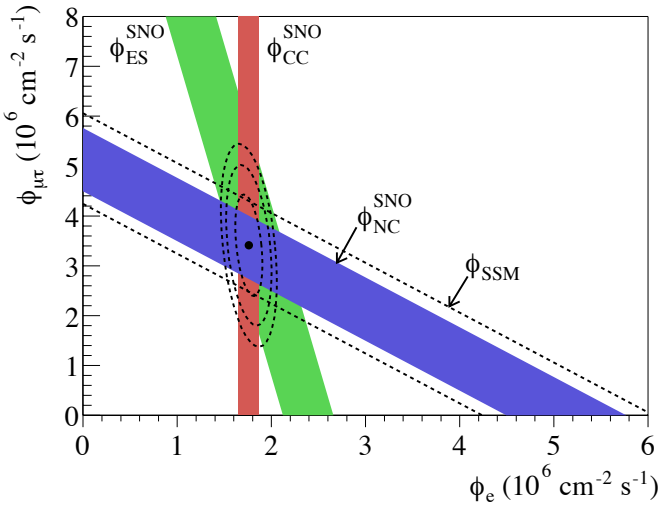

Figure 1.1: Neutrino fluxes measured by SNO in the elastic scattering (ES), charged current (CC), and neutral current (NC) channels. The horizontal axis represents the flux of electron neutrinos, and the vertical axis represents the flux of muon and tau neutrinos combined.

and mass-squared difference, Δm^2_{12}, as the solar neutrino experiments. The measured values of these parameters, obtained from a global analysis of all the experiments, are listed in Table 1.1. KamLAND has also produced the most direct evidence for neutrino oscillations by measuring the electron antineutrino survival probability as a function of L/E, shown in Fig. 1.2.

Neutrino oscillations have also been observed in atmospheric neutrinos, first by the Super-Kamiokande experiment. Atmospheric neutrinos are produced when cosmic rays interact with the air in the upper atmosphere. The collisions mainly produce pions, which produce neutrinos when they decay. The Super-Kamiokande detector is a water Cherenkov detector in the Kamioka mine that detects atmospheric neutrinos via charged-current interactions with nucleons, ν_l + N $\rightarrow$ l + N'. Because the earth is spherical, the flux of upward-going and downward-going neutrinos at the detector site would be symmetric if no oscillations occurred. Super-Kamiokande found a clear asymmetry in upward-going and downward-going neutrinos [10]. The oscillation effect was confirmed by the accelerator-based, long baseline experiments K2K [11] and MINOS [12], and the measured values for the oscillation parameters, θ_{23} and Δm^2_{23} are listed in Table 1.1.

The value of the third mixing angle θ_{13} was initially bounded close to

Parameter	Best Value	2σ C.L.
Δm^2_{12}	7.58×10^{-5} eV^2	(7.16-7.99) $\times 10^{-5}$ eV^2
Δm^2_{13}	2.35×10^{-3} eV^2	(2.17-2.57) $\times 10^{-3}$ eV^2
$\sin^2\theta_{12}$	0.306	0.275-0.342
$\sin^2\theta_{23}$	0.42	0.36-0.60
$\sin^2\theta_{13}$	0.021	0.008-0.036

Table 1.1: Measured values of neutrino mixing parameter [9].

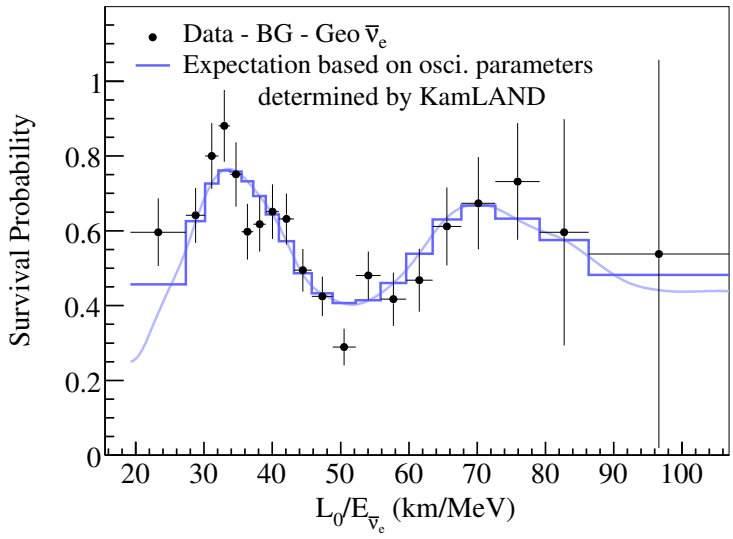

Figure 1.2: Electron anti-neutrino survival probability as a function of L/E measured by the KamLAND experiment. L_0 is the effective baseline taken as a flux-weighted average ($L_0 = 180\,\mathrm{Km}$). Figure taken from [8].

zero from the short-baseline reactor experiments, like Chooz [13] and Palo Verde [14] about ten years ago. Very recently, new relevant results have been announced by two long-baseline accelerator experiments probing the $\nu_\mu \to \nu_e$ appearance channel, which is governed by the θ_{13} and Δm^2_{23} parameters. In particular, the Tokai-to-Kamioka (T2K) experiment has observed 6 electron-like events with an estimated background of 1.5 events, rejecting $\theta_{13} = 0$ at the level of 2.5σ [15]. The low background level makes the T2K results particularly important and robust. Shortly after, the Main Injector Neutrino Oscillation Search (MINOS) experiment has reported the observation of 62 electron-like events with an estimated background of 49 events, disfavoring $\theta_{13} = 0$ at 1.5σ [16]. These data, suggesting a non-zero value of θ_{13} (see Table 1.1), would open a wide range of possibilities to explore CP-violation and the mass hierarchy.

1.3 Dirac and Majorana neutrinos

A free spin -1/2 fermion, whether Dirac or Majorana, may be represented by a four-component spinor field ψ, which satisfies the Dirac equation

$$(i\gamma^u \partial_u - m)\,\psi = 0 \tag{1.7}$$

The field may be decomposed into left-handed and right-handed chiral projections $\psi = \psi_L + \psi_R$ where

$$\psi_L = \left(\frac{1-\gamma_5}{2}\right)\psi, \quad \psi_R = \left(\frac{1+\gamma_5}{2}\right)\psi \tag{1.8}$$

The field of a Majorana fermion, by definition, satisfies the constraint

$$\psi = \psi^c, \tag{1.9}$$

where $\psi^c = \mathcal{C}\psi = \gamma_0\gamma_2\bar{\psi}^T$ and $\mathcal{C}$ is the charge-conjugation matrix. Under the action of $\mathcal{C}$ a left-handed field goes into a right-handed one, and viceversa. As a consequence of the fact that neutrino has no electric charge, it is possible that the right handed component of the neutrino field is simply the $\mathcal{C}$-conjugated of the left handed field. If this possibility is verified then neutrino is said to be a Majorana particle. The Majorana condition implies $\psi_R = (\psi_L)^c$, so the left-handed and right-handed components of a Majorana field are not independent. It is then clear that the possibility of describing a fermion by a Majorana field only arises for neutrinos, as the other fermions

have electric charge. The Lagrangian mass term for a Majorana neutrino can be written as

$$-\mathcal{L} = -\frac{1}{2} m \left(\bar{\nu}_L^c \nu_L + \bar{\nu}_L \nu_L^c\right) \tag{1.10}$$

In principle neutrinos can have both Majorana and Dirac mass terms. Considering for simplicity the case of only one flavor, it reads

$$-\mathcal{L} = \frac{1}{2} \left(\bar{\nu}_L^c \; \bar{\nu}_R\right) \begin{pmatrix} 0 & m_D \\ m_D & M_R \end{pmatrix} \begin{pmatrix} \nu_L \\ \nu_R^c \end{pmatrix} + \text{h.c.}; \tag{1.11}$$

In eq. 1.11 the two independent fields ν_L and ν_R are present, m_D is the Dirac mass and M_R is the Majorana mass for ν_R. Note that the coefficient m_L has been set to zero: since in the Standard Model ν_L has weak Isospin projection $I3 = 1/2$, the corresponding Majorana mass term would be a Isospin triplet and would not be gauge invariant. The mass matrix introduced in 1.11 can be diagonalized to find the corresponding mass eigenstates. After the mass matrix is diagonalized, the neutrino Lagrangian mass term takes the form

$$-\mathcal{L} = \frac{1}{2} \sum_{k=1,2} m_k \, \bar{\nu}_{kL}^c \nu_{kL} + \text{h.c.} \tag{1.12}$$

where

$$\begin{aligned} \nu_1 &= \cos\theta \, \nu_L + \sin\theta \, \nu_R^c \\ \nu_2 &= -\sin\theta \, \nu_L + \cos\theta \, \nu_R^c \end{aligned} \tag{1.13}$$

and $\tan 2\theta = m_D / M_R$.

Few considerations arise from the previous equations. First, as can be seen from eq. 1.12, even in the general case in which also the Dirac mass term is present, in the mass eigenstates basis neutrinos are described by Majorana fields. In addition, while the Dirac mass m_D, being generated by the Higgs mechanism, is expected to be more or less of the same order of magnitude of the mass of other fermions, there are no limitations for the Majorana mass M_R. In particular it can assume arbitrarily large values. If $M_R >> m_D$ it turns out from eq. 1.13 that

$$\begin{aligned} \nu_1 &\simeq \nu_L, \quad m_1 \simeq \frac{m_D^2}{M_R} \\ \nu_2 &\simeq \nu_R^c, \quad m_2 \simeq M_R \end{aligned} \tag{1.14}$$

If this condition is verified, the heavy neutrino ν_2 is predominantly ν_R^c and the light neutrino ν_2 is essentially the observed particle ν_L. Thus the introduction of the Majorana mass term in the Lagrangian leads to a natural

explanation for the smallness of neutrino masses: the bigger is the mass of the unseen particle ν_R, the smaller is the mass of ν_L.
The nature of neutrinos, Dirac or Majorana, and whether lepton number is conserved in nature are open experimental questions. Experiments aiming to answer these questions attempt to observe a lepton-number-violating process, with neutrinoless double beta decay being the most promising candidate.

1.4 Double beta decay

Double beta decay (DBD) is a second order weak process, in which a nucleus changes its atomic number by two units:

$$(A, Z) \rightarrow (A, Z + 2) \tag{1.15}$$

It occurs for some even-even nuclei for which the single beta decay is energetically forbidden, or suppressed by large change in angular momentum. Two different DBD modes are usually considered: first, the decay with two neutrinos (2νDBD), which is allowed in the Standard Model, that is described by the reaction

$$(A, Z) \rightarrow (A, Z + 2) + 2e^- + 2\bar{\nu_e} \tag{1.16}$$

and, second, the neutrinoless decay (0νDBD) given by

$$(A, Z) \rightarrow (A, Z + 2) + 2e^-. \tag{1.17}$$

The double beta decay accompanied by two neutrinos (see fig. 1.3(a)) was detected for the first time in ^{82}Se in 1987 [17]. It is a standard second order weak decay, which does not depend on the Dirac or Majorana nature of the neutrino, and may be modeled as two successive single beta transitions which proceed via virtual intermediate nuclear states. Double beta decay half-lives for nuclei that undergo the process are very long, on the order of 10^{18}-10^{24} years since the decay is second order in the weak interaction. The measured half-lives of double beta decaying isotopes are listed in Table 1.2.

The double beta decay without emission of neutrinos, 0νDBD , is instead forbidden in the Standard Model, since it violates the lepton number by two units and has never been observed (except for one controversial claim discussed in Sect. 2.1.1). 0νDBD decay can proceed through many different mechanisms: almost any physics that violates the total lepton number can generate it [39]. The simplest way to obtain neutrinoless double beta decay is by the exchange of a massive Majorana neutrino: it is possible to consider

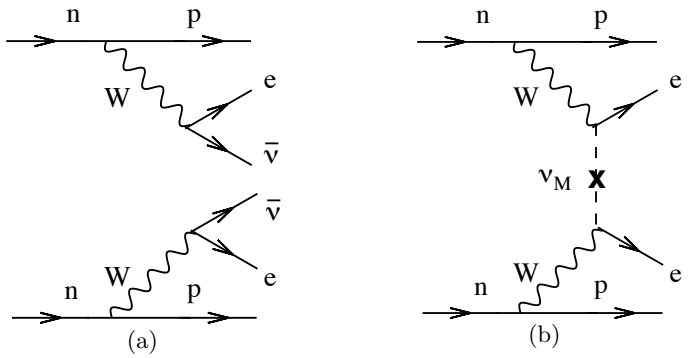

Figure 1.3: Double beta decay diagrams for the 2νDBD mode (left) and the 0νDBDmode (right). The 0νDBD diagram assumes that the process is mediated by the exchange of a Majorana neutrino (see the text).

the virtual neutrino in the diagram of Fig. 1.3(b) as being produced as an antineutrino (equal to a neutrino since it is Majorana) at one vertex and absorbed as a neutrino at the other vertex. In addition to the Majorana equivalence of neutrino and antineutrino, a nonzero neutrino mass is required to flip the helicity since antineutrinos are right-handed and neutrinos are left-handed. The helicity flip and the smallness of the neutrino mass cause the rate of 0νDBD decay, if it occurs at all, to be much lower than the rate of 2νDBD decay.
The rate of 0νDBD decay driven by the exchange of light Majorana neutrinos can be written as:

$$\left[T^{0\nu}_{1/2}\right]^{-1} = G_{0\nu}\,|M_{0\nu}|^2\,\langle m_{\beta\beta}\rangle^2 \tag{1.18}$$

where $G_{0\nu}$ is the phase space factor, $M_{0\nu}$ is the nuclear matrix element (NME), and $m_{\beta\beta}$ is the effective Majorana mass defined as:

$$m_{\beta\beta} \;=\; \left|\sum_{j=1}^{3} U_{ej}^2\, m_j\right| \;=\; \left|\sum_{j=1}^{3} |U_{ej}|^2\, e^{i\phi_j}\, m_j\right| \;. \tag{1.19}$$

The particle physics information is contained in $m_{\beta\beta}$. The phase space factor $G_{0\nu}$ is easily calculable. Calculation of the NME $M_{0\nu}$ is instead not a trivial issue in nuclear theory. It will be discussed further in 1.4.2. Experiments try to measure $T^{0\nu}_{1/2}$, and in the absence of a signal, they set a lower limit. Apart for a controversial claim (see Sect. 2.1.1), 0νDBD has

DBD Decay Reaction	$T^{2\nu}_{1/2}$[y]	Reference
^{48}Ca $\rightarrow$ ^{48}Ti	$(4.4^{+0.6}_{-0.5})\cdot 10^{19}$	[18, 19, 20]
^{76}Ge $\rightarrow$ ^{76}Se	$(1.5 \pm 0.1)\cdot 10^{21}$	[21, 22, 23]
^{82}Se $\rightarrow$ ^{82}Kr	$(9.2 \pm 0.7)\cdot 10^{19}$	[24, 25, 26]
^{96}Zr $\rightarrow$ ^{96}Mo	$(2.3 \pm 0.2)\cdot 10^{19}$	[20, 27]
^{100}Mo $\rightarrow$ ^{100}Ru	$(7.1 \pm 0.4)\cdot 10^{18}$	[24, 28, 29]
^{116}Cd $\rightarrow$ ^{116}Sn	$(2.8 \pm 0.2)\cdot 10^{19}$	[20, 30, 31, 32]
^{130}Te $\rightarrow$ ^{130}Xe	$(6.8^{+1.2}_{-1.1})\cdot 10^{20}$	[33, 34]
^{136}Xe $\rightarrow$ ^{136}Ba	$(2.29 \pm 0.12)\cdot 10^{21}$	[35, 36]
^{150}Nd $\rightarrow$ ^{150}Sm	$(8.2 \pm 0.9)\cdot 10^{18}$	[29, 37, 38]

Table 1.2: 2νDBD half-lives observed for various double beta decaying isotopes.

never been observed. The experimental lower limits for the half-lives are reported for a set of commonly studied isotopes in Table 1.3.

Parent Isotope	$T^{0\nu}_{1/2}(y)$	Reference
^{48}Ca	$> 1.4 \times 10^{22}$	[40]
^{76}Ge	$> 1.9 \times 10^{25}$	[41]
^{76}Ge	1.19×10^{25}	[42]
^{82}Se	$> 1 \times 10^{23}$	[43]
^{96}Zr	$> 1.0 \times 10^{21}$	[44]
^{100}Mo	$> 4.6 \times 10^{23}$	[43]
^{116}Cd	$> 1.7 \times 10^{23}$	[45]
^{130}Te	$> 2.8 \times 10^{24}$	[46]
^{136}Xe	$> 1.2 \times 10^{24}$	[47]
^{150}Nd	$> 1.8 \times 10^{22}$	[48]

Table 1.3: Commonly studied double beta decay isotopes and best lower limits for the 0νDBD half lives. The claim of observation in ^{76}Ge will be discussed later in Sect. 2.1.1.

1.4.1 0νDBD and neutrino masses

If neutrinos are Majorana particles, measuring or constraining the effective Majorana mass provides information on the neutrino mass scale and hierarchy. This is possible because there is a relationship between the effective

Majorana mass and the mass of the lightest neutrino. This relationship depends on whether the hierarchy is normal or inverted because the lightest neutrino mass eigenstate depends itself on the hierarchy (see Fig. 1.4).

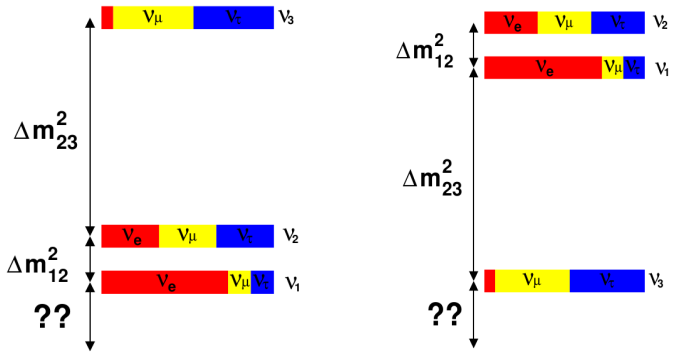

Figure 1.4: Neutrino mass eigenstates for (a) normal and (b) inverted hierarchy.

Taking a closer look to the definition of the effective neutrino mass (eq. 1.19), in the case of normal hierarchy mass with m_1 as the lightest mass eigenvalue, it takes the form:

$$\begin{aligned} m_{\beta\beta} &\equiv \left|U_{e1}^2\, m_1 + U_{e2}^2\, m_2 + U_{e3}^2\, m_3\right| \\ &= \left|U_{e1}^2 m_1 + U_{e2}^2\sqrt{\Delta m_{12}^2 + m_1^2} + U_{e3}^2\sqrt{\Delta m_{13}^2 + m_1^2}\right| \\ &= \left|\cos^2\theta_{12}\cos^2\theta_{13}\; e^{i\alpha_1}\; m_1 + \sin^2\theta_{12}\cos^2\theta_{13}\; e^{i\alpha_2}\cdot\right. \\ &\quad \left.\cdot\sqrt{\Delta m_{12}^2 + m_1^2} + \sin^2\theta_{13}\; e^{-2i\delta}\sqrt{\Delta m_{13}^2 + m_1^2}\right|, \end{aligned} \tag{1.20}$$

where α_1 and α_2 are Majorana phases and δ is the Dirac phase. A similar equation is easily obtained for the inverted mass hierarchy in which m_3 is the lightest mass eigenvalue. Plugging in the measured values of the neutrino mixing angles and mass-squared differences (see Table 1.1) a value for $m_{\beta\beta}$ is obtained for each value of the lightest neutrino mass, m_1 for the normal hierarchy or m_3 for the inverted hierarchy, and for a given set of values for the phases (α_1, α_2 and δ).

Fig. 1.5 shows the range of allowed values for the effective mass hierarchy for each value of the lightest neutrino mass. The green band indicates the allowed parameter space in the case of inverted mass hierarchy, while the red

band corresponds to the case of normal mass hierarchy. The two bands overlap in the zone of degenerate mass hierarchy (where the mass of the lightest neutrino is $\sim 10^{-2}eV$). Double beta decay experiments with better sensitivity are able to probe smaller values of $m_{\beta\beta}$. Thus, observation of double beta decay would not only imply that neutrinos are Majorana particles: it would also provide information on the neutrino mass hierarchy and on the absolute scale of neutrino mass. If instead this process is not observed, it cannot be concluded that neutrinos are Dirac particles: the presence of the vertical dip in the normal hierarchy band (which correspond to a particular combination of the two Majorana phases) indicates the fact that $m_{\beta\beta}$ could vanish, even if neutrinos are Majorana particles.

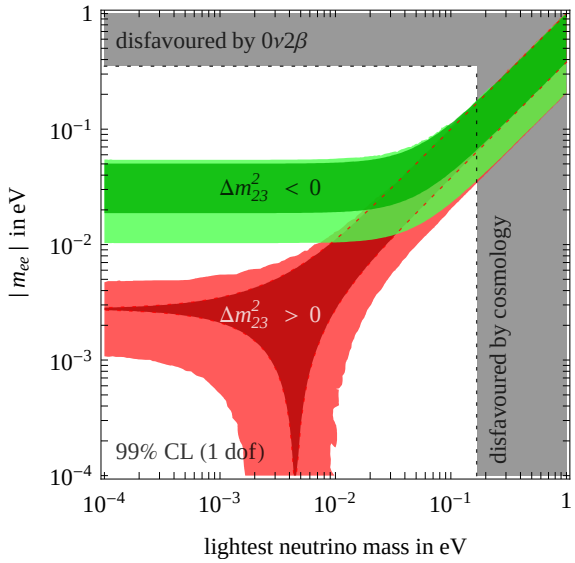

Figure 1.5: 99% C.L. expected ranges of effective Majorana mass as function of the lightest neutrino mass. The red region corresponds to normal hierarchy and the green one to the inverted hierarchy. The darker regions show how the ranges would shrink if the present best-fit values of oscillation parameters were confirmed with negligible error. The grey bands indicate the parameter space that is excluded by current double beta decay experiments and by cosmological observations. Figure from [49].

1.4.2 Nuclear Matrix Elements

It has just been discussed that without making any assumption on the mechanism that generates 0νDBD the existence of this process implies that neutrinos are Majorana particles. However, in order to extract informations on the neutrino mass hierarchy and the absolute mass scale, some assumptions must be made on the mechanism that is responsible for this process. The simplest possibility is to assume that the 0νDBD decay occurs by the exchange of a light Majorana neutrino. It is clear from Eq. 1.18 that, even under this assumption, the phase space factor $G_{0\nu}$ and the Nuclear Matrix Element $M_{0\nu}$ (NME) must be known in order to extract the value of $m_{\beta\beta}$. Moreover, even if the observation of 0νDBD decay of an isotope is enough to make the discovery, the confirmation and the comparison with different isotopes is needed to rule out the possibility that the observed signal is produced by some other unknown rare process able to mimic the 0νDBD experimental signature. Since different isotopes have different phase space factors and NME, these quantities must be known to combine and compare the results of different experiments.
While $G_{0\nu}$ is precisely calculable, NME represents the biggest source of theoretical uncertainty and cannot be determined experimentally, as it occurs only in the 0νDBD. Nuclear matrix elements depend on the structure of the parent and daughter nuclei, as well as the intermediate one. Since a many bodies problem must be solved, the calculation cannot be carried out analytically, but requires numerical computations in which several approximations are introduced.

Approaches for evaluating NME have generally fallen into two categories, the Interacting nuclear Shell Model (ISM) [50] and the Quasiparticle Random Phase Approximation (QRPA)[51]. Recently new approaches like the Interacting Boson Model (IBM) [52] and the Generating Coordinate Model (GCM) [53] have also been applied. In the ISM, interactions are described by an effective Hamiltonian which is diagonalized over all configurations of a chosen subset of valence single-particle states. In principle ISM calculations are more reliable, as they require few approximations. However such calculations are computationally intensive, which places a practical limit on the number of single-particle valence states that can be considered. QRPA calculations use a larger valence space with respect to ISM, but the interaction strengths are parameterized, and only a subset of the possible configurations are taken into account. In the GCM approach is also taken into account the tendency of nucleon to align its orbit with the average field produced by all other nuclei. The IBM represents an intermediate path between the "mi-

croscopic" view of nuclear structure of ISM and the "collective" view of the above mentioned QRPA and GCM. The IBM model is based on the shell model, the complexity of which is reduced heavily by combining the nucleons in pairs, which represent bosons.

There has been significant progress in the calculations of NME in recent years. Now the calculations obtained with different approaches lie within a factor of two to each other, as can be seen in Fig. 1.6.

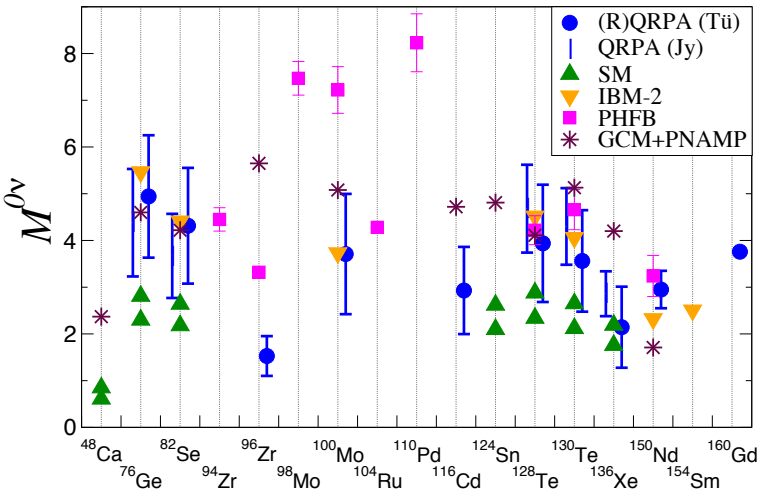

Figure 1.6: Nuclear matrix element calculations for several 0νDBD isotopes different approaches. The two QRPA calculations shown in the figure agree well with each other and with an interacting boson model (IBM) calculation, while the recent NSM calculation is roughly a factor of two lower. Nevertheless, for a given isotope, the calculations spread by typically a factor 2. Picture from[54].

Chapter 2

Experimental searches for double beta decay

The observation of 0νDBD is a challenging task from the experimental point of view. Being a very rare process, the experimental search of this decay requires a large amount of mass operating in low background conditions and an excellent energy resolutions. This Chapter, after an overview of the fundamental requirements which have to be satisfied by a double beta decay experiment, presents the most important results which have been obtained so far. The chapter describes as well the current and future experiments and presents, at the end, the bolometric technique, the approach used in the CUORE experiment.

2.1 Fundamentals of 0νDBD experiments

The amount of energy released in double beta decay, usually defined Q-value, is given by the mass difference between the parent and the daughter nucleus, subtracted by the masses of the two emitted electrons:

$$Q_{\beta\beta} = M_p - (M_d + 2\,m_e)\ . \tag{2.1}$$

In the 2νDBD the two neutrinos carry away part of the energy, giving rise to a continuous spectrum of the sum energy of the two electrons. In the 0νDBD decay all the energy goes into the electrons, so that the signature is a monochromatic line in the energy spectrum at the kinetic energy of the two electrons (see Fig. 2.1). Therefore, at least in principle, the signature of 0νDBD is very clear. Despite such characteristic signature, the rate of double beta decay is so low that its identification is very difficult. The two

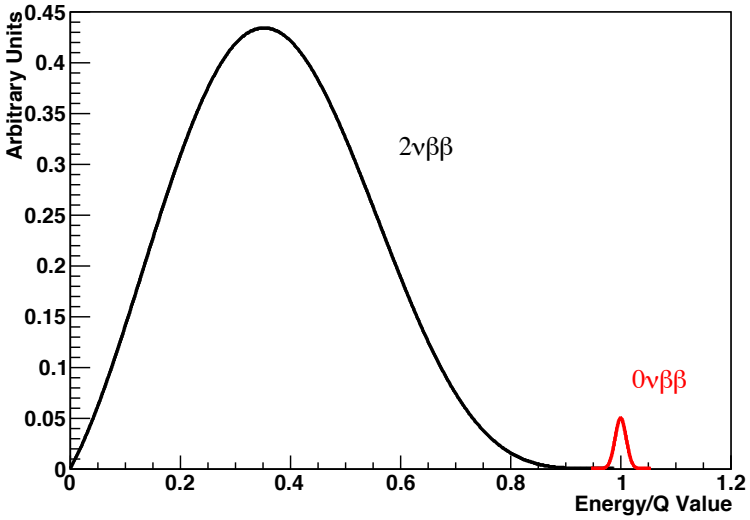

Figure 2.1: Summed electron energy spectrum for double beta decay.

main requirements for an experiment designed to observe this peak are a very low background level and the capability to measure electron energies with high resolution. A low background level is required to make statistically significant the discovery of a 0νDBD decay signal and a high energy resolution prevents the tail of the 2νDBD decay continuum spectrum from hiding a small 0νDBD decay peak. The fraction F of 2νDBD events that are contained in the ΔE energy window centered at the Q-value of the decay is given by [55]:

$$F \approx \frac{\Delta E^6}{Q_{\beta\beta}^5}. \tag{2.2}$$

To compare different experiments and to point out the advantages and the disadvantages of different detecting techniques, it is convenient to introduce a very important parameter, called *sensitivity*, denoted by S. It is defined as the half-life corresponding to the minimum number of signal events observable above background at a given statistical significance. For experiments in which the background events scale with the total mass of the detector it can be expressed as [39]

$$S^{0\nu}\left(n_\sigma\right) \;=\; \frac{\ln 2}{n_\sigma}\,\epsilon\,N_a\,\frac{\eta}{A}\,\sqrt{\frac{M\cdot t}{b\cdot\Delta E}}\;, \tag{2.3}$$

where n_σ is the statistical significance, ϵ is the detection efficiency, N_a is the Avogadro number, η is the isotopic abundance of the studied nucleus, A is the atomic mass number, M is the total detector mass, t is the live time of the experiment, ΔE is the resolution and b is the background, expressed in counts/keV/kg/y. To compare the discovery potential of experiments using different isotopes, it is also convenient to define the nuclear factor of merit F_N:

$$F_N = m_e^2 \, G_{0\nu} \, |M_{0\nu}|^2 \tag{2.4}$$

where m_e is the electron mass and F_N has dimension of years^{-1}. Using equation 1.18 and replacing the half-life with the sensitivity, the Majorana mass measurable by an experiment can be expressed as:

$$m_{\beta\beta} = \frac{m_e}{\sqrt{S^{0\nu} \cdot F_N}} \tag{2.5}$$

where the sensitivity accounts for the experimental features and the nuclear factor of merit accounts for the 0νDBD isotope. In Tab. 2.1 are reported the nuclear factor of merit, the Q-value and the natural abundance of the most used 0νDBD candidates.

It is clear from eq. 2.3 that high isotopic abundances are preferable, as they correspond to an increase in the number of observed 0νDBD nuclei. Even if rather expensive, isotopic enrichment is often the only choice for those candidate nuclei which have low natural abundances. Isotopes with high Q-values are preferred for several reasons. First, the background from natural radioactivity decreases with increasing Q. A marking point is represented by the 2615 keV line from ^{208}Tl, the γ-line from natural radioactivity

Parent Isotope	F_N [y^{-1}]	$Q_{\beta\beta}$ [keV]	η [%]
^{48}Ca	$0.54 \cdot 10^{-13}$	4271	0.19
^{76}Ge	$0.73 \cdot 10^{-13}$	2039	7.4
^{82}Se	$1.7 \cdot 10^{-13}$	2995	8.7
^{100}Mo	$5.0 \cdot 10^{-13}$	3034	9.6
^{116}Cd	$1.3 \cdot 10^{-13}$	2902	7.5
^{130}Te	$4.2 \cdot 10^{-13}$	2527	34.1
^{136}Xe	$0.28 \cdot 10^{-13}$	2479	8.9
^{150}Nd	$57 \cdot 10^{-13}$	3367	5.6

Table 2.1: Nuclear factor of merit F_N, Q-value and natural abundance (η) for several double beta decay isotopes of experimental interest. The values of F_N are taken from [56].

with the highest energy. Isotopes with Q-values above this energy benefit from a much lower background level. Moreover isotopes with large Q-values are preferred because the phase space factor that appears in the formula for the decay rate scales as $G_{0\nu} \sim Q^5$ and because the fraction F of the 2νDBD counts in the region of the 0νDBD peak scales as $F \sim 1/Q^5$.

2.1.1 Past double beta decay experiments

Past double beta decay experiments had typical sensitivities to the effective Majorana mass in the degenerate neutrino mass hierarchy region of Fig. 1.5.

Two main experimental approaches are considered. In the *source = detector* approach the DBD emitter is part of or constitutes the detector. In this way particles are fully absorbed in the detector, allowing high detection efficiency (of order 90%). Nevertheless there is no sensitivity to the event topology and nature, reducing the background rejection capability. In the *source ≠ detector* approach the DBD emitter is passive and is surrounded by an active detector. Exploiting the typical signature of a two electrons event, the background rejection is very high. On the other hand the detection efficiency is poor (of order 30%).

The most sensitive current limit on 0νDBD (a complete list is in Tab. 1.3) has been obtained so far in ^{76}Ge by the Heidelberg - Moscow [57] and IGEX collaboration [58], using High Purity Germanium semiconductors (HPGe) as detectors. The big advantage of semiconductor detectors is their excellent energy resolution (about 4 keV at 2 MeV). Even if these devices can only measure the sum energy of the two electrons emitted in the decay, some background reduction can be obtained by exploiting pulse shape analysis.

The Heidelberg-Moscow (HM) Collaboration operated five HPGe detectors enriched to a level of 86% in ^{76}Ge with a total source mass of 10.96 kg. Located in the Gran Sasso underground laboratory, the experiment ran from 1990 to 2003 and collected 71.7 kg·y exposure of ^{76}Ge [59]. It achieved a background level of 0.11 counts/keV/kg/y in the energy region around the ^{76}Ge Q-value of 2039 keV.

In 1999 the HM Collaboration produced a limit of $T^{0\nu}_{1/2} > 5.7 \cdot 10^{25} y$ at 90% C.L [60]. Later in 2001 a subset of the collaboration claimed a 3.1σ evidence for 0νDBD decay of ^{76}Ge [61], with an half life of $T^{0\nu}_{1/2} = 1.5 \cdot 10^{25}$y and a corresponding effective neutrino mass of $m_{\beta\beta} = 0.39$ eV. Due to the fact that this result was not published by the full collaboration and due to several technical criticisms of the analysis [62, 63], the claim of discovery

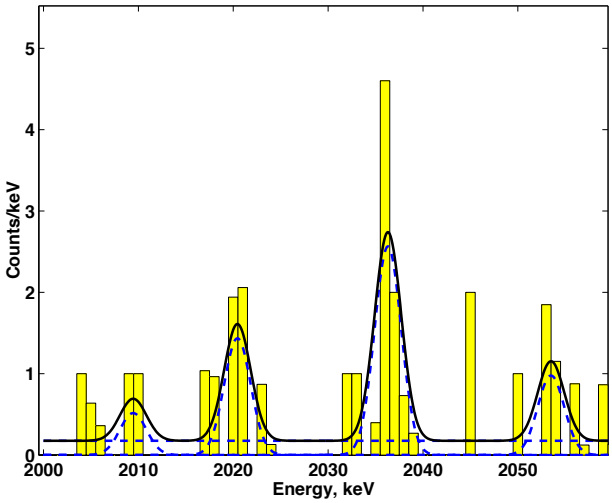

Figure 2.2: The Heidelberg-Moscow spectrum of single site events near the Q-value of ^{76}Ge after application of pulse shape discrimination. Figure from [42].

has not been fully accepted by the scientific community.

However, the authors confirmed their claim with more data, more sophisticated analyses, and produced results with greater statistical significance [42, 64, 65]. In particular, they developed a pulse shape discrimination capability to distinguish between single-site events and multi-site events in their germanium detectors. Indeed double beta decay events deposit the decay energy within a small and localized region and are therefore single-site events, whereas gamma backgrounds typically Compton scatter in the detector at least once before being fully absorbed and are therefore usually multi-site events. Pulse shape discrimination is in principle a powerful tool for separating a double beta decay signal from background in a germanium detector. Application of pulse shape discrimination to the Heidelberg-Moscow data produced an extremely low background spectrum that contains a peak at the Q-value measured with a statistical significance greater than 4σ (Fig. 2.2) [42].

The scientific community still did not find the analysis as conclusive due to concerns about the validation of the pulse shape discrimination method. It is clear that the issue will only be settled by confirmation or confutation of the claim with data from next generation experiments.

The International Germanium Experiment (IGEX) was similar to HM. It

used 86% isotopically enriched HPGe detectors to search for 0νDBD decay of ^{76}Ge. The collaboration originally operated detectors at three different underground laboratories: the Homestake gold mine in the United States, the Canfranc Tunnel in Spain, and the Baksan Neutrino Observatory in Russia. Then, three 2 kg detectors were operated at Canfranc. The final resulting limit on 0νDBD decay was $T^{0\nu}_{1/2} > 1.6 \cdot 10^{25} y$ (90% C.L.)[66].

Competitive limits on neutrinoless double beta decay came also from the Neutrino Ettore Majorana Observatory (NEMO-3 [67]) which ended in January 2011 after 5 years of data collection. The NEMO-3 experiment is notable because it has the capability to track charged particles and perform particle type identification. In the NEMO-3 detector, a *source* $\neq$ *detector* design, the double beta decaying source was contained in thin foils. The set-up, installed underground in the Laboratoire Souterrain de Modane (France), was divided in twenty sectors, allowing the study of many nuclides at the same time, such as ^{100}Mo, ^{82}Se, ^{150}Nd, ^{116}Cd, ^{130}Te, ^{96}Zr and ^{48}Ca. Particles emitted from the foils are tracked inside a wire ionization cham-

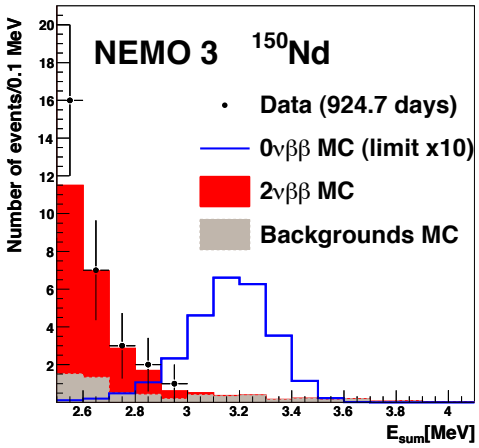

Figure 2.3: Distribution of the energy sum E_{sum} of the two electrons for the 2νDBD of ^{150}Nd from the NEMO-3 experiment. The data are compared to the total background and the the 2νDBD expectation. Figure from [48].

ber and their energies are measured by plastic scintillator calorimeters. This type of detector provides a rich set of information, including the number and type of particles in the decay, independent measurements of the energy of each final state particle, and angular distributions of decay products. This information is a great help for disentangling signal events from backgrounds.

It also allows to search for 0νDBD decay in many isotopes by changing the source foil. Thanks to its background suppression capabilities and module source design, NEMO-3 has made precision measurements of the 2νDBD half-lives of several isotopes [43, 68, 48] (an example of the energy sum spectrum of the two electrons for ^{150}Nd is shown in Fig. 2.3). However, this approach is limited to relatively small source masses and has limited energy resolution.

The CUORICINO detector operated in the underground site of LNGS from 2003 to 2008 searching for neutrinoless double beta decay in ^{130}Te using the bolometric technique. CUORICINO not only obtained the best present limit on the ^{130}Te 0νDBD half life, but also prepared the way for one of the most promising next-genereration 0νDBD searches, the CUORE experiment, that constitutes the framework of this PhD thesis. For this reason, in this section just a brief description of the CUORICINO experiment will be given, being the subjects discussed in details in next Chapters.

The CUORICINO experiment was an array of 62 TeO_2 bolometers arranged in a tower of 13 floors (see Fig. 2.4(a)). Each floor consisted of a single module detector as described in Sec. 3.4. Eleven floors were made out of four crystals 5·5·5 cm^3 each (see Fig. 2.4(b)), while the two remaining floors were composed by nine crystals 3·3·6 cm^3 each (see Fig. 2.4(b)). The operating principle of a bolometer is very simple: the energy deposited in the detector by a nuclear event is measured by recording the temperature increase of the detector. In order to make the extremely small heating signal appreciable and to reduce all the intrinsic noise source, the detector must be operated at very low temperature, of the order of $\sim$10 mK. In the CUORICINO detector the absorber is a TeO_2 crystal and the thermal pulses are read by Neutron Transmutation Doped Germanium Thermistors. The mechanical structure of the detector is made of OFHC copper, to which the bolometers are connected by means of Teflon holders. Several layers of low radioactivity lead and borated polyethylene were also used to shield the detectors and minimize the external background (see Fig. 2.4(d)). To avoid heating due to vibrations the tower was mechanically decoupled from the cryogenic apparatus using a stainless steel spring. The CUORICINO spectrum measured in the double beta decay region is shown in Figure 2.5. With no evidence of ^{130}Te 0νDBD , the limit on the half life was set to $T^{0\nu}_{1/2} > 2.8 \cdot 10^{24}$ y [46], corresponding to a sensitivity on the effective Majorana mass of $m_{\beta\beta} < 0.3 \div 0.7$ eV, depending on the adopted nuclear matrix element.

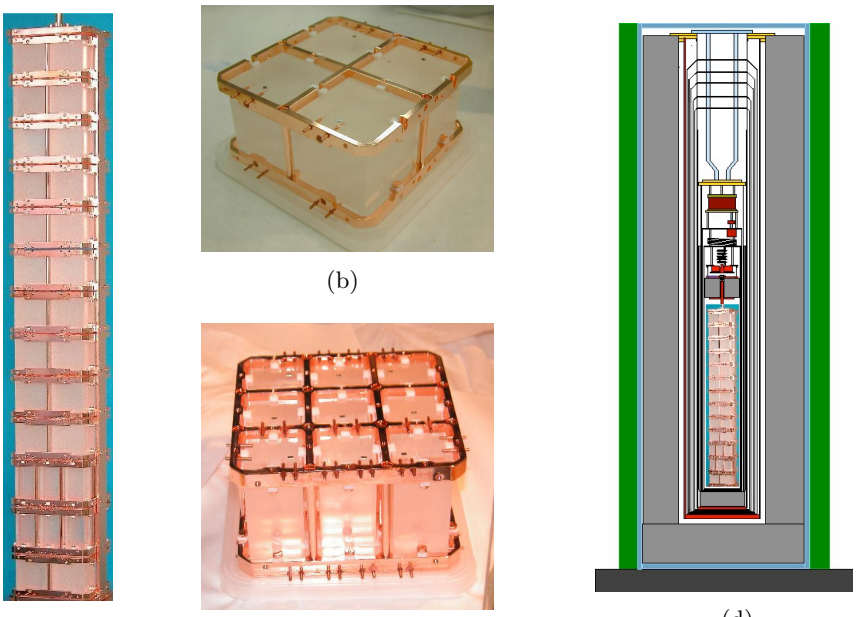

(a) (b) (c) (d)

Figure 2.4: (a): the CUORICINO tower; (b): one of the eleven floors composed by four crystals; (c):i one of the two nine crystals floors; (d): sketch of the shieldings surrounding the detector array.

2.1.2 Present and future double beta decay experiments

In the last year some "next generation" 0νDBD decay experiments have started running. These experiments aim at reaching a sensitivity on the effective Majorana mass of $\sim$50 meV in order to cover the quasi-degenerate neutrino mass regime and perhaps to begin to probe the inverted hierarchy. This corresponds to an increase of about one order of magnitude in the $m_{\beta\beta}$ sensitivity with respect to the past experiments, that in terms of half-life corresponds to an increase of two orders of magnitude.

From Eq. 2.3 it is clear that, fixing the 0νDBD candidate, the source mass (M) and the measuring time (t), the half-life sensitivity can be improved mainly by acting on the energy resolution (ΔE) and the background level (b).

The good energy resolution is the only protection against the intrinsic 2νDBD background, and improves the signal-to-noise ratio in the region of interest around the Q-value. Nevertheless the future double beta decay experiments are mainly devoted to the background suppression.

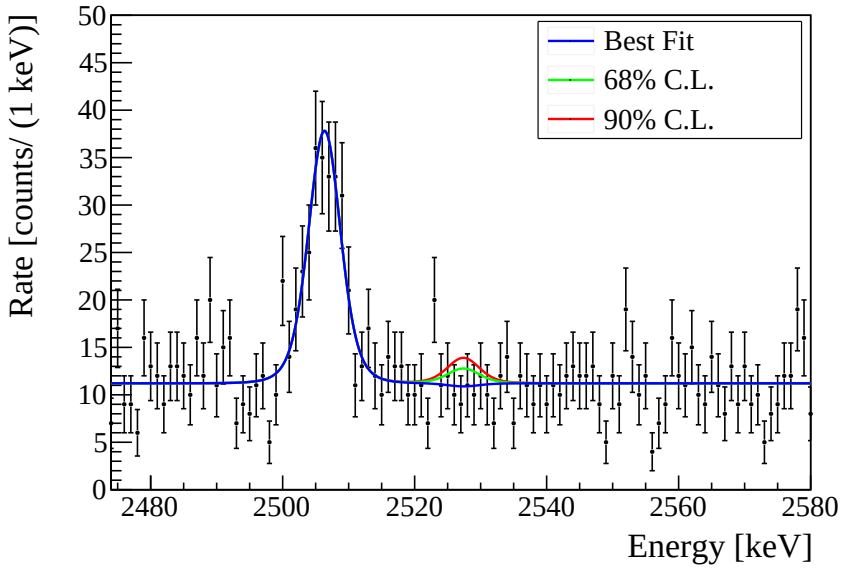

Figure 2.5: Energy spectrum near the Q-value of ^{130}Te (2527 keV) summed over all CUORICINO bolometers. The peak at 2505 keV is produced by the two γs emitted in the β decay of ^{60}Co. It is about 7σ away from the position where the 0νDBD peak is expected and its contribution to the background is negligible. The blue, green and red lines represent respectively best fit, 68% and 90% C.L. on the number of events under the 0νDBD peak.

The natural radioactivity of detector components is often the main background in experiments which search for rare events. Even though the half-lives of the natural decay chains are comparable to the age of the Universe, they are very short compared to the half-life sensitivity of the future 0νDBD experiments ($\geq 10^{26}$y). Therefore, even traces of these nuclides can become a significant background. The primordial radioactive contaminations, mainly ^{238}U and ^{232}Th (see Fig 2.6(a) and 2.6(b)) with their natural radioactive chains, are serious background sources for experiments which look for rare signals below 5 MeV.

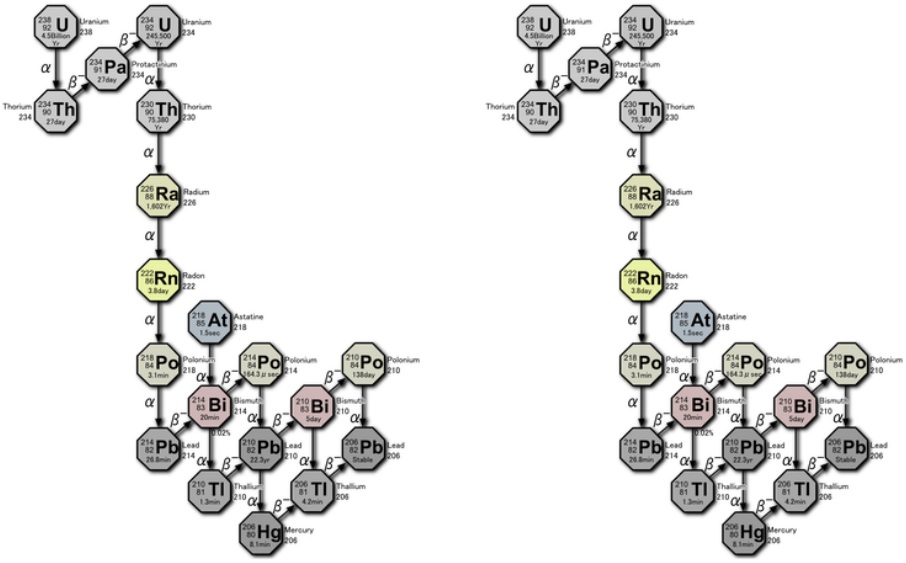

(a) (b)

Figure 2.6: (a): ^{238}U decay chain; (b): ^{232}Th decay chain.

Among those background sources there is the special case of ^{222}Rn and ^{220}Rn, being gases that can easily diffuse through detector materials and because their radioactive daughters can stick to the surface of detector materials. Thorough selection, cleaning and handling of materials is then mandatory for all future 0νDBD experiments in order to reduce these sources of background. Moreover, for preventing the recontamination of a detection system from Radon diffusion, experiments usually use small overpressure of pure nitrogen gas in the detector area surroundings.

In addition to internal backgrounds coming from radioactive impurities in detector components themselves, there are external backgrounds origi-

nated outside the detector. Those backgrounds can be in principle suppressed by placing the detector at an underground location and by enclosing it into a shielding system. In typical underground laboratories the muon flux is indeed reduced by several orders of magnitude, while all the other components of cosmic-ray radiation are negligible and only secondaries are present (e.g. particles produced by muon interaction in the rock). These are neutrons and gamma rays. Also the rock radioactivity is a source of neutrons through the natural fission and (α,n) reactions. The flux of such neutrons is much more intense than the one of muon-induced neutrons. Their spectrum is however softer with an end point at few MeV. Environmental gammas are dominated by rock radioactive emission. Gammas are rather easily shielded with high-Z material like lead and copper, while neutrons are shielded with hydrogen-rich materials (for the neutron thermalization) mixed with high neutron capture cross section nuclei. Finally, veto systems can be used for the rejection of the background induced by muons interaction in the set-up.

Another source of background is related to the cosmogenic activation, like radioactive isotopes produced by cosmic-ray interactions with the detector component. It can be controlled by reducing the exposure of materials to cosmic rays and by avoiding the use of nuclei with large activation cross-section.

The so called "surface contamination" background plays a role in almost all detectors, but it is in particular crucial for fully active detectors, as the case of bolometers; it is originated by the α particles, emitted from radioactive nuclei located within few μm of a surface facing the detector, that lose part, or even all, of their energy in the few microns of this dead layer before reaching the detector. The resulting energy spectrum will be a continuum between 0 and 4 - 8 MeV (the common α energy) covering, unfortunately, all the possible Q-values. Furthermore, the same mechanism occours in the case of surface contaminations on the detector itself. All these background sources must be considered when selecting the detector materials and technology: only in this way the experiment will reach the sensitivity to test the inverted hierarchy region of neutrino masses.

The GERmanium Detector Array (GERDA) [69] is one of the two planned experiments devoted to the study of 0νDBD decay of ^{76}Ge. The detector, which is operating at LNGS, is composed by bare HPGe detectors enriched to 86% in ^{76}Ge, submersed bare into liquid argon. This cryogenic liquid serves both as cooling medium for detector operation and as passive and active shield. Thanks to these shielding and to pulse shape analysis, the GERDA collaboration plans to reach a background level as low as 10^{-4} counts/keV/kg/y in the 0νDBD region. The experiment is planned

to operate in two phases of increasing mass. In phase-I are employed the former Heidelderg Moscow and Igex HPGe detectors, eight detectors (∼18 kg) enriched to 86% in ^{76}Ge. The background index in phase-I is aspired to be lower by at least one order of magnitude compared to the predecessor experiments, that is $< 10^{-2}$ counts/keV/kg/y). The installation of the full array of enriched phase-I detectors finished at the end of 2011 and the physics data taking has just started. After one year of data taking, the first phase of the experiment is foreseen to reach a sensitivity of $3 \cdot 10^{25}$y being able therefore to confirm or reject the claim of observation in ^{76}Ge. In the second phase, with a total detector mass of the order of 40 kg, a sensitivity of $2 \cdot 10^{26}$y (corresponding to $m_{\beta\beta}$ in the range 0.07÷0.3 eV) will be reached in three years of data taking. Depending on the results that will be achieved in the first two phases, a third phase with a mass of the order of one ton could be supported.

The Majorana experiment also will search for 0νDBD of ^{76}Ge using HPGe detectors [70, 71]. It will be located in the Sanford Underground Laboratory, in South Dakota (USA). The Majorana project is following a phased approach. The first phase, called the Majorana Demonstrator, will consist of a 40 kg module of high-purity Ge, 30 kg of which will be enriched to 86% in ^{76}Ge. The goal of the Demonstrator is to achieve a background level at or below 4 count/(ton·y) in a 4 keV wide region of interest around the ^{76}Ge 0νDBD Q-value at 2039 keV. After a year of running, the Demonstrator should be able to set a limit on the half-life sensitivity of $T^{0\nu}_{1/2} > 10^{26}$ y and address the claim of 0νDBD detection in ^{76}Ge. The Majorana Collaboration is engaged in R&D on detector design, especially p-type, point-contact Ge detectors, and on signal processing for identifying multi-site interactions in segmented Ge detectors. The collaboration eventually aims to build a ton-scale experiment and may join with the GERDA Collaboration to undertake the larger experiment.

With the same technique used in CUORICINO , the CUORE experiment [72] will operate an array of 988 TeO_2 bolometers with a total mass of 760 kg (204 kg in ^{130}Te). In the assumption of a background level of 10^{-2} counts/keV/kg/y a sensitivity of $2 \cdot 10^{26}\, y$ in five years of data taking is expected ($m_{\beta\beta} < 0.02 \div 0.1$ eV). CUORE should start data taking in 2014. The first tower, called CUORE-0 ,will be assembled and cooled down in the CUORICINO cryostat before the end of spring 2012. Depending on the background level, its 1σ sensitivity will lie between $(6.6 \div 9.4) \cdot 10^{24}$ y in two years of live time. These experiments will be described in details in next Chapters.

EXO [73] (Enriched Xenon Observatory) is a multi-phase program to search for the 0νDBD decay of ^{136}Xe. The first phase, EXO-200, consists of a 200 kg detector currently operating in a laboratory space in the Waste Isolation Pilot Plant (WIPP), New Mexico (USA). The detector consists of a time projection chamber filled with liquid Xe enriched at 80% in ^{136}Xe, able to detect both ionization and scintillation light produced by the two electrons emitted in double beta decay. An R&D effort is underway to develop a technique to tag double beta decay events by atomic spectroscopy of the daughter $^{136}Ba^{++}$ ions. The Ba tagging would provide the capability to reject all backgrounds except for 2νDBD events. In the first phase of the experiment the detector prototype is operating without ion tagging. The expected sensitivity in this phase will be of $\sim 8 \cdot 10^{25}\, y$ ($m_{\beta\beta} < 0.1 \div 0.2\,\mathrm{eV}$). With a total mass of 1 ton, the final EXO detector will reach a sensitivity of $2 \cdot 10^{26}\, y$ ($m_{\beta\beta} < 0.03 \div 0.06\,\mathrm{eV}$). Recently, the EXO Collaboration reported for the first time the observation of the 2νDBD in ^{136}Xe, with $T^{2\nu}_{1/2} = 2.11 \pm 0.04(stat) \pm 0.21(sys) \cdot 10^{21}$y [35]. The observed decay rate is very interesting because provides new input to matrix element calculations and to the search for the 0νDBD.

The KamLAND-Zen [74] detector is a modification of the existing KamLAND detector, carried out in the summer of 2011, in order to search for 0νDBD decay of ^{136}Xe. The major modification to the existing KamLAND detector was the construction of an inner, radiopure and transparent vessel to hold the dissolved Xenon. In the first phase of the experiment 400 kg of ^{136}Xe will be dissolved in the liquid scintillator of the KamLAND detector and up to 1 ton in the second phase. Very recently, the KamLAND-Zen Collaboration reported the first result based on an exposure of 77.6 days with 129 kg of ^{136}Xe [36]. The measured two-neutrino double-beta decay half-life was $T^{2\nu}_{1/2} = 2.38 \pm 0.02(stat) \pm 0.14(syst) \cdot 10^{21}$ y, consistent with the recent measurement by EXO-200 described before. It was also obtained a lower limit for the neutrinoless double-beta decay half-life, $T^{0\nu}_{1/2} > 5.7 \cdot 10^{24}$ y at 90% C.L. The measured energy resolution at 2.6 MeV is (6.6 ± 0.3)%.

Several other next generation experiments have been proposed or are in the R&D phase.

SuperNEMO [75] is a proposed upgrade of NEMO-3 with at least 100 kg of source mass of various isotopes, as ^{82}Se or ^{150}Nd. It is currently in the R&D phase. The projected sensitivity for the half life is of $2 \cdot 10^{26}$y, corresponding to an upper limit on the effective Majorana mass in the range $0.04 \div 0.1\,\mathrm{eV}$. Compared to other experiments, SuperNEMO has the unique capability to accommodate several different 0νDBD isotopes in the detector

and to change the source foils rather easily. This feature could be of great importance to check for a possible positive signal seen by other experiments.

The SNO+ Collaboration plans to fill the SNO acrylic vessel with Nd-loaded liquid scintillator in order to search for 0νDBD decay of ^{150}Nd [76]. This isotope has the second highest Q-value, 3.37 MeV, and the fastest predicted neutrinoless double beta decay rate due to its large phase space factor (see Tab. 2.1). The high Q-value is a significant advantage, being above most radioactive γ backgrounds. However, the study of feasibility of enriching Nd is still in progress.

The CANDLES project (CAlcium fluoride for the study of Neutrinos and Dark matters by Low Energy Spectrometer) proposes the use of CaF_2 scintillating crystals to attempt to detect 0νDBD of ^{48}Ca [77]. The crystals would be immersed in liquid scintillator providing shielding and an active veto against external backgrounds. Among the DBD isotopes, ^{48}Ca has the highest Q-value, 4.27 MeV. This places the signal well above the energy region of γ natural radioactive lines. Unfortunately, the natural abundance of the isotope is very low (only 0.187%) and enrichment procedures are very complicated. Therefore, many tons of crystals would be needed for a competitive new-generation experiment.

Experiment	Technique	Isotope	Mass [kg]	$T^{0\nu}_{1/2}$ [y]	$m_{\beta\beta}$ [eV]	Status
Gerda-I/II	HPGe	^{76}Ge	18/40	$2 \cdot 10^{26}$	$0.07 \div 0.3$	in progress
Gerda			1000	$6 \cdot 10^{27}$	$0.01 \div 0.04$	R&D
Majorana-dem	HPGe	^{76}Ge	30-60	$(1\text{-}2)\cdot 10^{26}$	$0.07 \div 0.3$	R&D
Majorana			1000	$6 \cdot 10^{27}$	$0.01 \div 0.04$	R&D
CUORE-0	bolometers	^{130}Te	40	$9 \cdot 10^{24}$	$0.2 \div 0.4$	in progress
CUORE			740	$2 \cdot 10^{26}$	$0.02 \div 0.09$	in progress
EXO-200	TPC	^{136}Xe	200	$6 \cdot 10^{25}$	$0.1 \div 0.2$	in progress
EXO			1000	$8 \cdot 10^{26}$	$0.03 \div 0.06$	R&D
Kamland-Zen	liq. scint.	^{136}Xe	400	$4.5 \cdot 10^{26}$	$0.04 \div 0.08$	in progress
Kamland-Zen			1000	$\sim 10^{27}$	$0.03 \div 0.05$	R&D
SNO+	liq. scint.	^{150}Nd	56	$4.5 \cdot 10^{24}$	$0.1 \div 0.3$	in progress
SNO+			1000	$3 \cdot 10^{25}$	$0.04 \div 0.1$	R&D
Super-NEMO	tracking	^{82}Se	100-200	$2 \cdot 10^{26}$	$0.04 \div 0.1$	R&D

Table 2.2: Comparison of: experimental technique, isotope under investigation, source mass, expected half life sensitivity, $m_{\beta\beta}$ sensitivity and current status for the most sensitive next generation 0νDBD experiments. For the values of expected sensitivities see references in the text.

2.2 The bolometric technique

A bolometer is a particle detector that measure the energy deposited by incident radiation based on the temperature change of the detector. It generically consists of three parts: an absorber, a temperature sensor and a weak thermal link connecting the absorber to a thermal reservoir (Fig.2.7). The temperature variation induced by a deposit of energy E in the detector

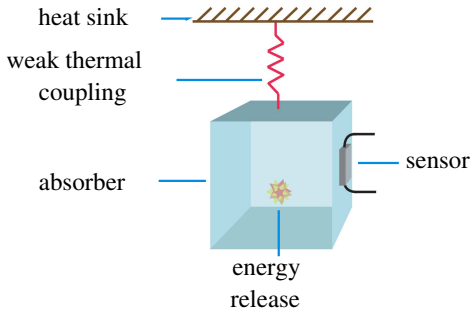

Figure 2.7: Schematic representation of a bolometric detector: an absorber is connected to a heat sink through a weak thermal coupling and a sensor for signal readout is attached to the absorber.

is given by

$$\Delta T = \frac{E}{C} \tag{2.6}$$

where C is the heat capacitance of the absorber material. The absorbed heat flows trough the conductance until an equilibrium condition with the heat sink is reached. The absorber then returns to the base temperature with a time constant τ= C/G, where G is the thermal conductance of the link:

$$\Delta T(t) = \frac{E}{C} exp(-\frac{t}{\tau}) \tag{2.7}$$

With these simple considerations, it is clear that in order to obtain big and fast signals the capacitance of the absorber must be small. This requirement can be fulfilled only operating at cryogenic temperatures, between 10 and 100 mK. Indeed, at low temperature the heat capacity C of a dielectric and diamagnetic crystal of mass m and molar mass M is given by the Debye T^3 law:

$$C(T) = \frac{12}{5}\pi^4 \frac{m}{M} N_a k_B \left(\frac{T}{\Theta_D}\right)^3 \quad T < \Theta_D \tag{2.8}$$

where Θ_D is the Debye temperature, which depends on the specific material [78].

Since most of the energy transferred from a particle to a detector is converted into heat, a bolometer has an higher intrinsic resolution than

other types of nuclear radiation detectors which measure the component of a particle energy going into ionization or excitation of atomic electrons. The theoretical resolution of a bolometer is indeed limited only by fluctuations in the number of phonons exchanged with the heat sink that maintains the base temperature of the bolometer. An estimate of this thermodynamic limit on the resolution of a bolometer may be obtained by considering that the elementary excitation, the energy required to create one phonon, is about $\epsilon = k_B\,T$ so that the number of phonons in a bolometer with energy $E = CT$ is $N = E/\epsilon = CT/k_BT$. Assuming this number of phonons fluctuates according Poisson statistics, the variation in the energy is

$$\Delta E = \Delta N \cdot \epsilon = \sqrt{k_B C(T) T^2} \tag{2.9}$$

a quantity which is independent from the energy. In a real detector, anyway, the energy resolution is strongly degraded due to extrinsic sources of noise, and this contribution become negligible.

2.2.1 Thermalization of deposited energy

Particles can interact with the absorber by scattering on nuclei or on electrons and in both cases the energy is finally converted into phonons. The interaction with nuclei is relevant for α particles: when particles interact with nuclei the released energy produces vibrational excitations and may also produce structural damages of the lattice, where the energy can be stored. If this energy is not converted into phonons, the statistical fluctuation of the number of produced defects can reduce the energy resolution. The fraction of lost energy depends on the incident particle: it is negligible for electron and photons, but it can worsen the resolution to few hundreds eV for an α particle with an energy of some MeV. In the case of scattering on electrons, the interacting particle produces electron-hole pairs in the absorber material. These charge carriers, initially produced in the proximity of the interaction point, spread very quickly in the detector and interact with each other until a quasi-equilibrium condition is reached. Then they undergo interactions with the lattice sites. In this step a large fraction of the initial energy is transferred to the lattice as vibrational excitations (phonons), but it is also possible that part of the energy leaves the crystal or is stored in stable or metastable states. Radiative recombinations of electron-hole pairs with the escape of the emitted photon, non radiative recombinations that take too much time compared to signal development and trapping of electrons and holes in impurity sites or lattice defects can cause a worsening of the energy resolution. Electron-hole pairs recombinations and scattering on

lattice impurities produce high energy and low momentum phonons in the optical branch, which in turn decay in a very short time (of the order of 100 ps) in longitudinal acoustic branch (LA) phonons (see Fig 2.8). As the

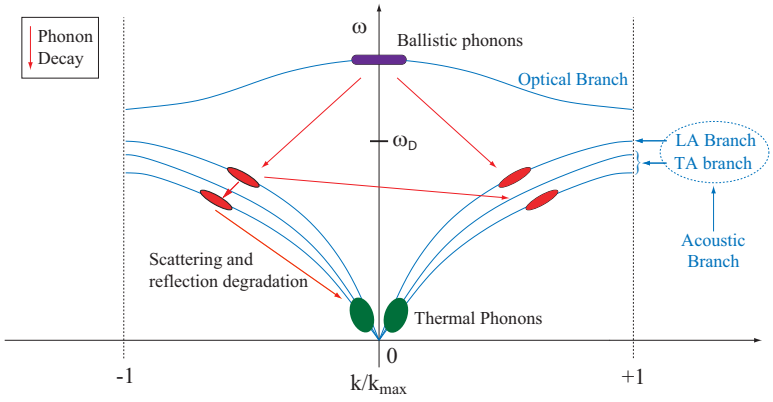

Figure 2.8: Mono-dimensional representation of the phonon dispersion curve.

decay obeys to energy and momentum conservation, each phonon from the optical branch typically produces two LA phonons with opposite momentum and energy of the order of $k_B\Theta_D$. However this energy is still much higher than the average phonon energy in thermal equilibrium. The thermalization proceeds then through phonon-phonon interactions, scattering on impurities and on crystal surfaces. The first mechanism is possible due to the anharmonicity of the lattice potential, and leads to the production of phonons in the transverse acoustic branch. Since the energy degradation through the phonon-phonon interactions becomes less effective when the phonon energy is approaching the equilibrium temperature, the scattering on impurities and crystal surfaces becomes the dominant process in the last stage of thermalization.

2.2.2 Phonon sensor

The phonon sensor is usually a thermistor, a resistive device which converts temperature variations into resistance variations. There are basically two types of thermistors, the Transition Edge Thermistors (TES) and the Semiconductor Thermistors (ST). TES are superconducting films kept at the critical temperature. They have a rather fast response ($\sim \mu$s) but can only work in a narrow range of temperatures. On the other hand ST have

a slower response (∼ms) but can be used in a wider range of temperatures. A parameter characterizing the sensor is the logarithmic sensitivity η:

$$\eta = \left| \frac{d \log R(T)}{d \log T} \right|. \tag{2.10}$$

The above expression implies that:

$$\frac{dR}{R} = \eta \frac{dT}{T} \tag{2.11}$$

where it is evident that the larger is η the higher is the response of the device. Typical values of η are 10 for ST and 100 for TES. In the following, the operating principles of the semiconductor thermistors will be presented being the ones used in the CUORE experiment. Semiconductors are covalent solids that behave as insulators being the valence band full and the conduction band empty, nevertheless the energy gap between valence and conduction band is less than 2 eV. The conduction can then happen only with an activation energy greater than the energy gap. Since kT at room temperature is $\simeq 0.025$eV, the conduction can only happen at higher temperatures. But in case the semiconductor lattice has impurities (extrinsic or doped semiconductors), new energy levels are introduced slightly above the valence band or below the conduction band, depending on the type of atoms inserted. With this technique the conduction can also happen at lower temperatures. The dopant concentration determines the behavior of the solid and the critical concentration that characterizes the transition from metal to insulator. The region near this concentration is called metal-insulator transition region (MIT) [79], at which the material resistivity exhibits a dependence on the temperature. At temperatures lower than 10 K the conduction is dominated by the migration of the charge carries between impurity sites. In this situation electrons are not localized and the conduction happens when an electron jumps from a donor site to another, without using the conduction band (*hopping mechanism*). This migration is due to the tunneling through the potential barrier separating the two dopant sites and it is activated by phonons (see Fig. 2.9). At even lower temperature, the energy of the phonons which are responsible for the conduction mechanism is low and charge carriers migrate also to far impurity sites with free energy levels which are close to the Fermi energy. In this conduction regime, called Variable Range Hopping [80] (VRH), the concentration of minority charge carriers determines the density of states close to the Fermi level. The MIT is set not only selecting the concentration of dopant but also chosing the ratio of acceptor and donor concentrations. In the VRH conduction regime

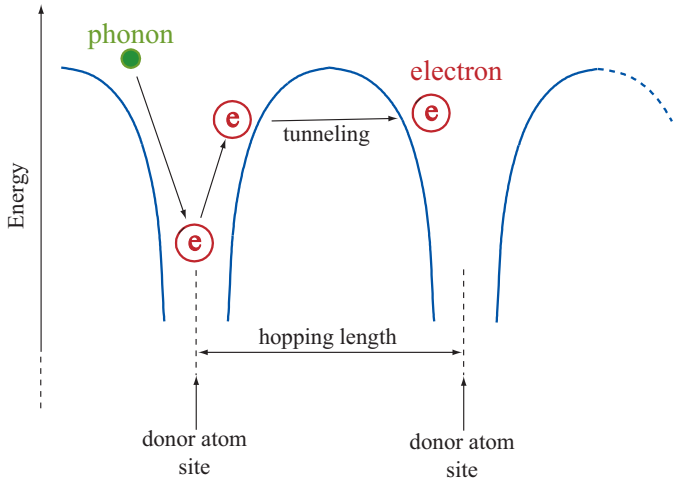

Figure 2.9: Schematic representation of the hopping conduction mechanism.

the resistivity dependence on temperature is described by the law:

$$\rho(T) = \rho_0 \exp\left(\frac{T_0}{T}\right)^{\gamma} \tag{2.12}$$

where $\gamma = 1/2$ and ρ_0 and T_0 depend on the doping concentration.

The expression of the logarithmic sensitivity can be easily derived from the above equation using Eq. 2.10:

$$\eta = \gamma \left(\frac{T_0}{T}\right)^{\gamma} . \tag{2.13}$$

2.2.3 NTD-Ge thermistors

The thermal sensor used in CUORICINO and CUORE bolometers is a Neutron Transmutation Doped (NTD) germanium thermistor operating in the Variable Range Hopping regime [81]. Melt-doped Ge crystals cannot achieve the necessary uniformity due to the effect of dopant segregation. The only technique available for producing uniform doping is NTD: Ge wafers are bombarded with thermal neutron beams that, inducing nuclear reactions, create donor (As and Se) and acceptor (Ga) impurities. The right dopant concentration and the consequent sensor performances are achievable due to the natural abundances of germanium. Wafers are then cut into pieces,

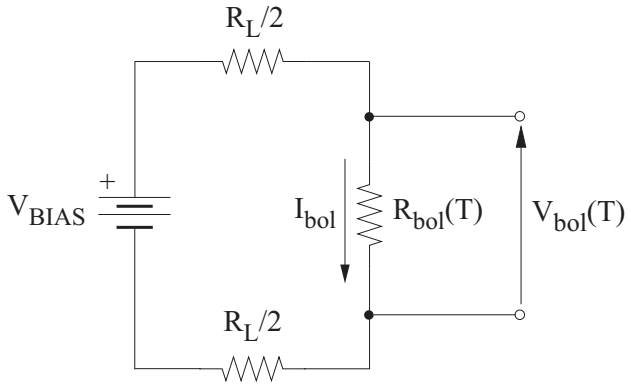

Figure 2.10: Electric scheme of the bias circuit used for thermistor readout.

each of them is a thermistor and its resistance can be expressed as:

$$R = R_0 \exp\left(\frac{T_0}{T}\right)^{\gamma} \tag{2.14}$$

where R_0 depends on the geometry and is roughly $R_0 = \rho_0\, l/S$, being l and S the length and the section of the piece respectively. The parameters R_0, T_0 and γ are determined experimentally. The measurement is made coupling the sensor to a low temperature heat sink using an high conductivity epoxy. The heat sink temperature is then varied ($15-50$ mK) while a steady current flows through the thermistor. Using a calibrated thermometer the parameters can be extracted from a fit to the $R(T)$ characteristic. Typical parameters of CUORE NTD's are:

$$R_0 = 1.15\ \Omega\,, \qquad T_0 = 3.35\ \mathrm{K} \qquad \text{and} \qquad \gamma = 1/2 \tag{2.15}$$

Using these values we can calculate that the static resistance (R_S) at the working temperature $T_S = 10$ mK results to be approximately 100 M$\,\Omega$.

2.2.4 Detector operation

To read out the signal from the NTD Ge thermistor which are coupled to the absorber, the thermistor is biased with the circuit shown in Fig. 2.10. The biasing circuit consists of a voltage source and two load resistors in series with the thermistor. The total resistance of the load resistors is chosen to be much greater than the resistance of the thermistor at the working

temperature so that an approximately constant current $I = V_{bias}/(R_L + R_{bol}) \approx V_{bias}/R_L$ flows through the thermistor. The voltage across the thermistor, $V_{bol} = IR_{bol} \approx V_{bias}R_{bol}/R_L$, is proportional to the thermistor resistance. The thermal information contained in the thermistor resistance is read out by recording the voltage across the thermistor.

The optimal bias voltage is determined independently for each bolometer. As the bias voltage is increased from zero and current flows through the thermistor, power $P = IV_{bol}$ is dissipated as heat in the thermistor. (Figs. 2.11(a) and 2.11(b)). The Joule heating of the thermistor increases its temperature and decreases its resistance, a phenomenon known as electrothermal feedback. The $I - V$ relationship, or load curve, for the thermistor begins approximately linearly at low bias voltages where electrothermal feedback is negligible. As the bias voltage increases, the slope of the $I - V$ curve increases until reaching the inversion point where the thermistor voltage is maximal. At higher bias voltages, the curve reverses direction, and the thermistor voltage decreases while the current in the biasing circuit continues to increase. The working point of the thermistor is a particular point on the load curve set by the bias voltage. The optimal working point is the one where the ratio of signal amplitude to noise level is maximized. In practice the optimal working point is found approximately by scanning the bias voltage in steps and selecting the value for which the signal amplitude is maximized.

A typical pulse produced by a particle interacting in a bolometers is represented in Fig. 2.12.

Using some numbers relative to the CUORE bolometers it is possible to have an idea of the magnitude of the produced signal. A typical value for the absorber heat capacity is $C \approx 10^{-9} J/K$ at $10mK$, thus an energy release of 1MeV would result in a temperature rise of $\sim 0.1mK$. Since the typical voltage drop across the sensor is of few mV in static conditions, the pulse height produced by the energy release of 1 MeV is given by $\Delta V/V \sim \Delta R/R \sim A\Delta T/T \sim 100\mu V$.

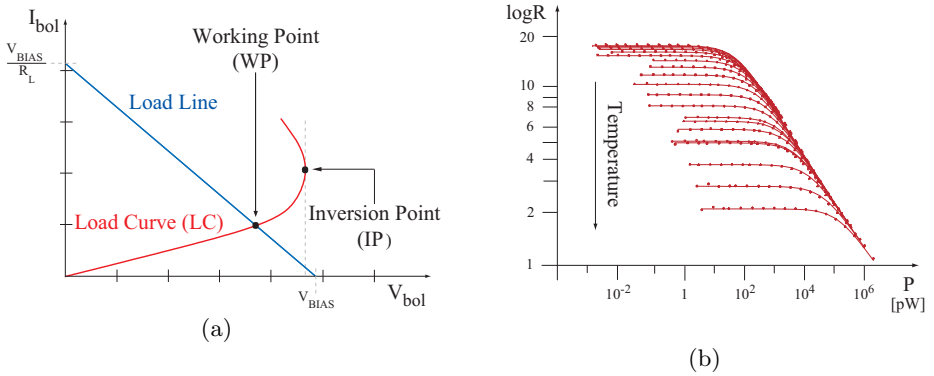

Figure 2.11: On the left, the load curve for an NTD Ge thermistor. On the right, measurements illustrating electrothermal feedback: as the power dissipated in the thermistor increases, the resistance of the thermistor decreases. The different curves were obtained at different base temperatures, i.e. the temperature at P = 0.

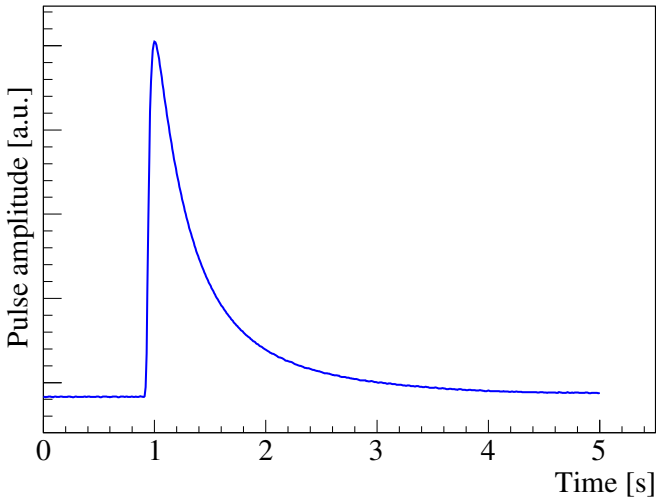

Figure 2.12: Typical pulse shape produced by a particle interacting in a bolometric detector.

Chapter 3

From CUORICINO to CUORE

Introduction

Since Fiorini and Niinikoski first proposed the use of bolometers for rare decay searches in 1984 [82], members of the CUORE Collaboration have operated a series of 0νDBD experiments based on the bolometric technique. Starting with a single crystal bolometer [83], the detectors have been increased in size to arrays of 4, 8 and 20 crystals [84, 85], leading up to the recently completed 62-crystals CUORICINO experiment [46].

Based on this experience, it has been developed the concept for the Cryogenic Underground Observatory for Rare Events (CUORE) [72], one of the most sensitive next-generation experiments searching for 0νDBD of ^{130}Te. The CUORE detector will consist of 988 TeO_2 bolometers arranged in 19 towers, resulting in a scaled-up version of the CUORICINO experiment.

The elementary unit of the CUORE detector, usually called "single module", is a single floor of a tower. The structure and the materials of CUORE single module are almost the same as the ones used in CUORICINO, but huge efforts have been done in order to improve the background rejection and the performances of the bolometers. The final test for the evaluation of all the improvements will be CUORE-0, a single CUORE tower realized using the new assembly procedures, which will be cooled down in the CUORICINO refrigerator.

In this chapter, after an overview of the CUORE experiment, the revision of the CUORICINO single module towards the CUORE single module will be detailed. In order to understand the sources of background and the

related improvements made to overcome it, the CUORICINO background will be also described.

3.1 CUORE: an overview

The CUORE experiment is a next generation 0νDBD decay experiment which will search for 0νDBD of ^{130}Te. The CUORE detector will be a tightly packed array of 988 TeO_2 bolometers, $5\times5\times5$ cm^3 and 750 g each, for a total mass of 741 kg of TeO_2 (see Fig 3.1(a)). Since the tellurium is unenriched, the total mass of ^{130}Te corresponds to 204 kg. CUORE will be operated underground, in the Hall A of the Laboratori Nazionali del Gran Sasso (Fig. 3.2), where the 3400 m w.e. rock shield reduces the muon flux to $\sim 3\cdot10^{-8}\mu$ cm^{-2}sec^{-1} [86] and the neutron flux to $\sim 10^{-6}$n cm^{-2}sec^{-1} [87].

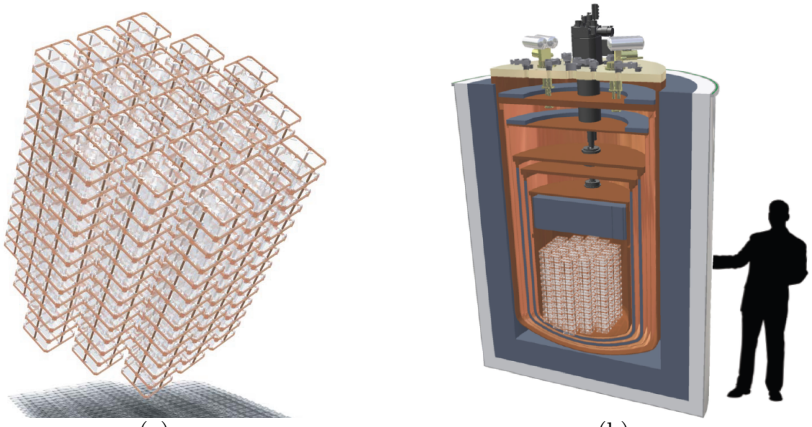

(a) (b)

Figure 3.1: (a): drawing of the 19 towers of CUORE. (b): drawing of the CUORE cryostat in cross-section, revealing the shielding and the array of towers.

The CUORE detector will be housed in a dedicated cryostat and cooled to $\sim$10 mK by a pulse-tube-assisted dilution refrigerator (see Sect. 3.5). To shield the detector from environmental radioactivity and radioactive contaminations of the dilution refrigerator itself, several layers of lead will be used both inside and outside the cryostat, with Roman lead constituting the innermost layer (see Fig. 3.1(b)).

CUORE aims to achieve a sensitivity of the order of 10^{26}y for the half-life of 0νDBD decay of ^{130}Te in 5 years of running. To realize this goal, the

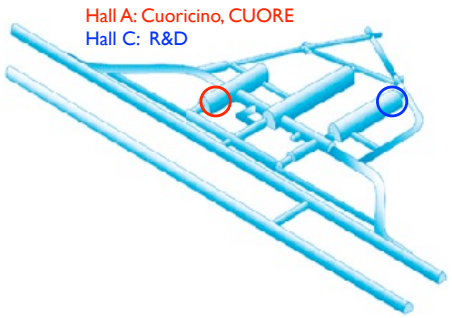

Figure 3.2: Layout of the underground laboratory at LNGS. CUORICINO and CUORE are located in Hall A, and a dedicated R&D facility for CUORE is located in Hall C.

CUORE Collaboration has made an intense effort to understand and control all the sources of backgrounds observed in CUORICINO and to optimize the cryogenic bolometer performances. Improvements in the radiopurity of materials and detector shielding will lead to an expected background level for CUORE <0.01 counts/keV/kg/y in the region of interest around the Q-value of ^{130}Te at 2527.5 keV.

The CUORE goal for the energy resolution is 5 keV FWHM, an improvement from the 7 keV average for the CUORICINO $5\times5\times5$ cm^3 crystals. The improvement is due mainly to the minimization of the mechanical vibrations of the crystals. The CUORE crystals have more stringent tolerances on their dimensions than the CUORICINO crystals in order to ensure that they fit snuggly in their holders; moreover the detector will be mechanically decoupled from the building structure, pumps, and cryocoolers by a carefully designed suspension system in order to suppress the propagation of vibrations to the crystals. The suspension system will be described in details in Chapter 6.

3.2 The starting point: the CUORICINO background

The background observed by CUORICINO can be grouped in two categories, depending on whether it comes from outside the detector (external background) or from the detector itself and the passive materials that sur-

round it (internal background). The external background is produced by neutrons, muons, and natural radioactivity in the underground laboratories. It can be reduced to a negligible level by proper detector shielding, as it will be described in Sect. 3.5. The internal background comes from the radioactive contaminations in the cryostat radiation shields, from the mechanical structure of the tower and from the crystals themselves. Excluding the most external cryostat radiation shields, from which the CUORICINO crystals were protected by a low radioactivity Roman lead layer, there is no way to protect the detector from the internal background sources. The only available solution is to eliminate them by proper material selection and cleaning. As it will be discussed later in details, this is one of the guidelines of the R&D activity for the CUORE experiment.

The energy spectrum measured by the $5\times5\times5$ cm^3 CUORICINO crystals operating in anti-coincidence is shown in Fig. 3.3. It was obtained by summing up the single crystal energy spectra over the whole data taking of the experiment. The anti-coincidence spectrum is obtained using the detector array as a veto, thus selecting events in which only one crystal was hit within a coincidence time window of 100 ms. This allows to accept only 0νDBD decay-like events, namely events that are contained within only one crystal, while background events are efficiently removed.

The CUORICINO average background counting rate in the 0νDBD region is 0.153 ± 0.006 counts/keV/kg/y. The main contribution were identified coming from:

- multi-Compton events from the ^{208}Tl 2615 keV photons, from the ^{232}Th chain, originating from a Thorium contamination of the cryostat shields. The effect of multi-Compton from the 2615 keV line of Thorium can be appreciated looking at the red spectrum in Fig. 3.3. This is a calibration measurement realized exposing the CUORICINO array to Thorium sources placed outside the cryostat. The calibration spectrum is compared with the CUORICINO background spectrum after normalization for having the same intensity on the 2615 keV line. The Thorium sources produce an illumination of the crystals which is not much different from what would be the illumination due to a Th contamination of the cryostat, therefore behaves in a similar way as the source that is supposed to produce the multi-Compton events in CUORICINO background spectrum. This implies that the CUORICINO external shield were thick enough to reduce to negligible level the contribution of muons, neutrons and enviromental γs but the internal Roman lead shield surrounding the CUORICINO array is not

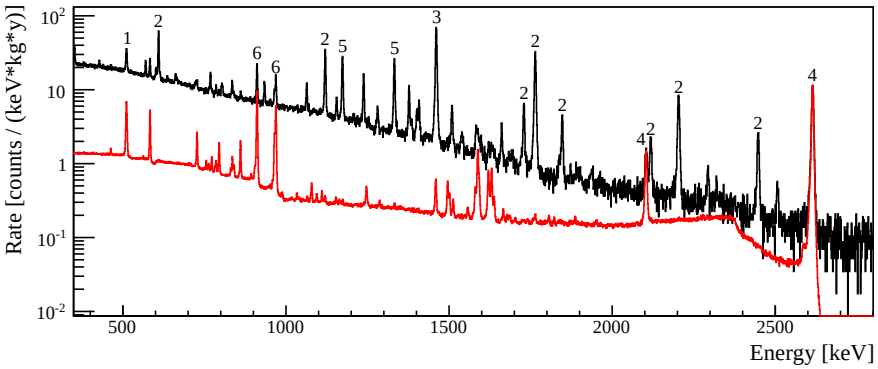

Figure 3.3: Anticoincidence total energy spectrum of all CUORICINO detectors (black). The most prominent peaks are labeled and come from known radioactive sources such as: e^+e^+ annihilation (1), ^{214}Bi (2), ^{40}K (3), ^{208}Tl (4), ^{60}Co (5) and ^{228}Ac (6). The total energy spectrum of all CUORICINO detectors during calibration measurements is also shown (red). For convenience, it is normalized to have the same intensity of the 2615 keV line of ^{208}Tl as measured in the non-calibration spectrum.

sufficient to shield the detector from the radioactivity of the cryostat itself.

- Surface contamination of the TeO_2 crystals in ^{238}U and ^{232}Th (and their daughters). The existence of this background source is evident when plotting the energies of coincident (double-hit) events in facing crystals (see Fig. 3.4). Indeed, when the contamination is on the crystal surface, in a fraction of decays the alpha (or with lower probability the nuclear recoil) escapes the source crystal and enters the facing one. In this case the two detectors record a coincidence event whose total energy yields the Q-value of the alpha transition. When the energies of coincidence events are tracked, the crystal surface contamination gives rise to straight lines with -1 slope, as it is shown in Fig. 3.4. Obviously, those kind of events do not contribute to the 0νDBD rate since they are rejected by the anticoincidence cut. But the same is not true for alpha particles that, exiting the crystals, are stopped in an inert material (such as the copper structure holding the array). These energy-degraded alphas produce a flat continuum extending from the Q-value down to the region of the 0νDBD signal. Similarly, also the

high energy betas emitted by Uranium and Thorium crystal surface contaminations contribute to the background in the 0νDBD energy region.

- Surface Th and/or U contamination of the copper surfaces facing the bolometers. The identification of this contamination was not straightforward. However, the two sources mentioned above cannot account for the background measured in the 0νDBD region. Moreover above the 2615 keV there is a flat background only partially explained by the surface contamination of the crystal. In this region pure gamma contributions are almost negligible while muons and neutrons have been ruled-out on the basis of Monte Carlo simulations and dedicated measurements [88]. On the other hand, degraded alphas (namely alphas that release only part of their energy in the crystal) coming from the surface contamination of the materials directly facing the detectors are a good candidate to account for this background. This contribution is the most difficult to deal with.

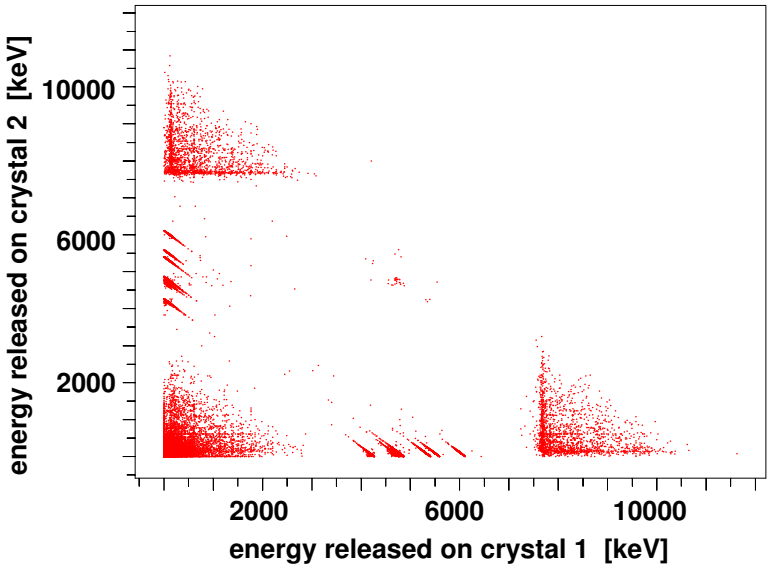

Figure 3.4: Scatter plot of double-hit events obtained with a Monte Carlo simulation of CUORICINO . Surface alpha contamination of the crystals are identified by the slop -1 lines.

3.3 The CUORE single module

The basic module of the CUORE-0 and CUORE detectors is the single floor of a tower: it consists of a 2x2 array of cubic TeO_2 crystal absorbers, containing ^{130}Te as 0νDBD. The crystals are mechanically and thermally coupled to an Oxygen-Free High Conductivity (OFHC) copper holder, acting as heat sink, using Teflon (PTFE) pieces. On each crystal are glued a Neutron Transmutation Doped Ge thermistor, for the detection of temperature variations, and a heater, which provides fixed reference pulses for the bolometer response stabilization. On the external side of the frames, copper pads are fixed to carry the signal to the electronic read-out. The electrical connection between the doped semiconductors and the copper pad is realized with 25 μm diameter gold wires, attached by means of the ball bonding and wedge bonding technique on the two different ends respectively (see Chapter 5 for details). A sketch of the CUORE single module with its main components can be found in Fig. 3.5. In the following paragraphs each component of the CUORE single module will be described in details.

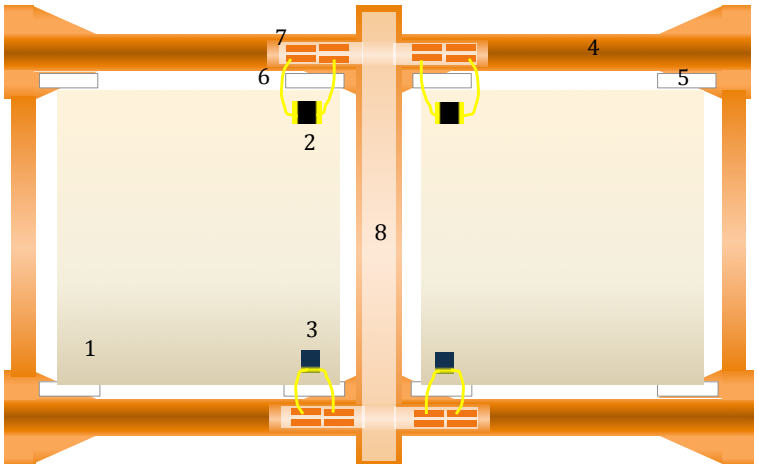

Figure 3.5: Sketch of the CUORE single module, with all its components: 1) the TeO_2 crystal absorber, 2) the NTD-Ge thermistor, 3) the Si heater, 4) the copper frame acting as thermal bath, 5) the PTFE spacers, linking the absorber to the bath, 6) the gold wires, 7) the copper pad and 8) the wire tray for carrying out the electrical signal.

3.3.1 The TeO_2 crystal: source and absorber

The choice of ^{130}Te is due to the necessity of testing 0νDBD in an isotope different from ^{76}Ge but with a competitive sensitivity to obtain crosschecked information. ^{130}Te resulted to be a very good compromise for all the requirements that characterize a double beta decay experiment. Double beta decay of ^{130}Te occurs through the transition

$$^{130}\mathrm{Te} \rightarrow ^{130}\mathrm{Xe} + 2\mathrm{e}^{-} + (2\,\bar{\nu_e})\,. \tag{3.1}$$

The most interesting feature of ^{130}Te compared to other 0νDBD isotopes is the high natural abundance: compared to other materials that usually need to be enriched, the abundance of ^{130}Te allows to build an experiment with natural Tellurium (Fig. 3.6). This is an advantage in terms of costs and material cleanliness, as enrichment procedures often introduce radioactive contaminations.

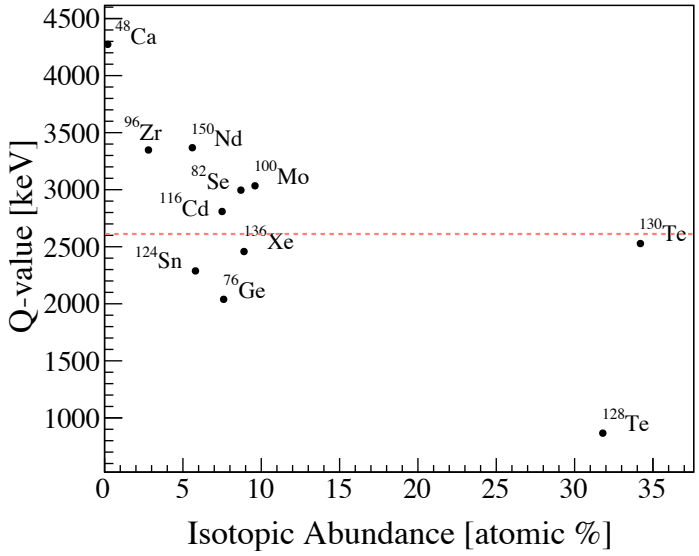

Figure 3.6: Graphical representation of natural abundances and Q-values for several commonly used 0νDBD isotopes. The dashed line at 2615 keV represents the highest energy natural gamma radioactivity. Isotopes with Q-values above this energy benefit of a much lower background.

The transition energy of ^{130}Te ($Q_{\beta\beta} = 2527.518 \pm 0.013$ keV [89]) is not very high compared to other 0νDBD isotopes (Fig. 3.6). In general, experi-

ments using isotopes with Q-values above 2615 keV are affected by a much lower radioactivity background. However, the ^{130}Te transition energy results to be located between the peak and the Compton edge of the 2615 keV line of ^{208}Tl which leaves a clean window to look for the signal. The use of TeO_2 crystals as absorbers for the bolometric search of neutrinoless double beta decay has undergone exhaustive and convincing validations in CUORICINO and its predecessor experiments. Crystals of tellurium dioxide are preferred over pure tellurium crystals due to their thermal and mechanical properties. Pure tellurium was tested as a bolometer, but the mechanical stress of thermal contraction caused excessive damage to the crystal [90]. Tellurium dioxide crystals, on the other hand, can undergo repeated thermal cycling with no observable damage or decrease in performance as bolometers. Moreover, TeO_2 crystals have a higher Debye temperature than pure tellurium crystals, yielding a lower heat capacity and therefore larger pulse amplitudes at the same working temperature.

CUORE TeO_2 crystals production

The production of TeO_2 crystals has been appointed to SICCAS (Shanghai Institute of Ceramics, Chinese Academy of Sciences), where also CUORICINO crystals were grown. Dedicated production lines were set up for the growth and surface processing, in order to reduce the presence of environmental radioactivity in the crystals. In particular, to minimize the influence of long-lived, naturally occurring isotopes, such as ^{238}U, ^{232}Th, ^{40}K and their daughters, extreme care has been devoted to the selection of all materials and ancillaries used for the preparation of the crystals.

Production and certification protocols have been developed and high sensitivity measurements have been performed to check the radio-isotope concentrations in raw materials, reactants, consumables, ancillaries and intermediary products used for crystals production [91]. Moreover, a dedicated cryogenic setup mounted and operated at LNGS is used to validate CUORE TeO_2 crystals. The tests are performed on crystals randomly chosen from each production batch and are aimed at checking their radioactive contamination level and their bolometric performance. The results of this measurements will be detailed in Chapter 4.

The production process of TeO_2 crystals for CUORE is divided into two major phases, crystal synthesis and crystal polishing, which are then divided into several sub-phases. Bulk contamination is a risk in the crystal synthesis phase, while surface contamination is the main concern during the crystal processing.

The raw material synthesis and TeO_2 crystal growth methodology used for the CUORE crystal production are well known ([92, 93]). The key to obtain high purity crystals is the implementation of two successive crystal growth processes with two associated iterations of TeO_2 powder synthesis, as illustrated in Fig. 3.7, and described in detail in [91]. In this way the final radio-pure TeO_2 crystals are grown from a highly pure TeO_2 powder as raw material. For the crystal growth, platinum crucibles are filled with the crystal seed and the raw calcinated powder, sealed and placed into Bridgman furnaces [93].

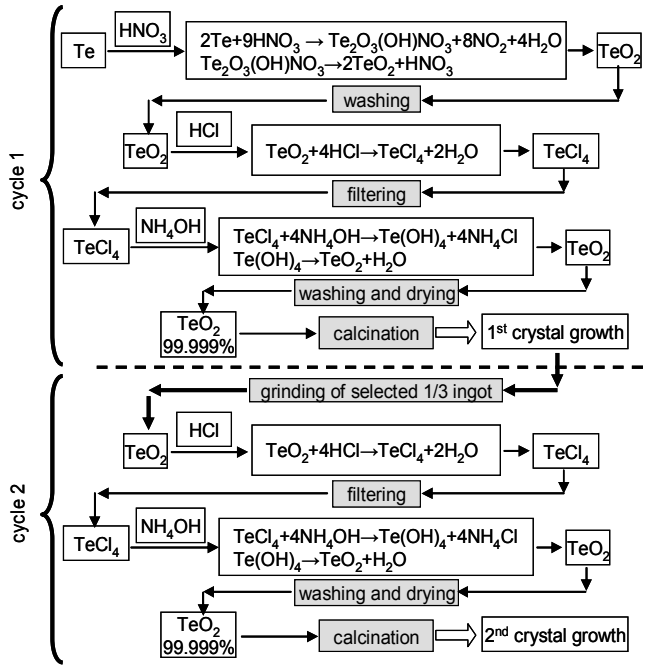

Figure 3.7: Raw material and crystal synthesis protocol applied for the production of CUORE TeO_2 crystals.

After the crystals growth a preliminary mechanical process (cutting, orienting and shaping) is performed on the raw crystal ingots, to bring the crystal shape, dimensions and crystallographic orientation of faces very close to the specifications values. Then, a final mechanical process is performed in a clean room, with also the purpose to clean the crystal surfaces, which may have been contaminated during the rough mechanical processing. The CUORE crystals have very strict specifications concerning dimensions, sur-

face quality and crystallographic orientation. The crystals must have cubic shape with (50 ± 0.050) mm, in order to exactly fit in the mechanical copper holder. In Fig. 3.8 are shown the dimensions of the first batch of CUORE crystals.

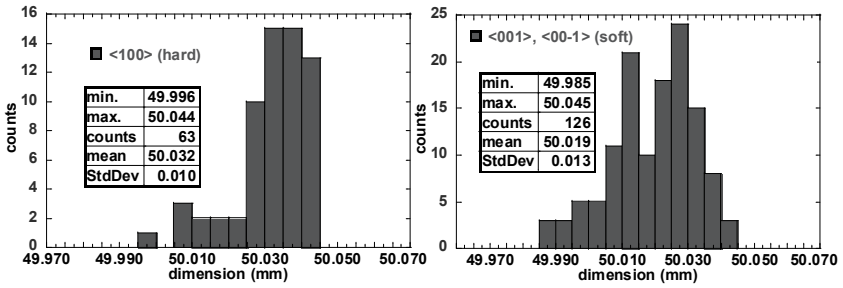

Figure 3.8: Dimensions of the first batch of CUORE crystals.

The final cleaning process is divided into two steps, chemical etching and polishing. The polishing also smooths the crystal faces, in case they have been damaged by chemical etching. The targeted number of atomic layers to be taken away by these two procedures is $\sim 10^4$ in order to eliminate all the impurity atoms which may have been adsorbed on the crystals faces and further might have diffused in its bulk. A special vacuum packaging procedure was also defined in order to reduce the surface radio-contamination risks, especially due to radon exposure in free atmosphere. After the clean room operations, crystals are packed and barcode labelled in a triple vacuum package, stored in groups of six crystals in polyethylene vacuum boxes (see Fig. 3.9(b)) and then delivered to LNGS.

3.3.2 The sensors

As previously introduced, CUORE-0 and CUORE crystals are equipped with two different doped semiconductors for the detection of the temperature variation (the thermistor) and for the measurement stabilization (the heater).

Thermistors

The thermal sensor used in CUORICINO and CUORE bolometers is a Neutron Transmutation Doped (NTD) Germanium thermistor working in the Variable Range Hopping regime.

(a) (b)

Figure 3.9: (a): 5×5×5 cm^3 TeO_2 crystal produced by SICCAS for CUORE-0 and CUORE. (b): the vacuum packed crystals in the boxes ready for the shipment.

These sensors are realized by neutron transmutation doping of ultra-pure Ge in a nuclear reactor to obtain the proper characteristics of resistance and variation of resistance with temperature. Germanium wafers are bombarded with thermal neutron beams that, inducing nuclear reactions, create donor (As and Se) and acceptor (Ga) impurities. The nuclear processes which take place are:

$$\begin{cases} {}^{70}Ge(21\%) + n \rightarrow {}^{71}Ge + \gamma & (\sigma = 3.43 \pm 0.17\, b) \\ {}^{71}Ge + e^- \rightarrow {}^{71}Ga + \nu_e & (t_{1/2} = 11.4\, d) \end{cases} \quad \text{Acceptor}$$

$$\begin{cases} {}^{74}Ge(36\%) + n \rightarrow {}^{75}Ge + \gamma & (\sigma = 0.51 \pm 0.08\, b) \\ {}^{75}Ge \rightarrow {}^{75}As + e^- + \bar{\nu_e} & (t_{1/2} = 83\, min) \end{cases} \quad \text{Donor}$$

$$\begin{cases} {}^{76}Ge(7.4\%) + n \rightarrow {}^{77}Ge + \gamma & (\sigma = 0.16 \pm 0.0014\, b) \\ {}^{77}Ge \rightarrow {}^{77}As + e^- + \bar{\nu_e} & (t_{1/2} = 11.3\, h) \\ {}^{77}As \rightarrow {}^{77}Se + e^- + \bar{\nu_e} & (t_{1/2} = 83\, min) \end{cases} \quad \text{Double donor}$$

To obtain the correct doping concentrations it is important to have a stable neutron flux and to keep under control the neutrons energy distribution: an excess of fast neutrons ($E > 5MeV$) would produce radioactive contaminants such as ^{3}H, ^{65}Zn or ^{68}Ge that would result in an increase of the background. In order to measure the performance of the doped thermistors it is necessary to wait for the decay of the activation product ^{71}Ge (τ=11.4 days). Given the high neutron flux at which the Germanium wafers are exposed, it is necessary to wait at least a few months before the sensor

can undergo a thermal performance test. Therefore, to have at least a rapid indication of the doping concentrations, Germanium wafers are exposed to the neutron flux together with several metal foils. By measuring the concentration of the long lived isotopes produced in these metal foils after the neutron irradiation it is possible to extract the neutron fluxes and thus the corresponding doping levels in the Ge wafers. After the decay of ^{71}Ge, the wafers are treated with heat to repair the crystal structure and are cut to obtain pieces of the desired geometry.

The size of the thermistors selected and tested in the CUORICINO bolometers and in the following CUORE R&D is 3×3×1 mm^3. In the CUORICINO thermistors the gold pads were on the two parallel 3×1 mm^2 sides and the electric contact were provided by 50 μm diameter gold wires welded to the gold pads with the ultrasonic ball-bonding technique ([94]). The thermistor pad geometry and the wire diameter have been changed from CUORICINO to CUORE due to technical and practical issues related to the detector assembly (see Section 5.2). In the new thermistors (with size almost the same as in CUORICINO) the gold pads are not only lateral but extend also on the thermistor upper face, covering two small, parallel areas of about 0.2x3 mm^2. In this way the bonding procedure can be done not only on the thermistor side, but also at the front. The gold wire chosen for the bonding of the new thermistors has a diameter of 25 μm. This kind of thermistor (sketched in Fig. 3.10(a)), with both lateral and frontal pads, is called "wrap-around".

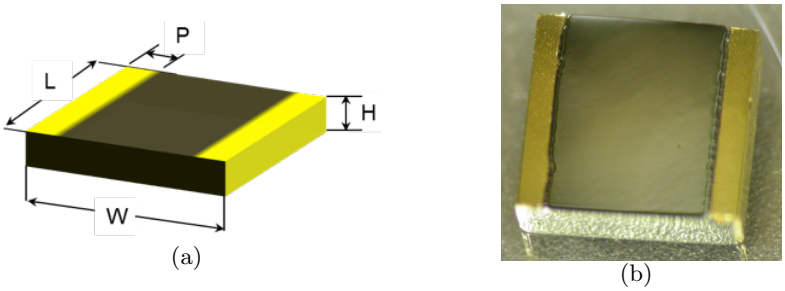

(a) (b)

Figure 3.10: (a): sketch of a CUORE-0 /CUORE thermistor. W is the width, i.e. the distance between the lateral gold pads (∼2.95 mm); L is the length (∼2.90 mm); H is the height (∼0.9 mm); P is the width of the gold pads (∼0.2 mm). (b): a sample of CUORE-0 thermistor.

A sample of a CUORE thermistor is shown in Fig. 3.10(b). Two sets of four CUORE wafers have been already produced and the characteristic

parameters are still under investigation.

Heaters

Low-temperature detectors are sensitive to slow drifts in temperature which can spoil their intrinsically excellent energy resolution. This problem is solved in CUORE by periodically injecting a fixed amount of energy into each crystal via a silicon heater glued to its surface. The pulses of energy from the heaters emulate particle interactions, and the crystal response to these controlled events is used to correct the effects of the temperature drifts in the offline analysis. The CUORE heaters are specifically engineered silicon chips on which a heavily doped meander is realized through the standard processes of silicon planar technology [95]. The meander has a low-mobility metallic behavior at low temperatures, providing a constant resistance of $\sim$300 kΩ. The CUORE heaters, produced at IRST (Istituto per la Ricerca Scientifica e Tecnologica, Trento), consists in a $2.3\times2.4\times0.5$ mm^3 device (see Fig. 3.11). The characterization of the CUORE heaters has to proof that the resistance of each device, besides to be in the proper value range, is stable with temperature variations in conditions close to the working temperatures of the bolometer. Also the uniformity of the implant has to be proved by measuring the pads-to-pads low temperature resistances.

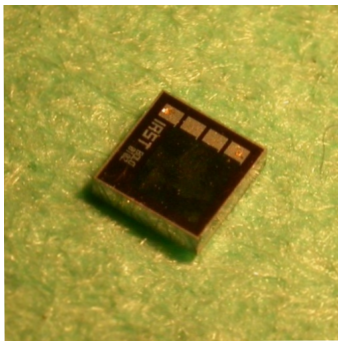

Figure 3.11: Heater sample from the CUORE production.

Thermistor-crystal coupling

The thermistors are mechanically and thermally coupled to the TeO_2 crystal by means of a matrix of small glue spots. The glue is a bi-component epoxy, Araldite Rapid, produced by Huntsman Advanced Materials. The choice of

this glue was based on its low radioactivity and its good thermal conduction, probed since CUORICINO experiment. A matrix of nine dots is used for the thermistors (see Fig. 3.12), while five dots are used for the heaters; the spots range in diameter from 0.5 to 0.8 mm and have an average height of 50 μm. Distributing the glue into separate dots prevents fractures or detachments at low temperatures due to the differential thermal contractions of the TeO_2 crystal and the semiconductor chips.

The glue coupling is a critical component of bolometric detectors which influences the quality of their performance. In CUORICINO the sensor-to-absorber coupling was realized through a manual procedure, and the resulting variability in quality caused a lack of reproducibility in the signal shape and in the detector performance. For CUORE a new partially automated system was developed to obtain definitely more reproducible sensor-to-absorber couplings. The new system is described in Sect. 5.1.

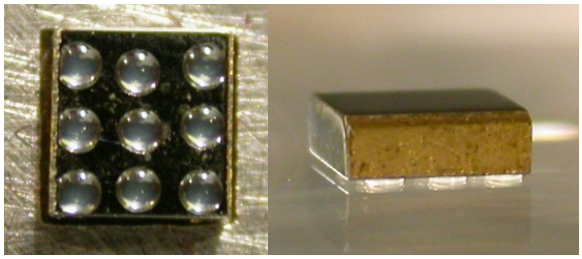

Figure 3.12: Examples of thermistor glued with nine glue dots.

Regarding the electrical connections, in the CUORICINO and CUORE experiments the electric contacts are realized with gold wires ball-bonded on the gold pads of the thermistors and on the aluminum pads of the heater. These connections are also thermal links to the heat bath, being the wires then connected to the Cu parts linked to the holder for electric read-out. The main difference between the CUORICINO and the CUORE approach to bonding is that in the past the gold wires were connected to the chips before being glued onto the absorber, while for CUORE the bonding process is done after the gluing and after all the crystals are placed in the tower. The best way for doing this is having thermistors with pads extended also in their upper face, to allow the execution of frontal bonding. This change is due to several reasons: the first one is the simplification of the gluing procedure, with no delicate wires to deal with; second the fact that it is difficult to access the lateral gold pad once the thermistor is glued on the crystal, being not

available enough working space for the bonding-machine. In this case fixing a broken wire bond requires the disassembly of the tower for the removal of the affected crystal, removing the thermistor from the crystal, repairing the bonds on the thermistor, re-gluing the it to the crystal, and then rebuilding the tower. The other main difference between the CUORICINO and the CUORE bonding is the gold wire diameter, which has been reduced from 50 to 25μm. The reasons of this choice are due to the new way in which the gold wires are connected to the electronic read-out in CUORE . In CUORICINO the gold wires were manually inserted and crimped in Cu pins placed in the holder towards the thermistor. In this way the gold wires were about 1.5 cm long and positioned along an almost straight line. On the contrary the CUORE wiring is realized through special Cu tapes, named Flexible Flat Cable (FFC), glued to wire trays connected to the side of the entire tower: the gold wires are bonded directly on the Cu pads of the tape, performing an about 3 cm long arc; it is difficult to bond thick (50 μm) wires with this shape because their act as springs with high restoring forces, with the risk to break the extremely delicate Au-Cu bonding. For this reason the CUORE wires will have a diameter of 25 μm. To ensure an effective bonding on the Cu pads of the tapes, a dedicated treatment of the copper surface has been studied and implemented (see Sect. 5.2).

3.3.3 The mechanical holder

The two main elements composing the Single Module holder are the copper structure, acting as a heat sink, and the PTFE elements, used for the connection between the crystal and the heat sink. Due to the fact that both these components touch or face the crystals, a big attention is paid to their cleaning procedure.

The copper

The copper holder for the Single Module of the CUORE detector is made out of two frames spaced by four columns (see Fig. 3.13). When more than one module are assembled together, the copper frames are in common between two adjacent floors.

Copper is one of the most used materials for the construction of the experiment CUORE . Its bulk radioactivity content has been measured to be $< 1.6 \cdot 10^{-11}$ g/g in ^{232}Th and $< 4.3 \cdot 10^{-12}$ g/g in ^{238}U. In CUORICINO a large fraction of the background in the double beta decay energy region is due to a deep (>5 μm) surface contamination of the copper mounting

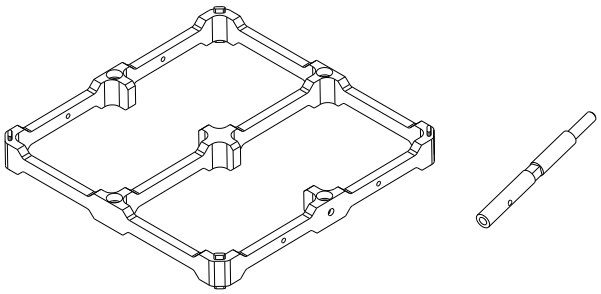

Figure 3.13: Representation of a frames (left) and a column (right) for the CUORE experiment.

structure. This contamination, due to U, Th or Pb and their daughters, does not have a strong signature. Its most evident effect is the presence of a flat background in the energy spectrum extending from above the 2615 keV ^{208}Tl line up to 4 MeV, where the spectrum starts to be dominated by alpha peaks.

For this reason, different copper surface-treatment strategies have been investigated and a final test to define the cleaning procedure for CUORE copper took place in 2009-2010 with the Three Tower Test (TTT) [96]. The TTT detector consisted of three stacked 12-crystal towers, as shown in Fig. 3.14, separated from each other by copper shields. The surfaces of the copper parts in each tower were cleaned using different procedures:

- the copper of the first tower (T1) was treated following the procedure which had produced the best results in previous R&D tests. The copper pieces were cleaned with soap, treated with H_2O_2+H_2O+citric acid and wrapped with several layers of polyethylene.

- The middle tower (T2) was cleaned at LNGS by a new chemical process, which foresees at the beginning a cleaning with simple soap and water, followed by electroerosion with 85% phosphoric acid, 5% butanol, and 10% water, followed then by chemical etching with nitric acid, and by the final passivation with H_2O_2+H_2O+citric acid.

- The copper of the last tower (T3) was cleaned at Legnaro National Laboratory (LNL, Italy) with a procedure consisting of tumbling, elec-

tropolishing, chemical etching, and a magnetron plasma cleaning technique.

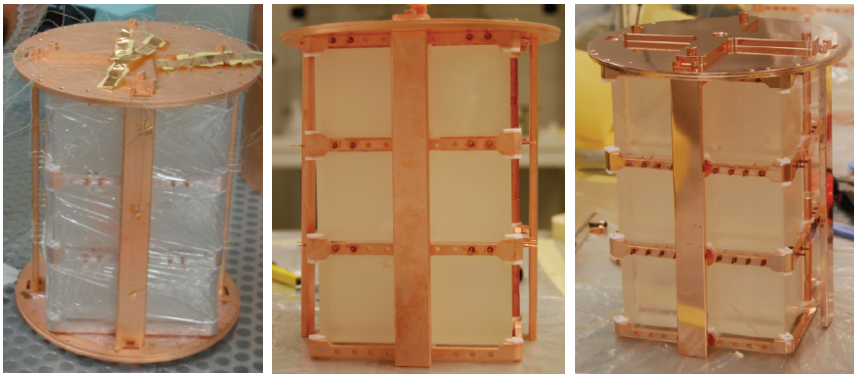

Figure 3.14: The three towers. From left to right: T1, wrapped in polyethylene, T2 cleaned at LNGS, T3 cleaned at Legnaro National Laboratory

The TTT detector was installed in the former CUORICINO cryostat and collected data from September 2009 until January 2010. The TTT measurement showed similar results for the copper treatment adopted for T1 and T3, while the counting rate measured in T2 was slightly larger, indicating that this technique is less effective in reducing copper surface contamination. As a consequence, after the manufacturing, the copper detector components of CUORE will undergo the Legnaro cleaning procedure, which essentially is aimed to remove a tiny layer of the component surface, including dirt and impurities due to handling and manufacturing.

PTFE supports

The PTFE blocks supporting the crystals inside the Cu structure play an important role. The pieces must be manufactured following precise dimensional tolerances to ensure that the correct pressure is acting on the crystals once cooled inside the cryostat. The three different types of holders which will be used are shown in Fig. 3.15.

Since the PTFE blocks will be in contact with the crystals, they must be made from specially selected PTFE and their surfaces must be perfectly decontaminated before use. Before the manufacturing process, the PTFE have been checked with neutron activation analysis, showing the following upper limits for its radioactive contaminations: $1.1 \cdot 10^{-11}$ g/g for ^{232}Th and

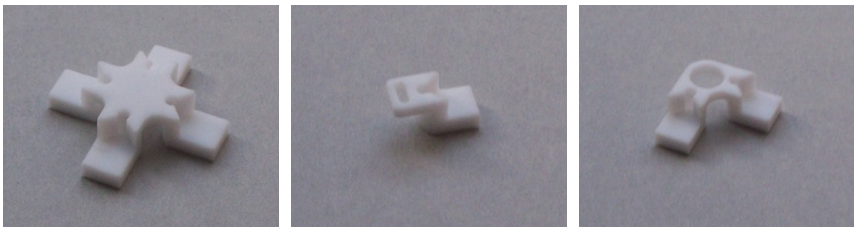

Figure 3.15: The three different types of Teflon block used to hold the crystals in the copper frames.

$3.0{\cdot}10^{-11}$ g/g for ^{238}U. The surface cleaning procedure is divided in two main phases: first the PTFE blocks are washed in an ultrasonic bath with basic soap in order to remove residual contaminants from the manufacturing works (i.e. grease and oil from mechanical workshop). Then the blocks are etched in an ultrasonic bath of nitric acid, in order to remove from the surface of the samples any leftover impurity from the machining. After being rinsed and dried with Nitrogen flux, the samples are stored in a controlled atmosphere. A strict selection of consumables and equipment was also performed, monitoring the radio-purity of the detergents and tools used during the procedure. In Tab. 3.1 are shown, for example, the concentrations of ^{238}U and ^{232}Th in nitric acid (HNO_3) and soap (Micro-90) obtained with ICPMS measurements.

	HNO_3 [ppb]	Micro-90 [ppb]
^{232}Th	<0.002	<0.340
^{238}U	<0.002	<0.670

Table 3.1: ^{238}U and ^{232}Th concentration, measured in part per billion (ppb), of acid and soap used for the surface cleaning of the CUORE PTFE blocks.

The above cleaning protocol was already implemented on the first CUORE blocks received from the manufacturer.

3.4 The detector array

The CUORE detector is a modular device composed by 19 identical towers, closely packed in a cylindrically symmetric structure (see Fig. 3.1(a)).

The tower design has followed several requirements, for example constraints on allowable materials (primarily Cu and PTFE, due to radioactivity restrictions and cryogenics), on the shape and size of the crystal modules (limiting as much as possible the Cu mass, number of pieces, and dimensions) and on the assembly requirements (simple, fast, reproducible and recontamination-free).

The 988 total crystals are arranged in 13 floors, and each floors constitutes a Single Module as described before, with the copper frames which are in common between two adjacent planes. The design of the tower has been optimized in order to reduce the amount of copper near the crystals. On the external side of the frames, 17μm thick Cu strips glued on copper wire trays have the function to carry the signal to the electronic read-out. A scheme of the single CUORE tower is depicted in Fig. 3.16. In order to avoid material recontaminations, all the assembling procedures will be performed in a nitrogen fluxed environment using custom design glove boxes, preventing the exposure of any part of the detector to air.

The tightly packed geometry of the CUORE array provides an intrinsic advantage over a single tower like CUORICINO for rejecting backgrounds that deposit energy in multiple crystals. Many backgrounds, like alpha decays near the surface of a crystal and Compton-scattered gammas, cause interactions in multiple crystals which are effectively simultaneous. An anticoincidence cut will be highly effective in suppressing these backgrounds in CUORE. Furthermore, the inner crystals result to be shielded by the outer crystals.

3.5 Shieldings and cryogenics

The total mass to be cooled in CUORE will be approximately 4 tons: refrigerators with the required characteristics are technically feasible, as it was demonstrated for example by the gravitational wave antenna experiments ([97]). However, due to the stringent radioactivity constraints, the CUORE refrigerator will have to satisfy several additional requirements which are rather uncommon in standard cryogenic devices. The cryogenic system must satisfy the following set of requirements:

- a base temperature lower than 10 mK must be reached for optimal detector operation;
- the cooling power of the refrigerator will have to account for the thermal load produced by the $\sim$2600 read-out wires running from 10 mK

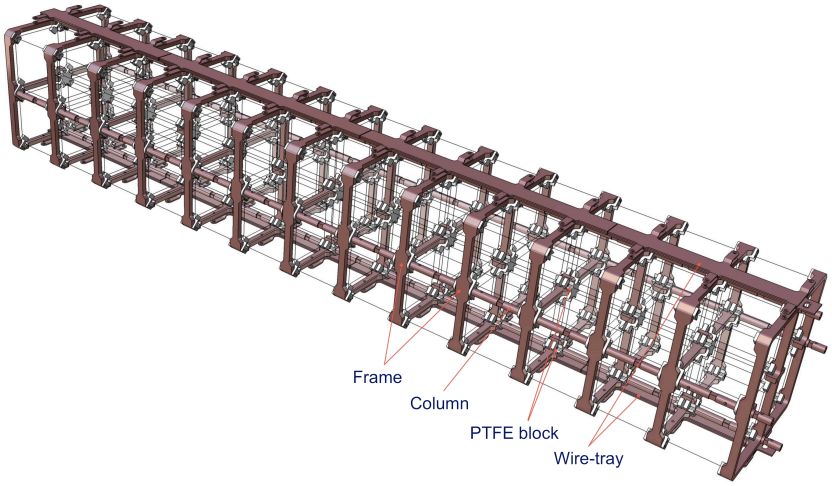

Figure 3.16: 3D model of a single CUORE tower.

to room temperature;

- the vibrations transmitted to the detectors must be minimized, because they would cause noise on the detectors and an increase in the average temperature of the entire array;
- the experience acquired with CUORICINO shows that the experiment must be properly shielded to reduce to a sufficiently low level the background coming from the ^{232}Th contaminations in the cryostat thermal shields;
- for the same reasons, only selected radio-pure materials can be used inside the lead shielding;
- since CUORE is expected to collect data continuously for several years, the cryogenic system must be stable, service-free and capable to operate high duty-cycle.

The CUORE cryogenic apparatus is shown in Fig. 3.17. The cryostat will be made out of six nested vessels. The Outer Vacuum Chamber (OVC), maintained at room temperature, and the Inner Vacuum Chamber (IVC) maintained at 4 K, will be separated by an intermediate radiation shield that will operate at a temperature of $\sim$40 K. Additional thermal radiation

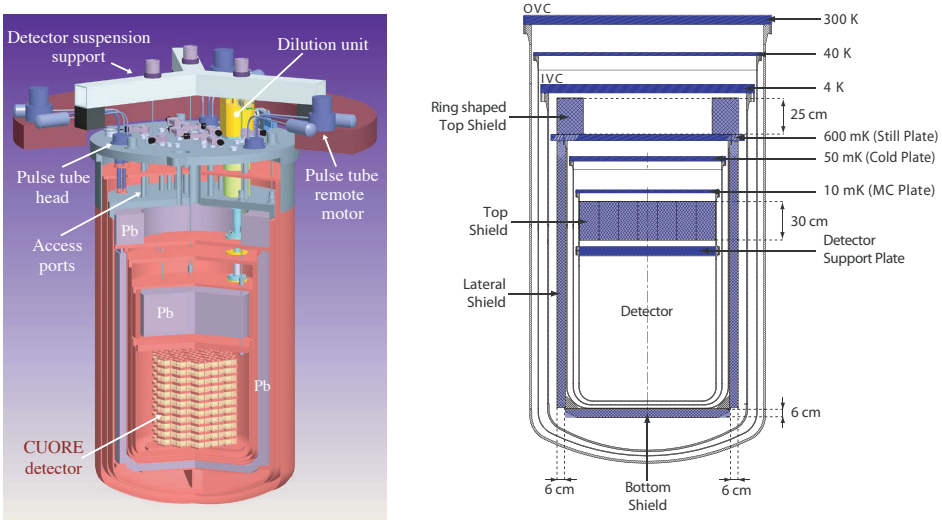

(a) (b)

Figure 3.17: (a): CUORE cryostat. (B): CUORE internal shields.

shielding will be provided by 30 layers of Multilayer Insulation (MLI) covering the 40 K shield and by 10 layers on the IVC shield. The amount of MLI is limited by radioactivity constraints.

The cooling of the IVC and of the 40 K radiation shield will be achieved through five Pulse Tubes mounted on the room temperature OVC top flange. The detector will be cooled by a ^{3}He/^{4}He dilution refrigerator which has been specifically designed for CUORE by Leiden Cryogenics. It is a DRS-2000 unit modified for running without cryogenic liquids: a Joule-Thompson heat exchanger will replace the functionalities usually provided by the 1 K pot. The expected cooling powers are >1.5 mW, 30 μW and 5 μW at 120 mK, 20 mK and 12 mK respectively. Inside the IVC will be installed three thermal shields connected respectively to the Still (∼600 mK), to the Cold Plate (∼50 mK), and to the Mixing Chamber, which is the coldest point of the apparatus (∼10 mK). Inside the cryostat three lead shields will be installed to protect the experiment from environmental radioactivity and from contaminations in the building materials. A lead layer 25 cm thick positioned outside the OVC will shield the detector from the bottom and from the sides. An equivalent shielding from the top will be accommodated inside the cryostat, just above the detector. It will be placed between the mixing chamber plate and the detector, but it will be thermally linked to the 50 mK radiation shield (Cold Plate). With a thickness of 30 cm and a

diameter of 90 cm this shield will weight about 3300 kg. A lead ring-shaped shield placed on the Still flange will close the gap between the lead disk above the detector and the outer room temperature shields. An additional shielding of the sides and the bottom of the detector will be provided by a 6 cm lead layer (m$\simeq$5400 kg) installed just outside the Still shield. To fulfill the radio-purity requirements, the cryostat radiation shields are made of selected high purity copper which has been already stored underground to prevent cosmic ray activation and will be brought to surface only for the construction of the cryostat.

The cold lead disk above the detector and the detector itself are supported by two independent mechanical suspensions. This topic will be discussed in details in Chapter 6.

Chapter 4

CUORE crystals validation

The production of the CUORE crystals was appointed to SICCAS (Shanghai Institute of Ceramics, Chinese Academy of Sciences) and began in 2008. Taking into consideration the goal of CUORE in terms of background (lower than 0.01 counts/keV/kg/y), the radiopurity of the TeO_2 crystals is a crucial issue. As described in Section 3.3.1, the crystal production follows a specific protocol which makes possible the constant monitoring of all the production phases with an especially severe control on the radiopurity of all the employed materials.

Due the strict requirements on the radiopurity of the CUORE crystals, the standard techniques commonly used for the certification of the radiopurity during the various production phases (i.e. ICP-MS measurements, gamma spectroscopy with HPGe detectors and alpha spectroscopy with Surface Barriers Detectors) are not enough sensitive for bulk and surface contaminations of the final products and only bolometric measurements can be used. Cryogenic measurements are thus designed to test the ready-to-use TeO_2 crystals upon their arrival at LNGS.

The crystal validation is performed through experimental runs, each called CCVR (CUORE Crystal Validation Run), in which 4 crystals randomly chosen from a batch coming from SICCAS are mounted in an setup similar to a CUORE single module and are operated at cryogenic temperatures for several weeks in order to test the bolometric performance and the conformity of the crystals to the contract limits in terms of radio-purity. Due to the fact that the data collected on individual crystal runs are statistically too small to check the crystal surface contamination levels, an analysis based on the summed statistics is necessary. In this Chapter the results of the first 5 validation runs are presented, for a total of 18 detectors tested.

4.1 CCVR motivations and goals

The Cuore Crystals Validation Runs have been planned to test the various batches of crystals produced by the SICCAS for the CUORE experiment. The items under analysis are the bolometer performances, which means essentially energy resolution, and the radioactivity, in order to test the compliance of the crystals to the contract limits indicated in Tab. 4.1. The evaluation of the radioactive contamination is performed through the study of the high energy region of the spectrum, where it is expected the contribution of the α lines from uranium and thorium decay chains. Indeed, considering the short range of α particles, their signature is a clear indication of a radioactive contamination within the crystals or on their surface.

Isotope	Allowed Contamination
^{238}U	$< 3 \cdot 10^{-13}$ g/g
^{232}Th	$< 3 \cdot 10^{-13}$ g/g
^{210}Pb	$< 1 \cdot 10^{-5}$ Bq/kg
^{210}Po	< 0.1 Bq/kg

Table 4.1: Contamination limits for the ready-to-use TeO_2 crystals [91].

Here are reported the results of the first five runs, for a total number of 18 crystals tested, which validated the first six batch production. A summary of all CCVR measurement campaign is reported in Tab. 4.2. The test were performed on crystals randomly chosen from each production batch. The 4 crystals tested in CCVR1 (two of them were again tested in CCVR2, see Tab. 4.2) were delivered to LNGS by plane. This was necessary to ensure a fast response on the radioactivity level of the crystals. All the others crystals were transported by ship, in order to minimize their cosmogenic activation.

Detector	Livetime [d]	Crystal tested	Te metal batch
CCVR1	59.9	7, 11, 39, 41	1-2
CCVR2	19.4	7, 11, 76, 97	1-3
CCVR3	43.05	180, 190, 229, 236	4
CCVR4	25.8	313, 340, 354, 380	5
CCVR5	30.3	416, 421, 436, 455	5-6

Table 4.2: Summary of CCVR measurements.

4.2 The experimental setup

Each CCVR setup consists of an array of four crystals, arranged in a single floor which in a first approximation represents the single CUORE module (Fig. 4.1). The four $5 \times 5 \times 5$ cm^3 crystals are enclosed in a pair of copper frames, connected to each other by four small columns, also made of copper. Frames and columns are wrapped with several layers of polyethylene. The crystals are connected to the copper frames by small Teflon supports ehich represent the weak thermal conductance versus the heat sink.

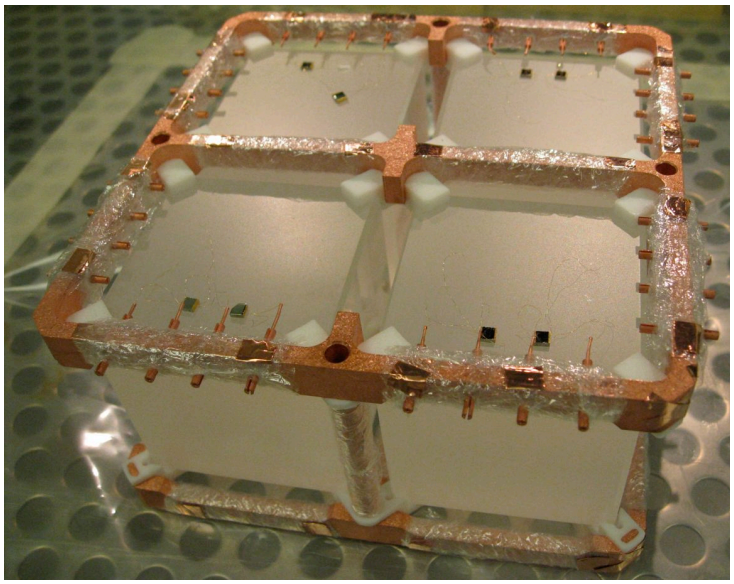

Figure 4.1: CCVR module: the crystals are hold by copper frames wrapped in polyethylene. In the picture are also visible the Teflon holders and the NTD sensors.

The NTD thermistors and Si heaters are manually glued to the crystals in nine separate spots using Araldit Rapid epoxy glue. The electrical connections for the NTD sensor and the Si resistor are executed with two 50μm diameter gold wires, bonded to the metalized surface of the two chips. The wires are crimped at the opposite side into copper pins which pass through the mechanical structure of the single module (see Fig. 4.1).

Most of the CCVR crystals are provided with two thermistors (instead of one) to be sure to have at least one good channel per crystal.

The CCVR measurement were performed using the R&D facility available in the Hall C of LNGS. The experimental setup is composed by a

cryogenic apparatus similar to the one of CUORICINO , but with a smaller space for the detectors. Even if proper shieldings are installed to reduce the background from environmental γs and muons, the Hall C apparatus is affected by a quite high ^{232}Th contamination in the radiation shields. As a consequence the background in the double beta decay region, which is on the left side of the 2615 keV ^{208}Tl peak from the ^{232}Th chain, is rather high compared to CUORICINO . Nevertheless the Hall C apparatus is still suited for the validation on the CUORE crystals, being the main purpose of the CCVR the investigation of the continuous background in the 3-4 MeV region, above the ^{208}Tl line. In the Hall C setup, the electrical signals are carried out from the single module trough a twisted pair of wires, until they reach the mixing chamber of the dilution refrigerator. From this point on, the signal is delivered over a pair of twisted coaxial cables: passing through several thermalization stages, these wires reach the front-end electronic boards through a set of Fisher connectors. The front-end electronics include the biasing circuit, amplifiers, and an antialiasing Bessel filter [98]. The bias voltage is adjustable in the range 0-10 V and has to be set independently for each bolometer as described in Sect. 2.2.4.

4.3 Data analysis

CCVR data processing, aiming to obtain the energy spectra of each detector, follows the procedure described in details in [46]. The raw data are processed with the Optimum Filter (OF) algorithm [99] to maximize the signal-to-noise ratio and to evaluate the best amplitude of each recorded pulse. The idea at the basis of the OF technique is to discard the signal frequency components most affected by noise by constructing a proper filter transfer function, which is determined according to the detector response information. The average pulse and its noise power spectrum density are estimated for each channel from the bolometric pulses and from the noise baseline (i.e. data samples recorded randomly and without triggered events) using a proper averaging procedure. After the pulse amplitude has been evaluated using the OF technique, gain instability corrections must be applied to data. In fact, thermal drifts induce variations in the response of the detectors. In order to avoid this kind of instabilities, the detectors are maintained at a constant temperature by a feedback stabilization circuit, fed by the signal of a thermometer which is attached to the mechanical structure of the detector [100]. Nevertheless, fine gain drift corrections are mandatory.

Thermal instabilities are hence corrected by exploiting a fixed energy

pulse: in CCVRs the gain instability correction was obtained using as reference the 5407.5 keV line from ^{210}Po (the origin of Polonium in the CUORE crystals will be explained in details later).

The stabilized amplitudes are then converted into the corresponding energy values. The energy calibration of the detector is performed by inserting a ^{232}Th source in proximity of the detector, in a position between the cryostat and the external lead shields. Spectra from calibration measurements show several γ peaks that are not visible in standard background measurements, due to the low radioactivity content of the detector materials. A fit is applied to these peaks to obtain a E(ΔV) conversion curve which is then used to obtain the energy spectra. In CCVRs the 5407.5 keV ^{210}Po peak is used in addition to the standard peaks from ^{232}Th. An example of calibration spectrum (Channel2 - CCVR1) is shown in Fig. 4.2. Background measurements between two consecutive calibrations are usually grouped into a "data-set". The data-sets for each CCVR are summarized in the first column of Tab. 4.3.

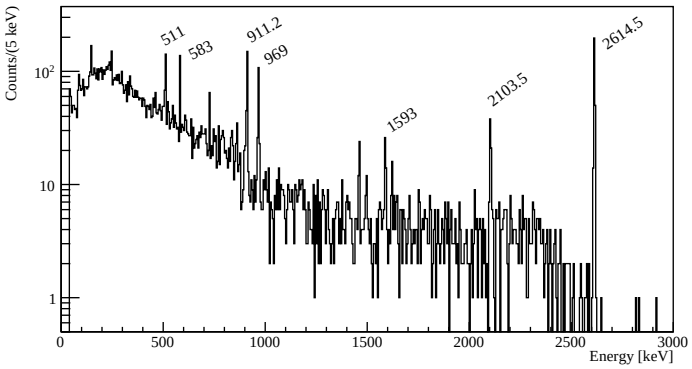

Figure 4.2: Calibration spectrum of Channel2 - CCVR1. Gamma lines from the ^{232}Th decay chain are visible in the spectrum.

The calibration is performed using a third-order polynomial function.

In the case when no calibration run was available (for the CCVR3 and for the data-set 6021 of CCVR4), the calibration has been performed on the sum spectrum of all background runs using the gamma lines at 511 keV, 1460.8 keV, 2614.5 keV and the α line at 5407.5 keV. Tab. 4.3 summarizes the peaks used for calibrating each data-set.

Signal events of each channel are selected only if they satisfy different

Detector	Data-set	Calibration run	Calibration peaks
CCVR1	6010	yes	Th + Po
CCVR2	6012	yes	Th + Po
CCVR3	6014	no	511, 1460.8, 2614.5, 5407.5
CCVR4	6015	yes	Th + Po
CCVR4	6018	yes	Th + Po
CCVR4	6021	no	511, 1460.8, 2614.5, 5407.5
CCVR5	6027	yes	Th + Po
CCVR5	6030	yes	Th + Po
CCVR5	6031	yes	Th + Po

Table 4.3: CCVR data-sets and respective calibration peaks used.

requirement. A common energy threshold for all CCVRs was set to 50 keV. Global requirements on the detector performances are applied following criteria decided a priori on the detector performances (excessive noise level, ADC saturation, etc..). They identify time intervals of bad quality which need to be discarded. These kind of cuts introduce a dead time that is accounted for accordingly, reducing the live time of the interested detector. There are also event-based requirements, which include pile-up rejection, pulse-shape and coincidence selection. The presence of a pile-up prevents the OF algorithm from providing a correct evaluation of the pulse amplitude. The pile-up rejection is performed by imposing an extendable (paralyzable) dead window of 7 seconds to each event. The pulse-shape analysis is used to reject non-physical events. The pulse shape parameters are the rise time and decay time of the OF-filtered waveform and the mean quadratic deviation of raw signal from the average detector response. Examples of discarded events are shown in Fig. 4.3.

As a first step, each CCVR spectrum is corrected for the corresponding efficiency of the event-based cuts (from Table 4.4) and then the spectra are summed together. Four types of spectra are produced for all CCVRs:

- **Total Energy spectrum (TOT)**: it contains all the general cuts and the pulse shape cuts.

- **Anti-coincidence Energy spectrum (M1)**: it contains the events which caused an energy deposition in one crystal only (anti-coincidence cut). For what concerns α particles, this corresponds to bulk events (namely decays where the emitted α particle is absorbed within the crystal itself) and to surface events, generated by decays occurring

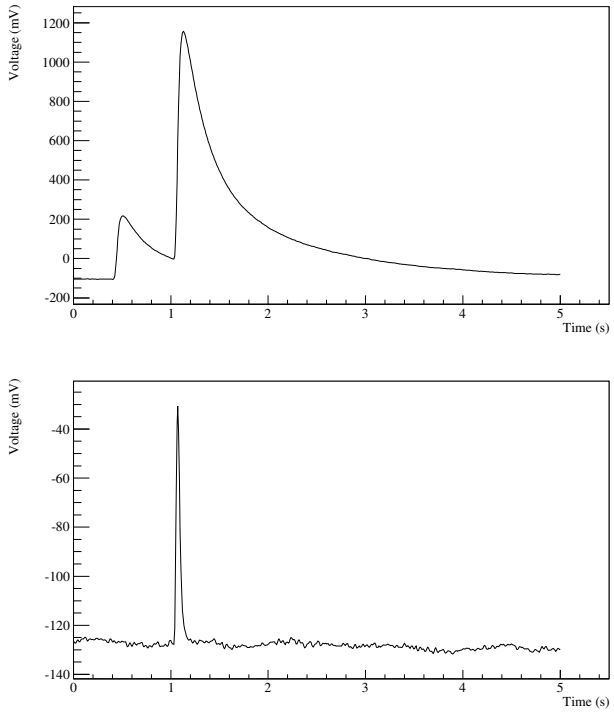

Figure 4.3: Examples of spurious signals. Top: pileup; Bottom: spike event.

on the surface of an inert material which hits a facing crystal, or to α decays occurring on a crystal surface, whose escaping products are absorbed by inert materials.

- **Coincidence Energy spectrum (M2)**: it contains the events which caused an energy deposition in two crystals. For what concerns α particles, these events arise from α decays occurring on a crystal surface faced to another crystal.

- **Coincidence Sum Energy spectrum (M2sum)**: it contains the sum energy of multiplicity 2 events. For instance in the case of an α decay on the surface of a crystal, both the energy of the α particle E_1 in the facing crystal and the corresponding nuclear recoil energy E_2 in the original crystal are detected. In the spectrum M2sum the variable $E_{TOT} = E_1 + E_2$ is plotted.

Fig. 4.4 shows the sum spectra of all CCVRs.

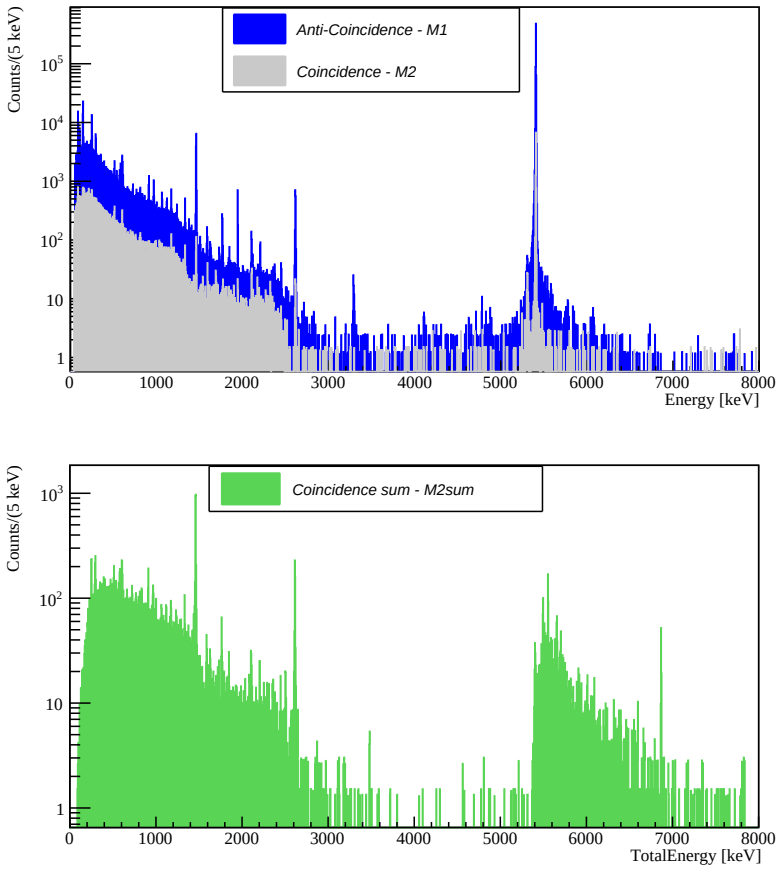

Figure 4.4: Energy spectra for the full CCVR statistics. Top: M1 (blue) and M2 (gray) spectra. Bottom: Sum energy spectrum of multiplicity 2 events.

4.3.1 Efficiency of event-based cuts

Due to the high rate of ^{210}Po events, it was recorded a significant loss of efficiency due to pile-up rejection. The efficiency is evaluated as:

$$\varepsilon_{\text{pile-up}} = 1 - P_{\text{pile-up}} = e^{(-r \cdot T)} \tag{4.1}$$

where P is the probability of a pile-up, r is the counting rate of the events that passed the global cuts described above, and T is the length of a time interval containing an event during which the occurrence of another event would be considered pile-up. The interval T contains a time window after the event during which a double pulse would result and a time window before the event during which the event's baseline would be spoiled by the tail of the preceding pulse. Actually, T depends on the energy of the other event: the higher is the energy of the other event, the longer its tail remains too large. The count rate is channel-dependent and sometimes also time-dependent. In the specific case of ^{210}Po events, the count rate decreases with time due to polonium decay (half-life: 138.38 days).

For the sake of simplicity, an average pile-up reduction efficiency for each CCVR is computed. This will apply to all channels in the full energy range and is calculated using the formula 4.1 with $T = 7$ s and using as value for the parameter r the global counting rate after the general cuts. The average pile up efficiency compared to the efficiency evaluated on each run is shown in Fig. 4.5 for CCVR3 data.

Run	count rate [mHz]	$\varepsilon_{\text{pile-up}}$	ε_{PS}	ε_{AC}	ε_{Tot}
CCVR1	24	0.84 ±0.01	0.96±0.01	0.987±0.003	0.80 ±0.01
CCVR2	19	0.88 ±0.01	0.98±0.01	0.982± 0.005	0.85 ±0.01
CCVR3	16	0.89 ±0.01	0.97±0.01	0.990±0.002	0.86 ±0.01
CCVR4	19	0.88 ±0.01	0.94±0.02	0.987±0.003	0.82 ±0.02
CCVR5	16	0.89 ±0.01	0.98±0.01	0.990±0.003	0.87 ±0.01

Table 4.4: Count rate and efficiencies of event-based cuts for each CCVR.

For the evaluation of the efficiency of the pulse shape cut ε_{PS}, it is used the background peak at 2614.5 keV due to ^{208}Tl. The region of the spectrum containing this peak is plotted with the pulse shape cut applied and also with the complementary cut applied (namely the events that are rejected by the pulse shape cut). Figure 4.6 shows the two spectra with the accepted events at the top and the rejected events at the bottom. The efficiency of the pulse

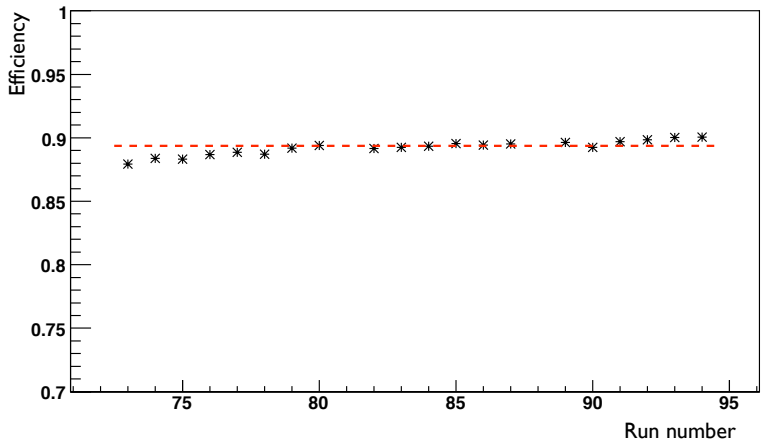

Figure 4.5: Pile up efficiency computed with formula 4.1 on CCVR3 data. Each point represents the pile up efficiency for the corresponding run. The horizontal dashed line represents the average value used for the analysis.

shape cut is determined from a simultaneous fit to both spectra. Values for each CCVR are shown in Tab. 4.4.

The same procedure is applied for the evaluation of the anti-coincidence cut efficiency $\varepsilon_{\mathrm{AC}}$. In this case, instead of the 2614.5 keV line (which is usually in coincidence with other γ lines), it is used the photopeak at 1460.8 keV due to ^{40}K. The results are summarized in Table 4.4. The fit result for CCVR1 data is shown in Fig. 4.7.

4.3.2 Monte Carlo simulations

In order to extract from CCVRs data numerical information on the activity or contamination of a given nuclide in CUORE crystals, it is necessary to rely on Monte Carlo simulations, capable of reproducing the main features of the detector geometry and response.

CCVRs simulations are performed with the GEANT4-based code developed by the CUORE collaboration and described in [101]. The simulation takes into account the energy resolution and the threshold of each detector. For bulk contaminations, an homogeneous distribution of the given nuclide inside the crystals is assumed. For surface contaminations, different depths of the contamination layer (from 0.01 μm to 10 μm) are considered and the contamination density profile is assumed to decrease exponentially with the

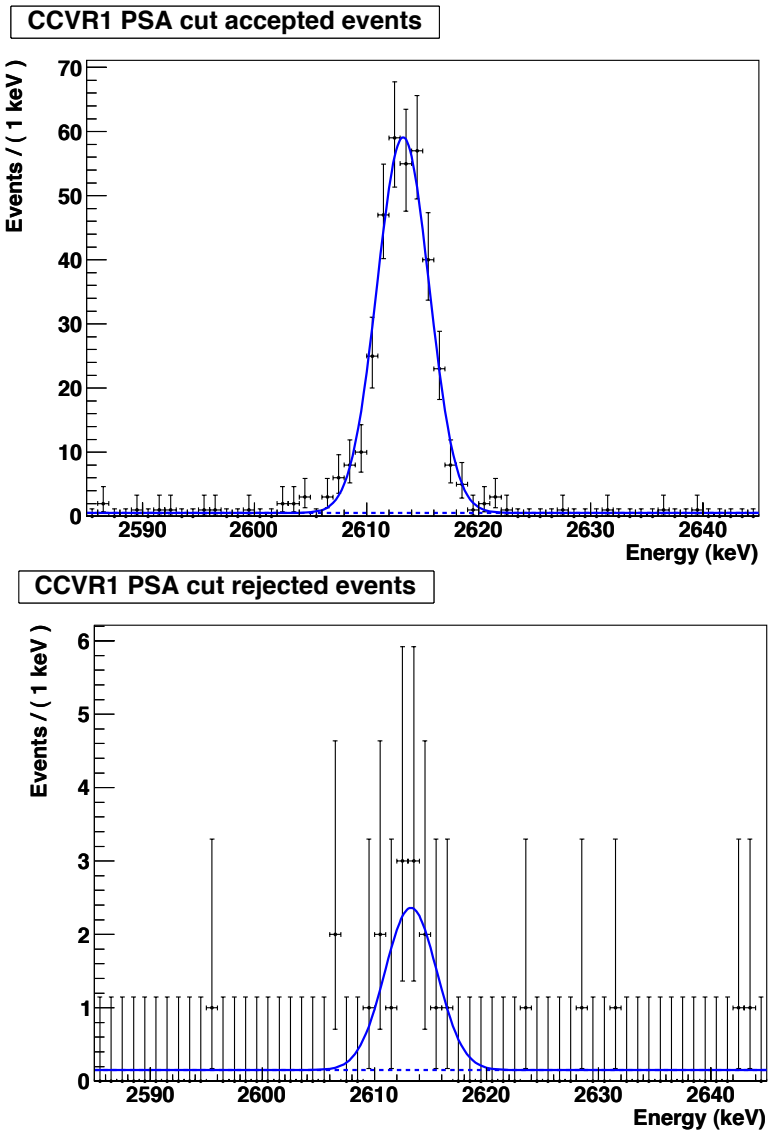

Figure 4.6: Fit to the ^{208}Tl spectrum to determine the pulse shape cut efficiency of CCVR1. On the top are the events that are accepted by the pulse shape cut, and on the bottom are the events that are rejected. The efficiency of the cut is determined from a simultaneous fit to the two spectra.

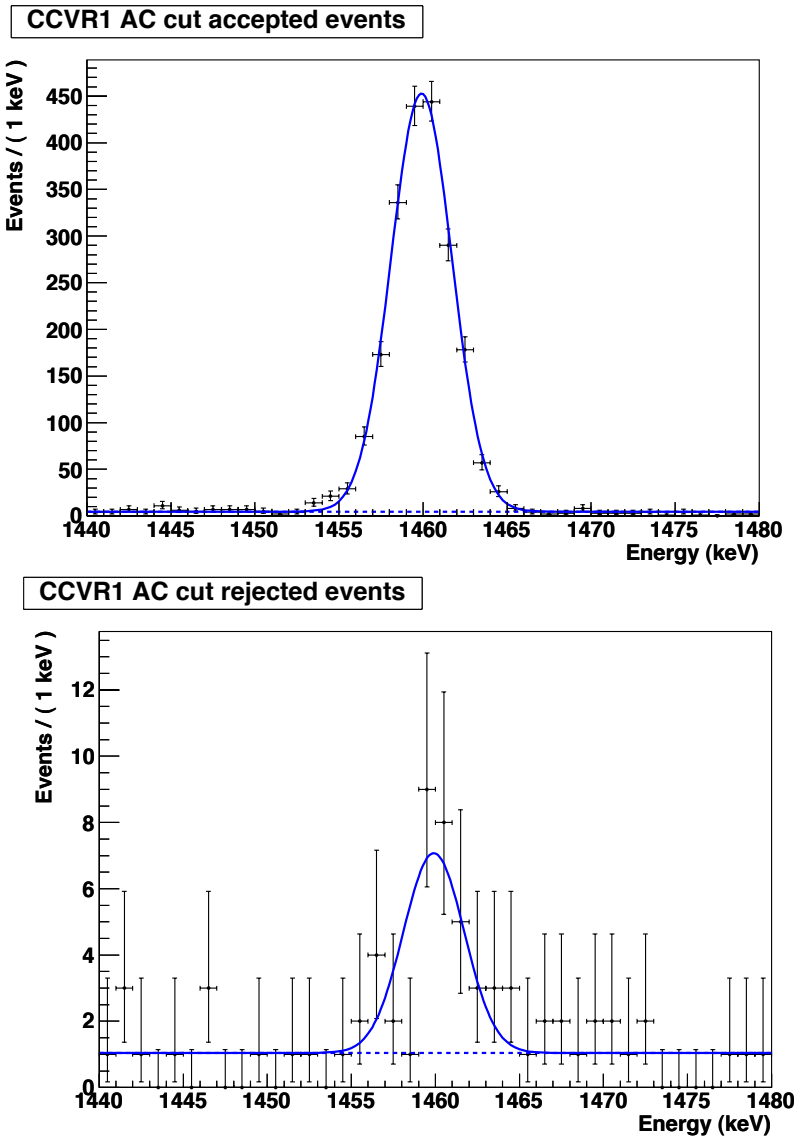

Figure 4.7: Fit to the ^{40}K spectrum to determine the anti-coincidence cut efficiency of CCVR1. On the top are the events that are accepted by the anti-coincidence cut, and on the bottom are the events that are rejected. The efficiency of the cut is determined from a simultaneous fit to the two spectra.

depth from the surface to the bulk of the crystal. In Fig. 4.8 it is shown a M2sum spectrum obtained with MC simulation of surface contamination in ^{238}U with different depth.

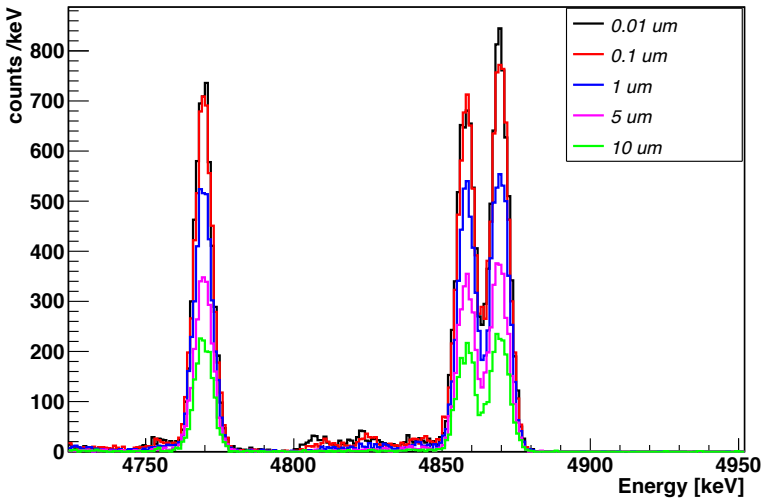

Figure 4.8: M2sum Monte Carlo spectrum obtained simulating a contamination in ^{238}U with different depth.

In CCVR1, $\sim 4\%$ of the measurements had only 2 crystals side by side. This aspect has affected the efficiency calculation of surface contaminations. To take into account this variation from the standard configuration with 4 crystals, 2 different efficiencies are calculated for each Monte Carlo simulation:

- ε_{MC}^{2ch}: corresponding to the CCVR1 configuration with only 2 active crystals;
- ε_{MC}^{4ch}: corresponding to the standard CCVR configuration, with 4 active crystals;

The average efficiency, weighed on the proper lifetime Δt^i, is computed using the formula:

$$\varepsilon_{MC} = \frac{\varepsilon_{MC}^{2ch}\,\Delta t^{2ch} + \varepsilon_{MC}^{4ch}\,\Delta t^{4ch}}{\Delta t^{2ch} + \Delta t^{4ch}} \tag{4.2}$$

4.4 Results on background rates of CUORE crystals

The background rates in various energy regions can be calculated from the energy spectra of all CCVRs. Six energy regions of interest are identified in the spectra and the corresponding count rates for anticoincidence (M1) and coincidence (M2) spectra are calculated. The results for the global spectra are reported in Table 4.5 (errors are statistical only).

	Continuum (2700, 3200) keV	^{190}Pt (3200, 3400) keV	Continuum (3400, 3900) keV
M1	0.19±0.02	0.38±0.04	0.09±0.01
M1-PoSub	0.13±0.02	0.34±0.04	0.06±0.01
M2	0.05±0.01	0.02±0.01	0.025±0.006
M2-PoSub	0.02±0.01	0.01±0.01	0.008±0.008
	U/Th (4000, 5000) keV	^{210}Po (5000, 6000) keV	U/Th (6000, 8000) keV
M1	0.19±0.01	-	0.057±0.004
M1-PoSub	0.13±0.01	-	0.057±0.004
M2	0.04±0.01	-	0.014±0.002
M2-PoSub	0.014±0.007	-	0.014±0.002

Table 4.5: Count rates measured in [counts/keV/kg/y]. Errors are statistical.

The continuum region (2700, 3200) keV is of great interest since it is the region immediately above the Q-value of the neutrinoless double beta decay of ^{130}Te . In the region (3200, 3400) keV a contribution of the α line from ^{190}Pt is expected. This contamination is almost unavoidable for TeO_2 crystals, because Platinum crucibles are used during the production of the crystals, as explained in Sec. 3.3.1. From 4000 to 8000 keV the contribution of the various α lines from U and Th decay chains is expected. In between, there is the region (5000, 6000) keV, which is affected by the ^{210}Po contamination. This produces not only a peak at the α-decay Q-value (5407.5 keV) but also a broad background over the entire region due to misidentified pile-up events (above the peak energy) or due to the escape of the α that releases part of its energy in a inert material (below the Q-value energy). An indication of the rate in this region is of no particular interest, also due to the relative short half-life of ^{210}Po (138.38 days) that guarantees a huge reduction of this count rate when CUORE will start the data taking.

Because of the presence of ^{210}Po, an excess of count rate could appear

in the M1 and M2 spectra below the energy of the 5407.5 keV α decay Q-value, if the contamination of ^{210}Po is close enough to the surface for the α to escape and release part of its energy in an inert material (M1 spectrum) or in a nearby detector (M2 spectrum). This contribution from the M2 spectrum can be estimated, calculating for each energy region the rate of M2 events in which the total energy E_{TOT} lies in the interval (5407.5±50) keV. The M2 count rate subtracted for this contribution is defined as M2-PoSub and reported in Table 4.5 for comparison.

In a similar way the contribution of surface ^{210}Po in the M1 spectrum is evaluated. Because of the geometry of the CCVR setup, coincidences are possible for only 8 of the 24 crystal faces. Consequently the M1 count rate due to ^{210}Po of the remaining 16 faces is assumed to be two times the rate calculated on the M2 spectrum as described above.[1] The M1 count rate subtracted for the surface ^{210}Po contribution is defined as M1-PoSub and reported in Table 4.5.

It is interesting to compare the CCVRs rates with the detectors used previously in the Three Towers Test (TTT) and CUORICINO . This comparison is shown in Table 4.6, where the M1 and M2 count rates for CCVRs are after polonium subtraction.

The notation (2700, 3900) refers to the combination of both the continuum region (2700, 3200) keV and (3400, 3900) keV, excluding the ^{190}Pt energy region of (3200, 3400) keV. It can be inferred that:

- in the region (2700, 3900) keV the CCVRs anti-coincidence rate is compatible within 1.8 σ with the corresponding TTT value;
- in the region (4000, 5000) keV, as already measured in the TTT run, a reduction in the count rate with respect to CUORICINO is observed;
- in the region (5000, 6000) keV a comparison is not possible since CCVR is affected by the high rate of ^{210}Po. This is due to the fact that in CCVRs only recently grown crystals are measured, unlike in the TTT run or CUORICINO ;
- in the region (6000, 8000) keV, as already measured in the TTT run, a reduction in the count rate with respect to CUORICINO is present. However, the CCVR count rate is greater than the TTT value, probably because of the presence of mis-identified pile-up (in M1) or coin-

[1] In some of CCVR1 measurements ($\sim$ 4% of the CCVR lifetime) only two facing crystals were active. The extrapolation of M2 counts to M1 is performed considering that the coincidence analysis is sensitive only to 2 over 12 faces.

		Continuum (2700, 3900)keV	U/Th (4000, 5000)keV
CCVR	M1	0.09±0.02	0.13±0.01
	M2	0.015±0.007	0.014±0.003
TTT	M1	0.052 ±0.008	0.28±0.02
	M2	0.009±0.003	0.0018±0.005
CUORICINO	M1	0.104 ±0.002	0.522±0.003
	M2	0.009± 0.001	0.084±0.001
		^{210}Po (5000, 6000)keV	U/Th (6000, 8000)keV
CCVR	M1	-	0.057±0.004
	M2	-	0.014±0.002
TTT	M1	1.30±0.07	0.025 ± 0.004
	M2	0.09±0.01	0.005 ± 0.002
CUORICINO	M1	0.846±0.004	0.099 ± 0.001
	M2	0.173±0.002	0.0163 ± 0.0004

Table 4.6: Count rate comparison with previous detectors, measured in [counts/keV/kg/y]. Here CCVR values are after polonium subtraction. Errors are statistical.

cidences (in M2) with ^{210}Po events, extending above 6000 keV. This contribution should decay away with ^{210}Po.

4.5 Results on bulk contaminations of CUORE crystals

Bulk contaminations in CUORE crystals are expected from:

- ^{210}Po, as a result of the chemical affinity between polonium and tellurium;
- natural contaminants, like ^{238}U and ^{232}Th with their radioactive-decay chains;
- ^{210}Pb, as a result of the deposition of lead nuclei produced by ^{222}Rn decays, during the crystal handling in free atmosphere;
- ^{190}Pt[2], due to the fact that platinum is used in several phases of the crystal production cycle. As described in Sec. 3.3.1, Platinum crucibles are used for the calcination of TeO_2 powder used for the crystal growth and the growth crucibles are made of platinum foil. The central part of the as-grown crystal ingot is selected for the CUORE crystals in order to avoid the risk of platinum contamination on the surface of the crystal due to possible diffusion during the growth process. Possible Pt contaminations are therefore in the bulk of the CUORE crystals.

The ^{210}Po activity is determined from a fit to the anti-coincidence rate vs. time behaviour (see Sec. 4.5.1).

For ^{238}U and ^{232}Th (see Sec. 4.5.2), the limit on the level of contamination is determined from the intensities of the α peaks in the anti-coincidence spectrum of all crystals, or from integrals centered at the peak position if the peaks are not visible. This is because an α decay from bulk contamination releases the entire Q-value of the reaction (α energy + nuclear recoil) in a single crystal.

For ^{210}Pb, the limit on bulk contamination is determined from a fit in the energy region (40, 60) keV in a subset of CCVRs data with high statistics and low threshold (see Sec. 4.6).

[2]The radionuclide ^{190}Pt is primordial and thus always present in natural platinum.

4.5.1 ^{210}Po bulk activity

The ^{210}Po activity can be measured from the intensity of 5407.5 keV line in the anti-coincidence spectrum. The plot in Fig. 4.9 shows the global rate of ^{210}Po events over time for CCVR1. For each channel the ^{210}Po events are selected in a $\pm$ 20 keV window around the energy of the α line. The units

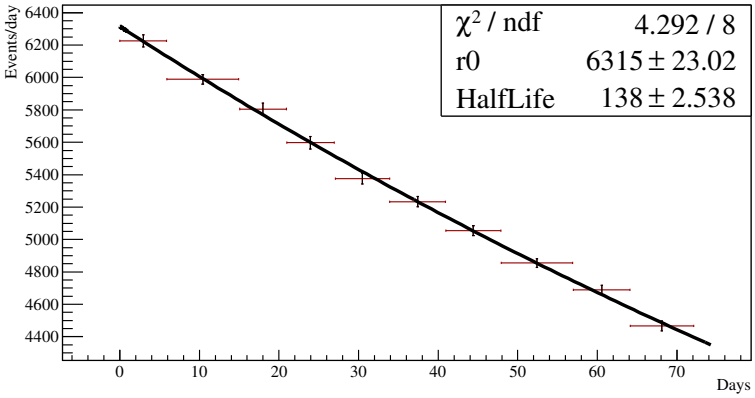

Figure 4.9: Global rate of ^{210}Po events over time for CCVR1. The fit result is overlayed.

on the x-axis are days passed since the start of the first background measurement. Each point represents a group of measurements whose livetime is at least 5 days. The horizontal error bars indicate the beginning and the end of each group of runs, and they are for visualization only. Each point is corrected with the corresponding rate-based efficiency, calculated with the equation (4.1). A larger dead time window (9 seconds instead of 7 seconds) compared to the rest of the analysis is used, to be more conservative in the removal of pile-up pulses.

The fit function is a pure exponential:

$$r(t) = r_0 e^{(-ln2\ t/T_{1/2})} \tag{4.3}$$

where r_0 is the rate at the beginning of the measurement and $T_{1/2}$ is the ^{210}Po half-life.

The half-life of the exponential decay has been evaluated for all CCVRs and it is shown in Table 4.7: it is in good agreement (1 σ) with the half-life of ^{210}Po (138.38 d). This indicates that the ^{210}Po contamination is out of equilibrium and it is not fed by ^{210}Pb.

Run	Half-life [days]
CCVR1	138.0± 2.5
CCVR2	132.3 ± 14.7
CCVR3	139.4 ± 6.3
CCVR4	137.8 ± 11.5
CCVR5	136.6 ± 9.1

Table 4.7: ^{210}Po half-life for all CCVRs. The activity has been fitted using an exponential function. All the values are consistent (within 1 σ) with 138.38 days.

From the value of r_0 returned by the fit for each CCVR and for each crystal, the ^{210}Po activity at the beginning of the measurement is extracted as follows:

$$A[\text{Bq/kg}] = \frac{r_0}{86400[\text{s/day}]\ m[\text{kg}]} \tag{4.4}$$

where m is the crystal mass.

Knowing the time elapsed since the "crystal birth date" (growth completed, before the cut and shape) and the start of the measurement, the ^{210}Po activity at production is computed.

The ^{210}Po activities for each CCVR and for all crystals are reported in Table 4.8. The results for crystals 007 and 011, measured first in CCVR1 and again in CCVR2, are consistent.

All crystals tested in the first five CCVRs are well below the limit of 0.1 Bq/kg imposed to the crystal producers.

4.5.2 U/Th bulk contaminations

^{238}U and ^{232}Th bulk contaminations are evaluated from the anti-coincidence spectrum summed over all CCVRs. For each of the peaks reported in Table 4.9, the number of counts (corrected by the efficiency of the event-based cuts from Table 4.4) is estimated within an energy window of $\pm 6\ \sigma$ around the Q-value. A σ of 2.2 keV is used, corresponding to the average between the values of the ^{210}Po peak σs for each CCVR, weighted by the corresponding lifetime of that run (see Sect.4.9 for details on the energy resolution evaluation).

Using the Bayesian approach, the upper limits N_u at 90% C.L. are obtained, assuming 0 expected background counts and a flat prior for the

CCVR	Crystal	^{210}Po activity [Bq/kg]
1	041	0.0257 ± 0.0001
1	011	0.0510 ± 0.0005
1	039	0.0229 ± 0.0001
1	007	0.0414 ± 0.0004
2	076	0.021 ± 0.004
2	011	0.07 ± 0.02
2	096	0.055 ± 0.006
2	007	0.047 ± 0.015
3	190	0.0078 ± 0.0005
3	236	0.0159 ± 0.0005
3	180	0.0203 ± 0.0008
3	229	0.0283 ± 0.0008
4	340	0.032 ± 0.004
4	313	0.005 ± 0.001
4	354	0.039 ± 0.004
4	380	0.040 ± 0.004
5	455	0.019 ± 0.002
5	416	0.024 ± 0.003
5	436	0.032 ± 0.003
5	421	0.020 ± 0.003

Table 4.8: ^{210}Po activity at production time for all CCVRs crystals.

signal [102] (see Table 4.9).

Chain	Nuclide	Energy [keV]	Half-life	N_u 90% C.L.
^{238}U	^{238}U	4270.0	4.47E+09 y	11.7
	^{234}U	4858.8	2.45E+05 y	20.8
	^{230}Th	4770.0	7.54E+04 y	24.9
	^{226}Ra	4870.6	1599 y	30.0
	^{218}Po	6114.7	3.05 min	7.4
^{232}Th	^{232}Th	4082.8	1.4E+10 y	5.9
	^{212}Bi	6207.1	60.55 min	13.5

Table 4.9: 90% C.L. limits on the number of events ascribed to several nuclides from uranium and thorium decay chains. For each nuclide it is also shown the Q-value and the half-life of the α decay.

The upper limit on the activity for each nuclide is calculated using the following formula:

$$A_u[\mathrm{Bq/kg}] = \frac{N_u}{\varepsilon_{MC}\, T[\mathrm{s}]\, m[\mathrm{kg}]\, \Gamma} \tag{4.5}$$

where ε_{MC} is the Monte Carlo detection efficiency, T the CCVRs live-time, m the crystal mass and Γ the branching ratio of the nuclide. In this analysis a total containment of the anti-coincidence events in the crystals is assumed (ε_{MC} =1). Results are shown in Table 4.10.

The upper limit for confidence level of 90% for U/Th bulk contaminations are then calculated in the hypothesis of secular equilibrium within the uranium and thorium decay chains. Results for the total CCVRs data are shown in the last column of Table 4.10.

In the most conservative approach, the bulk contamination limit on ^{238}U and ^{232}Th is set considering the most active nuclide for each chain. The upper limit at 90% C.L. for uranium and thorium bulk contamination are:

$$\begin{aligned} ^{238}\mathrm{U} &< 5.3 \cdot 10^{-14}[\mathrm{g/g}] \\ ^{232}\mathrm{Th} &< 2.1 \cdot 10^{-13}[\mathrm{g/g}] \end{aligned}$$

Both values of the upper limits are within the contract specification of $3{\cdot}10^{-13}$[g/g]. For the ^{238}U decay chain, the contribution from ^{210}Pb is treated separately (see Sec. 4.6).

Chain	Nuclide	Upper limit [Bq/kg]	Upper limit [g/g]
^{238}U	^{238}U	2.5E-07	2.0E-14
	^{234}U	4.7E-07	3.6E-14
	^{230}Th	5.7E-07	4.4E-14
	^{226}Ra	6.7E-07	5.3E-14
	^{218}Po	1.6E-07	1.3E-14
^{232}Th	^{232}Th	1.3E-07	3.1E-14
	^{212}Bi	8.4E-07	2.1E-13

Table 4.10: Upper limits at 90% C.L. on the activity and on the bulk contamination of uranium and thorium decay chains in the hypothesis of secular equilibrium.

It is important to note that the above upper limits are calculated under the hypothesis that the observed counts for each nuclide are entirely due to a bulk contamination of that nuclide. This is a conservative hypothesis since there is not a clear indication (for example a line) that such a bulk contamination actually exists and that the observed counts are not due to background of some other origin.

4.6 ^{210}Pb activity

During the production of CUORE crystals great care is devoted in order to minimize the exposure of the crystals to free atmosphere, in order to avoid recontamination of radon and its daughters, like for example ^{210}Pb. This contamination leads to low-energy electrons and γ radiation from the decay of ^{210}Pb and a continuum up to 1.16 MeV from the β decay of the ^{210}Bi daughter nucleus. Moreover, the α decay of the daughter ^{210}Po can contribute to the continuum background in the double beta decay energy region.

In the CCVRs crystals the ^{210}Pb contamination cannot be estimated from ^{210}Po, because this contamination is out of equilibrium (see Sec. 4.5.1). The only available signature is a combination of a beta spectrum (end point 16.96 keV) with a de-excitation energy of 46.5 keV (in most of the cases through a conversion electron). This decay produces a broad signature in the energy region (40, 60) keV, whose shape depends on the location of the Pb contamination.

Several simulations are performed both for a bulk contamination and for a surface contamination with exponential density profile and contamination depth varying from 0.01 μm to 10 μm. Even if, for the sake of simplicity, a common energy threshold of 50 keV is set for all CCVRs, there are subset of data where the threshold can be set to a lower value in order to look for this signature. CCVR1 data are used because they strike a balance between high livetimes (CCVR1 has the highest statistics) and good bolometer performances. Only for the CCVR1 data, the analysis is repeated with an energy threshold of 40 keV. The anti-coincidence spectrum between 40 and 60 keV is fitted with an exponentially decreasing background allowing the presence of a ^{210}Pb spectrum with a shape taken from a Monte Carlo simulation. The free parameters of the fit are the two parameters of the exponential background and the total number of counts from ^{210}Pb. The fit is repeated for each Monte Carlo simulated contamination. The number of ^{210}Pb events is compatible with zero within the error for all signatures. An example of Monte Carlo spectrum for a ^{210}Pb bulk contamination and the corresponding fit to the experimental spectrum is shown in Fig. 4.10. The upper limit at 90% C.L. on the number of ^{210}Pb counts is $N_u = 1.644\ \sigma$, where σ is the error on the number of counts returned from the fit. The upper limit on bulk contamination is computed using Eq. 4.5. The upper limit on surface contamination is extracted using the following formula:

$$A_u[\mathrm{Bq/cm^2}] = \frac{N_u}{\varepsilon_{MC}\ T[\mathrm{s}]\ S[\mathrm{cm^2}]} \tag{4.6}$$

where ε_{MC} is the Monte Carlo detection efficiency, T is the livetime and S is the surface area of a crystal (150 cm^2). The results are shown in Table 4.11. The upper limit on the activity for bulk contamination is below the contract limit of 10^{-5} Bq/kg.

4.7 Results on surface contaminations of CUORE crystals

Surface contaminations of CUORE crystals are expected from the same nuclides listed in Sec. 4.5, except for ^{190}Pt, which is only present in the bulk. Uranium and thorium surface contaminations can be investigated identifying coincident events in two facing crystals: surface contamination of an α-decaying nuclide should appear in the total energy spectrum (M2sum in Fig. 4.4) as a peak at the Q-value of the decay because the total energy (α + nuclear recoil) is collected by the two facing crystals. At the same time,

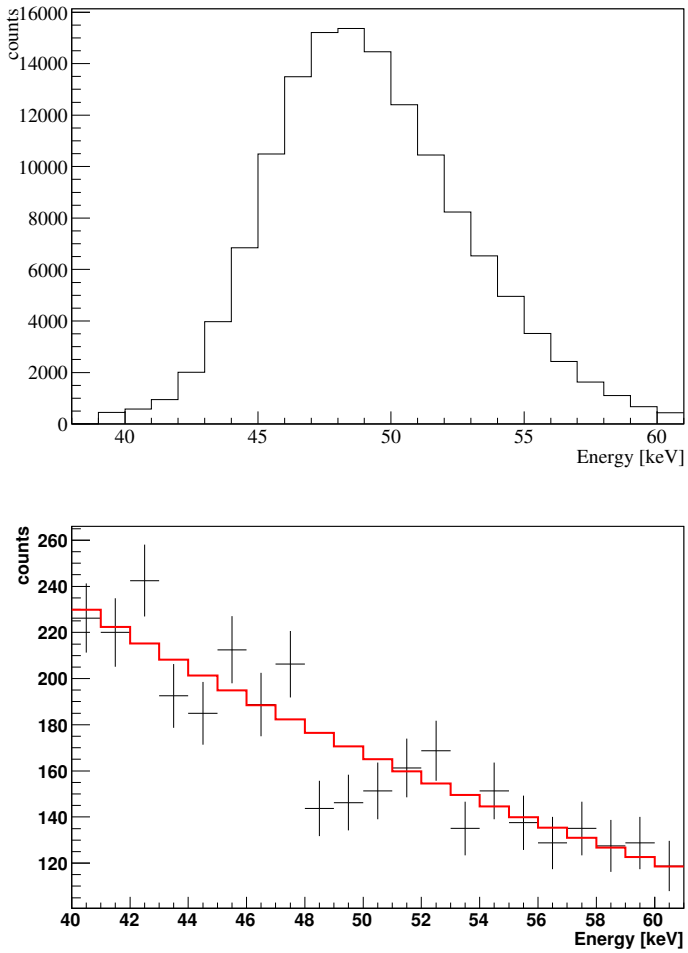

Figure 4.10: Top: Monte Carlo simulation of a ^{210}Pb bulk contamination in CCVR1. Bottom: CCVR1 low energy anti-coincidence spectrum. The energy threshold is set to 40 keV. The red line represents the fit to the spectrum with an exponential background and allowing the presence of a ^{210}Pb bulk contamination with the above shape. No hint of such contamination is found.

contamination	Upper limit 90% C.L.
bulk	3.3E-06
surf. 0.01μm	9.8E-07
surf. 0.1μm	3.8E-08
surf. 0.2μm	2.2E-08
surf. 1μm	9.2E-09
surf. 5μm	5.6E-09
surf 10μm	4.9E-09

Table 4.11: Upper limits on the activity of bulk and surface contamination of ^{210}Pb. Bulk contamination is given in [Bq/kg], surface contaminations are given in [Bq/cm^2].

if the surface contamination is deep enough, the α particle can be absorbed by the crystal, giving rise to the same signature of a bulk event.

The M2sum spectrum in Fig. 4.4 shows the background for energies above the polonium α line due to random coincidences between ^{210}Po and low energy events. On closer inspection (see Fig. 4.11), the peaks originated by the sum of a 5407.5 keV line and a low energy γ line originated from Te metastable isotopes are clearly visible. The energy values of γ lines are listed in Table 4.12.

Te isotope	Energy [keV]	Energy + 5407.5 [keV]
^{127}Te	88.3	5495.8
^{129}Te	105.5	5513
^{125}Te	144.8	5552.3
^{123}Te	247.5	5655
^{121}Te	294	5701.5

Table 4.12: Energy of the gamma lines from Tellurium metastable isotopes and corresponding sum energy when in coincidence with a ^{210}Po event.

Due to the presence of these coincidences, only nuclides with a Q-value lower than 5407.5 keV (see Table 4.13) can be used for surface contamination analysis. ^{218}Po and ^{212}Bi are therefore discarded.

The scatter plot of M2 events is shown in Fig. 4.12, in which the shadowed region contains the events with a total energy E_{TOT}=E_1+E_2 within 4

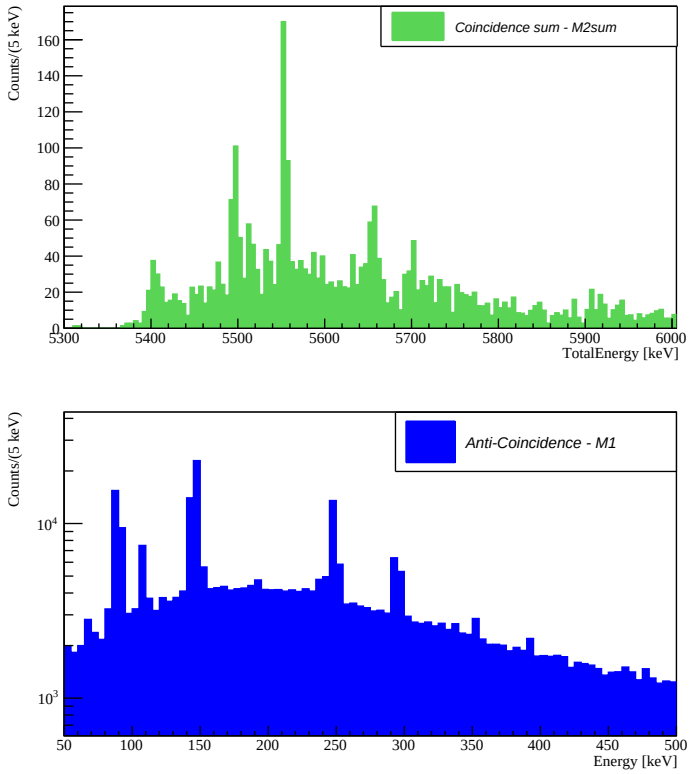

Figure 4.11: Top: M2sum spectrum in the region (5300, 6000) keV. Peaks originating from the accidental coincidence of the 5407.5 keV line and a low energy γ line from Te metastable isotopes are clearly visible. Bottom: M1 spectrum in the region 0-500 keV. The low energy lines from Te metastable isotopes are clearly visible.

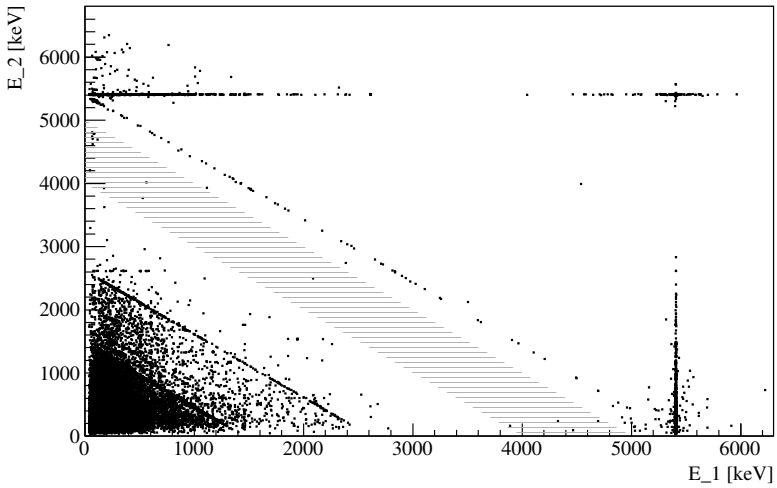

Figure 4.12: Scatter plot of M2 events showing the energy E_1 released in one event versus the energy E_2 released in the second hit. The shadowed region contains events with total energy E_{TOT}=E_1+E_2 between 4 and 5 MeV, used for surface analysis.

and 5 MeV. For each nuclide listed in Table 4.13, the number of counts is computed from the M2sum energy spectrum in an energy window of $\pm$ 6 σ around the Q-value and divided by ε^2 (where ε is the efficiency of the event-based cuts of Table 4.4), since two coincident events have independent probabilities of passing the cuts. In Table 4.13 are shown the corresponding upper limits at 90% C.L., computed using the Bayesian approach with 0 expected background counts and a flat prior for the signal [102].

Monte Carlo spectra for ^{238}U and ^{232}Th contamination on the crystal surface are generated with exponential profile and various penetration lengths. For each contamination depth, the containment efficiency is calculated in a $\pm$ 6 σ interval around the Q-value of each nuclide both for the M2sum spectrum and for the M1 spectrum. The results are shown in Fig. 4.13. For penetration length of 0.01 and 0.1μm the higher containment efficiency comes from the M2sum spectrum, whereas for depths of 1, 5 and 10 μm this originates from the M1 spectrum. The efficiency containment value for 0.2 μm depth is very similar for both the M1 and M2sum spectra. The drop in M1 containment efficiency for very thin layers of contaminations is due to the fact that, of the about 50% of decays where the alpha is emitted toward

Chain	Nuclide	Half-life [y]	Energy range [keV]	N_u 90% C.L.
^{238}U	^{238}U	4.47E+09	4257 - 4283	4.6
	^{234}U	2.45E+05	4845 - 4871	4.6
	^{230}Th	7.54E+04	4757 - 4783	4.6
	^{226}Ra	1599	4857 - 4883	10.5
^{232}Th	^{232}Th	1.4E+10	4069 - 4095	2.3

Table 4.13: Upper limits at 90% C.L. on the number of counts ascribed to several nuclides from uranium and thorium decay chain from the M2sum spectrum. For each nuclide, the half-life of the α decay is also shown.

the bulk of the crystals and the recoil is emitted towards outside, in most of the cases the recoil does not deposit all of its energy in the crystal and so the full Q-value of the alpha decay is not recorded.

The upper limits at 90% C.L. for the surface activity of each nuclide are evaluated using Eq. 4.6 where N_u is the 90% C.L. upper limit on the number of observed events from the M2sum or the M1 spectrum (see Table 4.13 for the M2sum counts and Table 4.9 for the M1 counts) and ε_{MC} is the Monte Carlo average efficiency defined in eq. 4.2 for the corresponding spectrum (M2sum or M1) and for the given signature. The upper limits for surface activity contaminations are calculated for both the M2sum and M1 spectra, normalizing each signature with the corresponding Monte Carlo efficiency. The signature giving the most stringent result is taken into account.

For surface contaminations of 0.01, 0.1 and 0.2 μm depths, the most stringent limits come from the M2sum spectrum. For the remaining depths (1, 5 and 10 μm) the surface activity reduces practically to a bulk activity and the M1 signature produces the most stringent limits.

For the ^{238}U chain, the surface contamination for 2 peaks is evaluated:

- ^{238}U, the chain parent;
- ^{226}Ra, the most active line both in M1 and M2sum spectra.

The contribution from ^{210}Pb is treated separately (see Sec. 4.6).

For the ^{232}Th chain there is only one useable line for this analysis, that is the one from ^{232}Th. This means that there is no way of testing the portion of the chain below ^{220}Rn and take into account a possible non-equilibrium of the chain, as done for the bulk contamination.

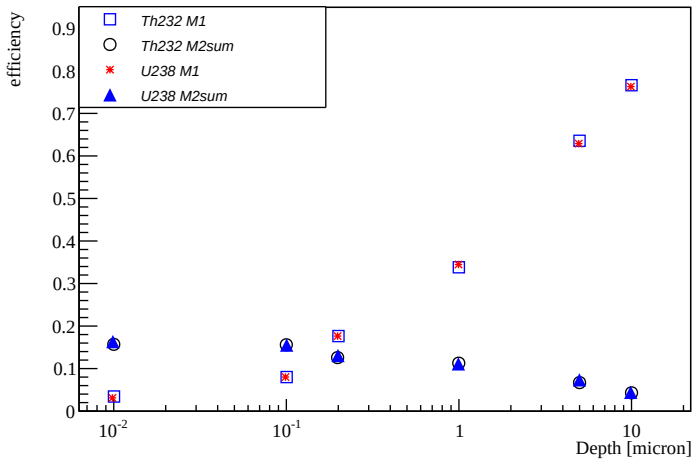

Figure 4.13: For each penetration length, the containment efficiency of surface events is computed for both M1 and M2sum Monte Carlo spectra.

The results for surface contaminations are shown in Table 4.14. As explained in Sec. 4.5.2, the above upper limits are calculated under the conservative hypothesis that the observed counts for each nuclide are entirely due to a surface contamination of that nuclide in the corresponding depth.

4.8 Extrapolation to CUORE background

In order to evaluate the contribution to the CUORE background arising from crystal impurities, a Monte Carlo simulation both for bulk and surface contamination is used, studying their contribution in the double beta decay energy region. The simulation reproduces the geometry of the two detectors (CUORE is a 19 tower array where each tower consists of 13 CCVR-like planes vertically aligned) allowing to account, for example, for the different number of direct neighbors of a CUORE crystal with respect to CCVR (therefore higher efficiency of the anticoincidence cut).

Being interested in a conservative upper limit to the CUORE background, in this extrapolation it has been assumed that CUORE crystals will have the same activity as crystals tested in CCVRs. However, when CUORE will start the data taking, most of the ^{210}Po (and other short lived states) will have decayed and the efficiency for pile-up rejection will be increased.

Depth	Nuclide	Upper limit 90% C.L. [Bq/cm^2]
0.01μm	^{238}U	3.1E-09
	^{226}Ra	6.3E-09
	^{232}Th	1.6E-09
0.1μm	^{238}U	3.2E-09
	^{226}Ra	6.6E-09
	^{232}Th	1.6E-09
0.2μm	^{238}U	3.8E-09
	^{226}Ra	7.6E-09
	^{232}Th	2.0E-09
1μm	^{238}U	3.7E-09
	^{226}Ra	8.9E-09
	^{232}Th	1.9E-09
5μm	^{238}U	2.0E-09
	^{226}Ra	5.4E-09
	^{232}Th	1.0E-09
10μm	^{238}U	1.7E-09
	^{226}Ra	4.4E-09
	^{232}Th	8.3E-10

Table 4.14: Upper limits at 90% C.L. for surface contamination, for different penetration length values. See text for the details on the calculations.

4.8.1 Background from bulk contamination

The CUORE geometrical efficiency for a uniform bulk contamination of crystals in ^{210}Pb, ^{238}U and ^{232}Th is estimated via Monte Carlo, and the corresponding CUORE background at the DBD energy region (Q-value $\pm$ 30 keV) is calculated using the formula:

$$\mathrm{bkg_{CUORE}} = \frac{A_{\mathrm{CCVR-bulk}}\ \varepsilon_{MC}^{\mathrm{CUORE-bulk}}}{\Delta E} \tag{4.7}$$

where $A_{\mathrm{CCVR-bulk}}$ are the values of ^{210}Pb, ^{238}U and ^{232}Th activities from Tables 4.10 and 4.11, $\varepsilon_{MC}^{\mathrm{CUORE-bulk}}$ is evaluated through Monte Carlo simulations and ΔE = 60 keV. The results are shown in Table 4.15.

chain	Nuclide	Upper Limit 90% C.L. [counts/keV/kg/y]
	^{210}Pb	2.6E-05
^{238}U	^{238}U	8.1E-07
	^{234}U	1.4E-06
	^{230}Th	1.7E-06
	^{226}Ra	2.1E-06
	^{218}Po	5.1E-07
^{232}Th	^{232}Th	1.7E-05
	^{212}Bi	1.1E-04

Table 4.15: Extrapolation to CUORE background from CCVRs bulk contamination limits from Tables. 4.10 and 4.11.

In the most conservative approach, considering the most active line (^{212}Bi), the upper limit to the CUORE background at the DBD energy due to bulk contamination of crystals is set to:

$$1.1 \cdot 10^{-4} \mathrm{counts/keV/kg/y}.$$

4.8.2 Background from surface contamination

In a similar way, the CUORE geometrical efficiency for a surface contamination for several depths is estimated. The corresponding CUORE background is extrapolated using the formula:

$$\mathrm{bkg_{CUORE}} = \frac{A_{\mathrm{CCVR-surf}}\ \varepsilon_{MC}^{\mathrm{CUORE-surf}}\ S}{\Delta E\ M_{\mathrm{CUORE}}} \tag{4.8}$$

where $A_{\mathrm{CCVR-surf}}$ are the surface contamination values from Tables 4.11 and 4.14, $\varepsilon_{MC}^{\mathrm{CUORE-surf}}$ is estimated via Monte Carlo simulations, S is the surface of the CUORE crystals, $\Delta\mathrm{E} = 60$ keV and $M_{\mathrm{CUORE}} = 0.75 \cdot 988$ kg.

Depth	Nuclide	Upper limit 90% C.L. [counts/keV/kg/y]
0.01μm	^{210}Pb	4.6E-04
	^{238}U	6.4E-05
	^{226}Ra	1.3E-04
	^{232}Th	2.0E-05
0.1μm	^{210}Pb	1.8E-04
	^{238}U	2.1E-04
	^{226}Ra	4.2E-04
	^{232}Th	7.0E-05
0.2μm	^{210}Pb	2.6E-04
	^{238}U	4.4E-04
	^{226}Ra	8.7E-04
	^{232}Th	1.5E-04
1μm	^{210}Pb	3.7E-04
	^{238}U	1.4E-03
	^{226}Ra	3.3E-03
	^{232}Th	4.7E-04
5μm	^{210}Pb	4.9E-04
	^{238}U	1.1E-03
	^{226}Ra	3.0E-03
	^{232}Th	4.7E-04
10μm	^{210}Pb	2.9E-04
	^{238}U	7.3E-04
	^{226}Ra	1.9E-03
	^{232}Th	3.2E-04

Table 4.16: Extrapolation to CUORE background from CCVRs surface contamination limits from Tables 4.11 and 4.14.

The results are shown in Table 4.16. Accordingly to these results, in the most conservative approach, a crystal surface contamination in CUORE within the limits estimated from CCVRs data, would yield a rate in the DBD energy region lower than $4.2 \cdot 10^{-3}$ counts/keV/kg/y. This value corresponds to the worst case: a contamination in ^{238}U and ^{232}Th at 1μm and a contamination in ^{210}Pb at 5μm. This result is strictly dependent on the density profile assumed for the contaminants distribution, as it can be seen in Fig. 4.14, where the upper limit at the 90% C.L. for the rate in the

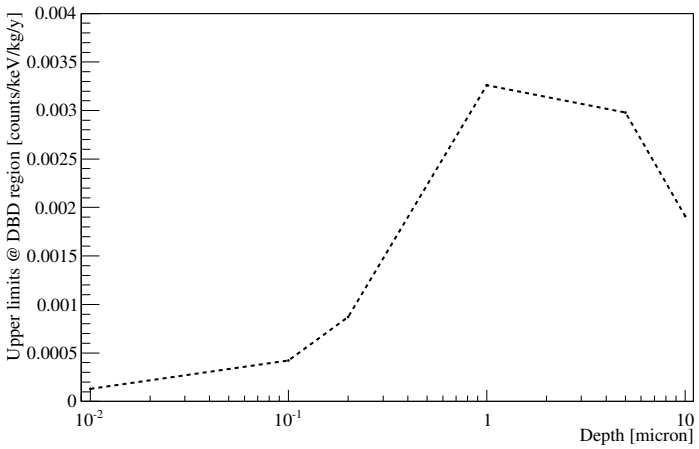

Figure 4.14: For each penetration depth, the upper limits at 90% C.L. for the count rate at the DBD energy region are plotted. The values are computed on ^{226}Ra line, and are due only to surface crystals contaminations.

DBD energy region (computed on ^{226}Ra line) is plotted in function of the contamination depth.

4.9 Performances of CCVR bolometers

Together with the radiopurity of the crystals, the CCVRs measurement are also used for the evaluation of the bolometer performance. It is important to note that it is not simple to compare the performances of different bolometers and, moreover, to identify the reason of eventual differences among the detectors. The main problem is that, even in case of dealing with identical bolometer components, minimal differences in their response are still possible due to the fact that the bolometers have been assembled manually; for example, two NTD with the same parameters and size, coupled to the same crystal, can result in different pulses for the same deposed energy due to a difference in the gluing (bigger or smaller dots, a veil instead of a perfect matrix, etc). The reduction of this kind of uncertainties is the main goal of the new CUORE thermistor-to-absorber assembly line, which will be described in Sect. 5.1.

An easy, but not exhaustive, way to examine the bolometric behavior is to evaluate its energy resolution. The energy resolution of the CCVR

bolometers is calculated from the FWHM of some radioactive lines: 1460 keV from ^{40}K, 2615 keV from ^{208}Tl and 5407 keV from ^{210}Po; the results are collected in Tab. 4.9. Only the energy resolution of the channels used for the background analysis described before are reported. Examples of fit plots (Channel2 - CCVR4) are shown in Fig. 4.15.

The average value of the energy resolution computed on the 2615 keV peak is (4.9±1.8) keV, which represents an improvement in comparison to the CUORICINO value (6.3±2.5) keV. One of the goals of the new CUORE assembly line, that will be described in the next Chapter is to ensure the uniformity and reproducibility of the energy resolution among detectors.

The implementation of a tested automated gluing and assembly line is aimed to produce detectors with all the same performances in terms of resolution. In this way, with a uniform resolution for all CUORE bolometers of 5 keV at 2.6 MeV, one of the minimum requirements for achieving a sensitivity of 10^{26} years on the half life of ^{130}Te 0νDBD will be fulfilled.

Run	channel	FWHM 1460 [keV]	FWHM 2615 [keV]	FWHM 5407 [keV]
CCVR1	1	5.7	4.9	5.3
	3	3.2	3.6	4.1
	5	5.0	4.2	4.5
	6	3.0	3.1	2.9
CCVR2	2	4.9	4.4	4.6
	3	2.8	2.8	2.6
	5	3.1	3.6	3.4
	7	2.2	2.9	2.3
CCVR3	1	4.1	4.2	4.6
	2	3.9	4.0	4.6
	3	4.3	4.2	4.0
	4	6.2	6.1	7
CCVR4	1	7.4	6.9	6.7
	2	6.1	6.0	6.1
	3	5.5	5.3	5.3
	5	9.9	9.4	9.3
CCVR5	2	5.0	4.9	7
	4	3.5	3.6	4.0
	5	9.5	8.7	8.3
	8	4.3	4.4	5.1

Table 4.17: Energy resolution of the CCVR bolometers, evaluated on different peaks.

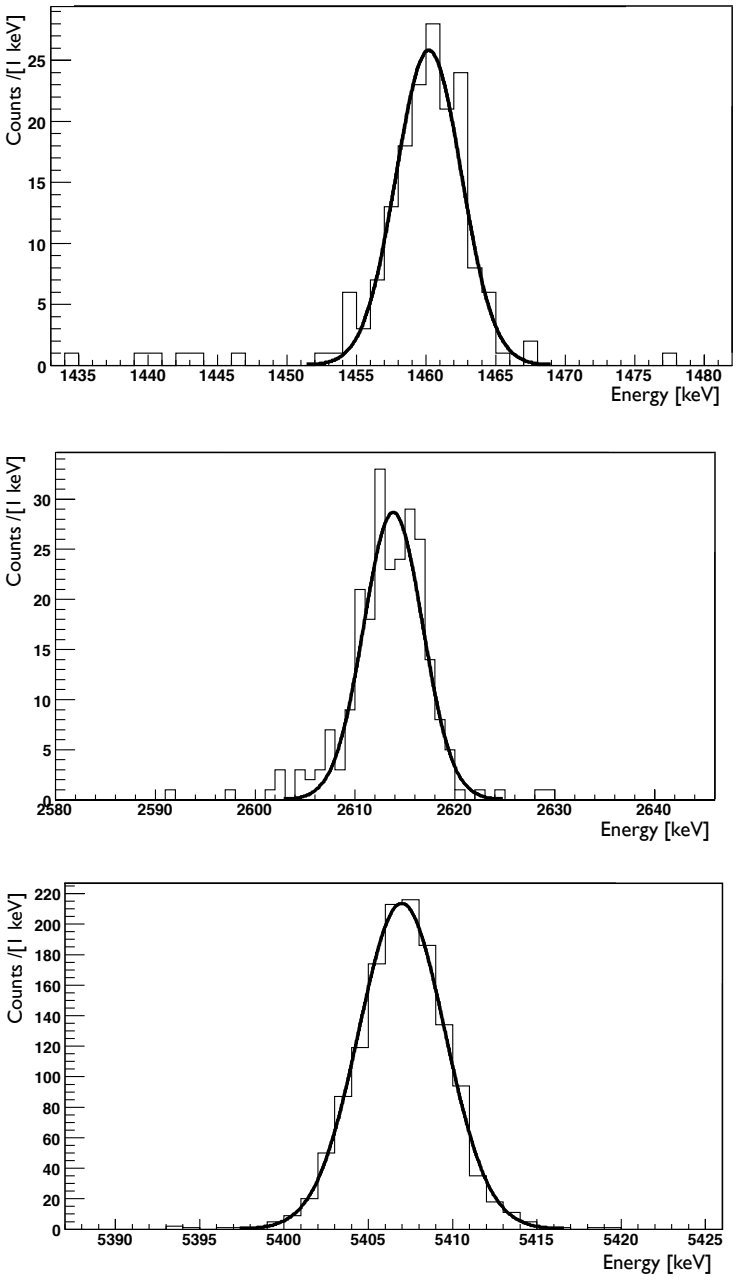

Figure 4.15: Energy resolution of channel 2 in CCVR4. Top: 1460 keV ^{40}K gamma line; Middle: 2615 keV ^{208}Tl gamma line; bottom: 5407 keV ^{210}Po alpha line.

Chapter 5

CUORE-0: the final test for CUORE

The first step of the CUORE experiment will be CUORE-0 , a single CUORE-like tower that will operate in the former CUORICINO cryostat and will start acquiring data in spring 2012.

CUORE-0 will consist of 52 CUORE crystals mounted with CUORE-style frames in a single tower with a total TeO_2 mass of 39 kg. It will be assembled with detector components manufactured, cleaned, and stored following the same stringent protocols defined for CUORE ; its construction will also be performed following the no-contact procedures developed for CUORE detector assembly. The preparation of CUORE-0 is thus aimed to confirm the efficacy and feasibility of the CUORE production and assembly procedures. In addition, CUORE-0 represents an opportunity to evaluate the bolometric performance of a CUORE -like detector apparatus in a familiar cryostat, and it will be the first large-scale empirical test of the undertaken extensive background-reduction measures.

This Chapter will describe the preparation activities before the construction of the CUORE-0 tower using the new CUORE assembly line. The attention will be focused on the CUORE-0 wiring read out, being related to part of this PhD activity.

5.1 The CUORE Tower Assembly Line (CTAL)

The assembly of the CUORE towers must be conducted following very strict prescriptions, due to the extraordinary level of radio-purity necessary for the success of the 0νDBD experiment.

The assembly is done following a "zero contact" philosophy for the detector components, i.e. no exposure to air to prevent possible Radon contamination and minimized contact (in space and time) with other materials. For these reasons, the whole assembly procedure will be performed inside dedicated glove boxes, in a clean room recently built in the CUORE hut in the Hall A of LNGS. Moreover, to reduce the cosmogenic activation, the exposure of detector parts to cosmic rays has to be minimized. The detectors parts, after having been produced, are packed and then stored in the so called Parts Storage Area (PSA), situated in the underground Laboratories, inside stainless-steel cabinets, which are flushed continuously with Nitrogen until the time when they will be used for the CUORE construction.

The tower construction is conduced around two units: the gluing station, which provide all the tools needed to glue the chips on the crystals, and the assembly line, an integrated set of tools devoted to the final assembly of the tower. Both units use glove boxes to provide a controlled atmosphere environment. Each glove box has been specifically designed in order to meet the requirements of each single operation.

5.1.1 The gluing glove box

As already mentioned in 3.3.2, the coupling of the sensors (thermistors and heaters) to the TeO_2 crystal absorbers has a relevant role in defining the performance of the detector. The quality of the glue spots (number of spots, volumes of the drops, height, diameter, pitch, air bubble inclusion, etc.) is one of the most delicate aspects of the bolometer assembly with respect to its integrity after the cool down and with respect to the bolometer response itself. A big effort has been done in order to improve the totally manual gluing procedure used previously in CUORICINO and obtain a highly reproducible sensor-to-absorber coupling procedure.

The sensor-to-absorber coupling is made applying a matrix of glue dots. In fact, in comparison with a veil deposition, the distribution in separate spots compensates the differential thermal contractions between the material of each sensor and TeO_2 , so that no fractures or detachments of the elements occur at low temperatures. The most efficient results are obtained with nine dots for a $\sim$3x3 mm^2 thermistor and with five dots for a $\sim$2.4x2.4 mm^2 heater (see Fig. 5.1). The dots diameter is chosen as $\sim 700 \mu$m while their height is determined by imposing a 50 μm gap between the TeO_2 crystals and the chips.

The glue used for that purpose must have a density high enough to avoid the merging of the dots after their deposition and of course it has to work

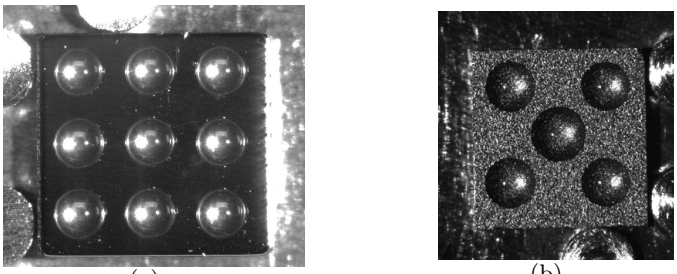

(a) (b)

Figure 5.1: Examples of gluing obtained with the new chip-to-absorber coupling line. (a): nine-dot matrix on a thermistor; (b): five-dot matrix on heater.

at cryogenics temperatures. The chosen one is the Araldite Rapid glue, a bi-component epoxy with an extremely short pot-life (3 minutes), whose radioactive contaminations showed to be very low, in agreement with the CUORE requirements.

The new automatic gluing system for CUORE-0 and CUORE detectors is performed in a glove-box, in a nitrogen gas atmosphere. The main tools of the gluing line are the XYZ positioner (for precise chip positioning), the glue dispenser and the anthropomorphic robot. The anthropomorphic robotic arm moves the crystals and the chips inside the glove box, eliminating the operator contact with cleaned detector elements and allowing high positioning repeatability. One of the main problems of the automatic sensor-to-absorber coupling is the fast curing time of the glue that prevents from using standard dispensing solutions and forces to a deep customization of the instrumentation. The glue is also extremely sensitive to change in the environmental temperature and pressure: for this reason a careful work for setting up correctly all the components in the right configuration was required during the installation of the gluing line in the underground CUORE clean room. The gluing line, after a careful cleaning of all its parts (mainly in PTFE and steel), was placed in the underground CUORE clean-room in spring 2011. The commissioning of the entire system was successfully completed in summer 2011. The gluing line then produced the 52 bolometers for the CUORE-0 tower. In Fig. 5.3 are shown four crystals that will be used for the CUORE-0 construction.

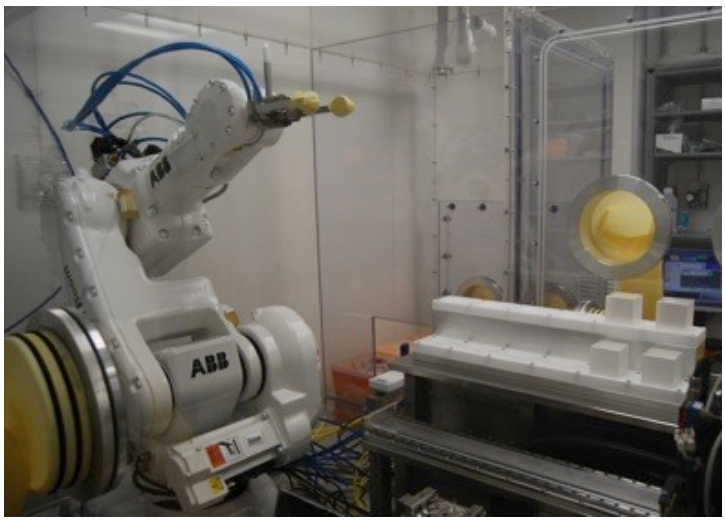

Figure 5.2: A picture of the operating CUORE gluing line: the ABB anthropomorphic robot (left) and the crystal repository with a TeO_2 crystals (right).

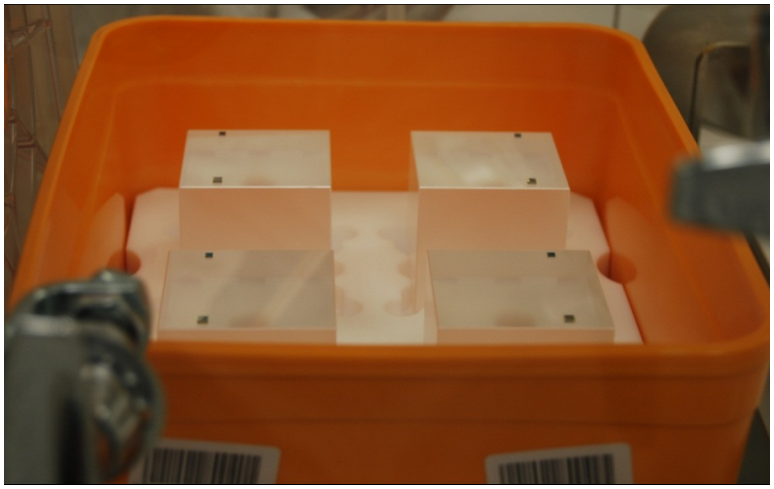

Figure 5.3: Four CUORE-0 crystals assembled using the new gluing line: on each crystal are visible the two sensors, NTD and heater.

5.1.2 The assembly glove boxes

The assembly line is arranged around a common airtight box, named Garage, which is used to handle and safely store the tower during all the assembly steps, and around some dedicated working volumes, the Glove Boxes (GBs). A dedicated clean mock-up tower has been used during the commissioning of the assembly line to validate all the operations performed in the GB. At the interface between the Garage and the Glove Boxes, is the "Universal Working Plane" (UWP), an aluminum table which is sealing the Garage top and which is supporting the single GBs (see Fig. 5.4(a)). The Garage and the GBs are continuously flushed with N_2 during all the real assembly operations.

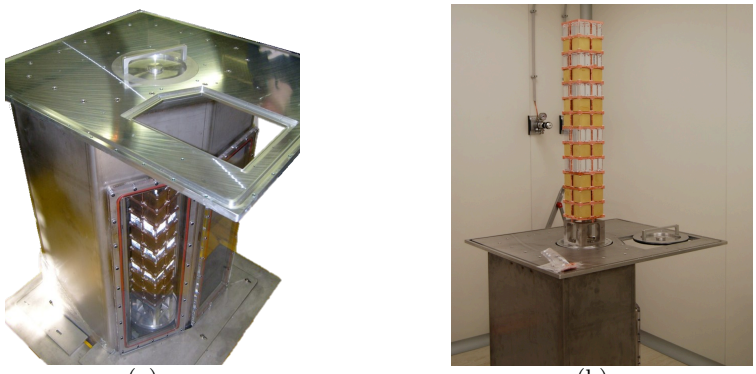

(a) (b)

Figure 5.4: (a): the mock-up tower closed in the Garage, with at the top the UWP; (b): the mock-up tower lifted from the Garage thanks to the elevator.

The tower is built on top of an assembly plate (see Fig. 5.4(b)), part of the garage equipment, which can rotate or move up and down through an elevator with a rotating base, driven by a remote control. Speed and precision of the motion allow the operator to place the tower in the different positions required for the assembly actions that have to carried out. By using the vertical motion, the tower can be safely stored and sealed inside the garage at any time, for example during standard procedures like the exchange of a glove box, or whenever the assembly must be interrupted for any reason (see Fig. 5.4(a)). The first GB coupled to the UWP is the Mechanical GB (Figures 5.5(a) and 5.5(b)) that will be used to mechanically assemble the structure of a single CUORE tower. This GB consists of two airtight volumes communicating through a sealable door. The "antecham-

ber" is the area where the single components (crystals, teflon holders, copper frames and columns) are extracted from the storage vacuum boxes and enter into the assembly chamber through dedicated PTFE slides where they are assembled all together. The assembly chamber is also equipped with two microscope used for real time check of the geometrical and dimensional accuracy of the tower under construction. Fig. 5.6 shows the operation of the microscopes, during the CUORE-0 test.

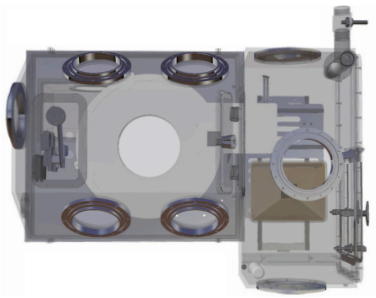

(a)

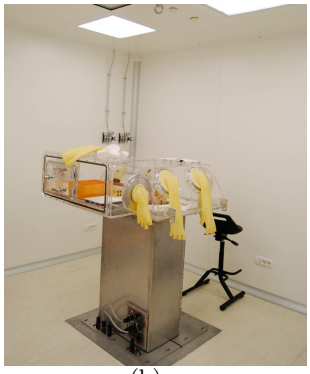

(b)

Figure 5.5: (a): schematic drawing of the Mechanical Glove Box (Mech Box), top view; (b): The Mech Box mounted on the Garage.

As soon as the tower structure is completed, the Mechanical GB is removed and substituted by the Cabling GB that allows the placement of the wire trays on the tower. The next step is the bonding of the thermistors and of the heaters to the pad of the wire trays. This task is accomplished inside the Bonding GB in which a commercial bonding machine has been customized for work in vertical position. Here many of the movements normally done manually by the operator are now driven by step motors, remotely controlled. Bonding very small Cu pads with 25μm gold wires, with the tower and the machine arranged in a vertical position inside a glove box, represents an extremely difficult task. Nevertheless, the bonding test performed on the pads of the wire trays coupled to the mock tower has given satisfctory results during the commissioning of the assembly line. More details will be given in Sect. 5.2.

Once the bonding is completed, the Cabling GB is used again to mount the covers of the wire trays and the shields (see Fig. 5.7(a)). This operation completes the construction of the tower, which is then put in a nitrogen flushed Storage Box (see Fig. 5.7(b)).

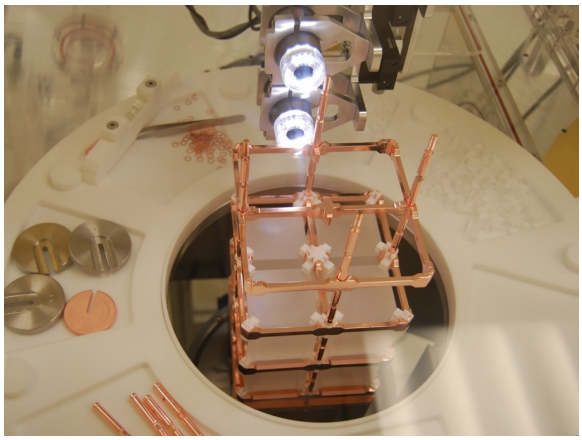

Figure 5.6: Detail of the microscopes operations in the main chamber of the Mechanical GB during the CUORE-0 test.

(a) (b)

Figure 5.7: (a): A picture of the Cabling glove box installed in the CUORE Clean Room. The CUORE-0 radiation shields are also assembled. (b): the mockup tower inside the Storage Box.

In parallel to this system runs an independent, stand alone, glove box called the "End Of the World" (EOW), see Fig. 5.8(a) and 5.8(b). It is used to prepare, just in time, the components for the main assembly system. The EOW glove box is the only part of the assembly line not coupled with the garage. It has been designed to accomplish all those tasks that are not so

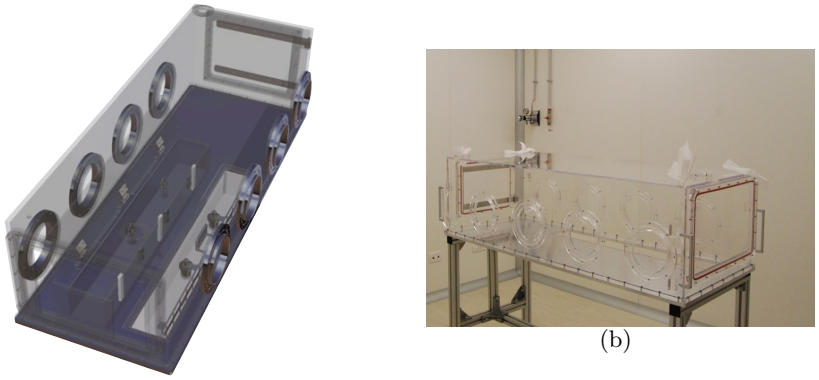

(a) (b)

Figure 5.8: (a): schematic drawing of the "End of the World" glove box (EOW). (b): The EOW during the commissioning in the CUORE clean room.

complex to justify an ad hoc solution, but that also do not fit in any of the specialized GBs. As an example, it will be used to re-packaging the detector components before they enter in the Mechanical Box, to assemble the wire trays or the CUORE-0 shield holders, etc. In Fig. 5.9 is shown the coupling of the wire tapes to the wire trays performed during the commissioning of the assembly line.

5.2 CUORE-0 wiring readout

As described in Sect. 3.3.2, each of the 52 crystals of a tower is equipped with a thermistor and an heater. The read out of these signals is realized through the Flexible Flat Cable (FFC) special tape approach, with gold ball bonding performed in situ from the chips to Copper tapes.

The CUORE-0 read out system consists of a set of 1.4 m long, $\sim$80μm thick, Cu-insulator tapes having PEN (Polyethylene 2.6 Naphthalate) substrate, on which a pattern of copper tracks are etched. The layer of Copper track is $\sim$17μm thick. For CUORE the cables will be $\sim$2.3m long, due the larger geometry of the detector.

The Cu-PEN tapes have been carefully designed in order to satisfy different specifications: low background, negligible cross-talk, negligible microphonism, very large parasitic impedance and high level of packaging. Each tower is equipped with two packs of nine wire tapes each. Three tapes are used to connect the 26 thermistors, another tape is used to connect the

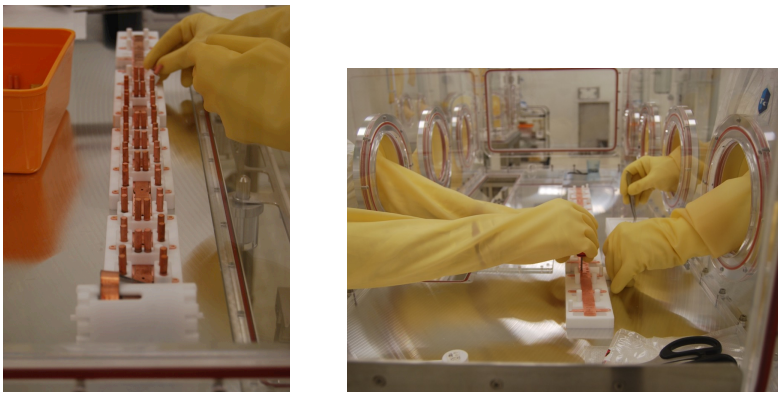

Figure 5.9: The operation of coupling of the wire tapes to the wire trays during the commissioning of the assembly line.

heaters of the same 26 crystals. The tapes are packed together, putting one on top of the other. Between any pair of the four tapes for the electrical signals, a grounded tape is inserted for electrical shielding, therefore totaling 9 tapes for each packs. For each tower the two packs are positioned and glued to a wire tray, which is running all along the tower, in a way that the pads, on which it will be performed the bonding from the chips, will be positioned at each floor of the tower. In Fig. 5.10 are shown the different tape shapes: T1 which reads the signals of thermistors from floor one to five (the counting starts at the top of the tower), T2 for signals from floor six to nine, T3 for signals from floor ten to thirteen. Being the heaters of one column all connected in parallel, only one tape for pack is needed (tape "Pulser" in Fig. 5.10). Fig. 5.11(a) shows a detail of the pads where the thermistors or the heaters will be bonded (these pads have the same features whether they are thermistors or heater pads).

The CUORE-0 and CUORE bolometers are read by differential voltage amplifiers. The link layout is designed to reduce as much as possible the distance between the two tracks of every differential pair, so that any mechanical vibration generates equal effects (common mode) on both elements of the pair. Therefore, at the amplifier input, the disturbances will cancel out. The Cu-PEN was designed to consider all these specifications. The width of every Copper track is 0.2 mm and the pitch 0.4 mm. The final width of the ribbon is 13.4 mm, with 1 mm of margin on each side. Being the CUORE-0 cables are 1.4 m long, while the standard production masks for track serigraphy have an extension of 80 cm maximum, the 2 masks

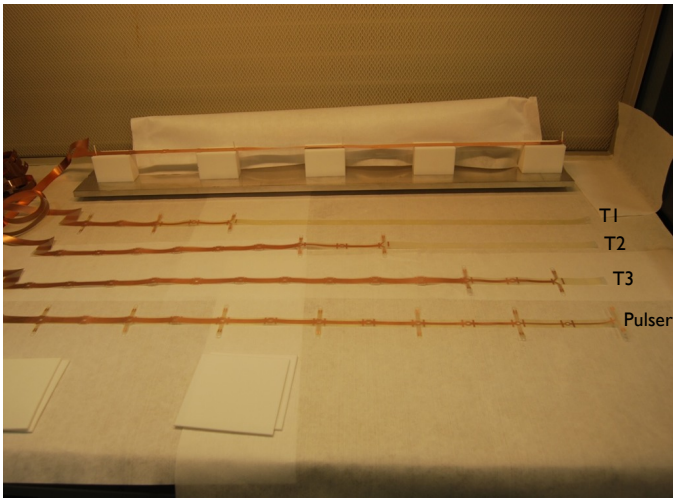

Figure 5.10: Different types of CUORE-0 PEN-Cu tapes. The picture shows ∼80 cm of the tapes that will be all along the tower.

must be manually jointed. To avoid any possible failure, at the joints the Cu-PEN was shaped wider on purpose and the tracks are larger (0.4 mm) and well separated (0.8 mm the pitch). An example of this feature is shown in Fig. 5.11(b).

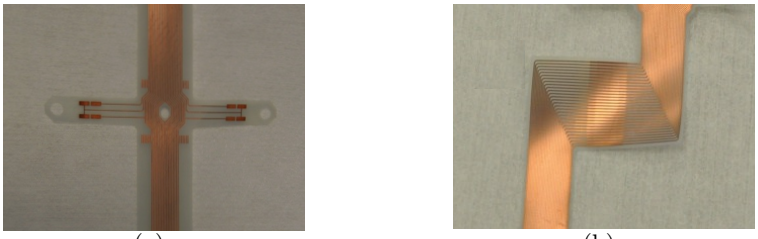

(a) (b)

Figure 5.11: (a): detail of the tape, showing the arm where the thermistors or the heathers will be bonded; (b) tape shape at the joints between production masks.

5.2.1 Tapes radioactivity

The radioactivity of all the materials located near the crystals has to be evaluated. Surface Barrier Detectors (SBD) were used to perform α spectroscopy and to investigate the presence of contaminations from the ^{238}U and ^{232}Th decay chains in the PEN-Cu tape. A few samples were checked using Silicon detectors at the Physics Department of the Milano Bicocca University. No excess of the counting rate in the α energy region was observed compared to the intrinsic background of the detector. Monte Carlo simulations were also performed for taking into account of the detection efficiency, and upper limits on the surface contaminations were set. The results are shown in Tab.5.1. The table shows the upper limits, measured in [Bq/cm^2], on the surface contaminations in ^{238}U and ^{232}Th that would originate from a contamination located uniformly at the corresponding depth. These values, extrapolated via Monte Carlo simulations to the geometry of the CUORE experiment, would result in a background lower than 10^{-3} counts/keV/kg/y .

Chain	0.1[μm]	1[μm]	5[μm]	10[μm]
^{238}U	$4.29{\cdot}10^{-7}$	$4.29{\cdot}10^{-7}$	$1.78{\cdot}10^{-6}$	$2.02{\cdot}10^{-6}$
^{232}Th	$5.36{\cdot}10^{-7}$	$4.31{\cdot}10^{-7}$	$4.41{\cdot}10^{-7}$	$5.36{\cdot}10^{-7}$

Table 5.1: Upper limits measured in [Bq/cm^2] on the surface contamination of PEN-Cu tapes measured with SBD detectors.

5.2.2 PEN-Cu electrical properties

The electrical properties of CUORE-0 tapes have been accurately characterized for what concern insulation and continuity.

The impedance characterization consisted in the measurement of the resistance between the tracks. The static impedance is a very important parameter since it can add DC offset and parallel noise. The characterization was made in vacuum condition: a dedicated box was designed in order to measure the 1.4 m long tapes without damaging the 17μm copper layer. The 4 tapes of a single pack (T1, T2, T3 and Pulser) were first arranged on PTFE holders and then connected to the electronic boards and enclosed by means of a plexiglas cover. The experimental set-up is shown in Fig. 5.12. A vacuum level of $\sim$0.03 bar was achieved by means of a diaphragm pump and the impedances of tracks was measured with a Keithley 6514 Electrometer. The performances of all the tapes were satisfactory: with the above mentioned

operating conditions, after a few hours, the parasitic impedance was larger than the instrumental full-scale limit of 200 GΩ, as shown in Fig. 5.13.

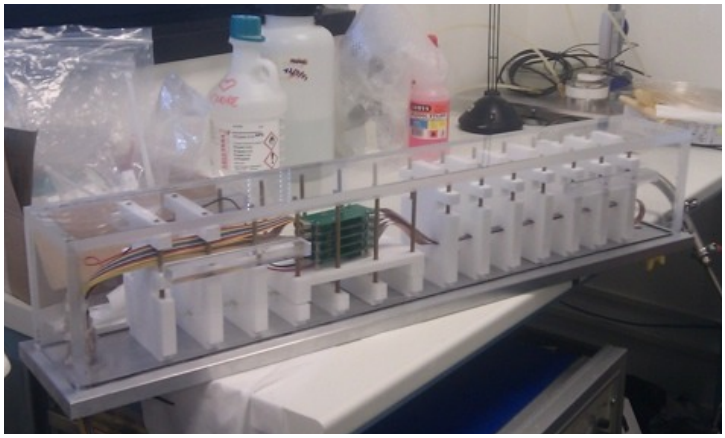

Figure 5.12: A picture of the experimental setup realized for the measure of the impedance of the CUORE-0 PEN-Cu tapes.

Also the electrical continuity of the CUORE-0 tapes was checked, using the Time Domain Reflectometry (TDR) technique [103]. The measurement can be performed connecting each pair of adjacent tracks to a fast sampling oscilloscope (DCA-X 86100D, 18 GHz Bandwidth). Sending a differential voltage step (20 ps edge) along a pair of track and, measuring the reflected signals it is possible to obtain informations on the properties of tracks. The "differential TDR" (the difference between the reflected signals) gives global information on the characteristics of the tracks, while the "common mode TDR" (the sum of the reflected signals) can also reveal possible asymmetries between the 2 tracks, including possible problems i.e. broken tracks or shorts. This technique enables to study the continuity of the tapes even if the track are left open at the end. Moreover, since the arms of the tapes are untouched, there is no risk of damaging the bonding pads. In Fig. 5.14 it is shown the plot of the signal amplitude versus the time of reflection of a good pair of tracks: the differential TDR is the yellow curve, while the common mode is the green one. Both signals are measured in mV (the calibration of the oscilloscope is 100 mV/div) and an offset of 200 mV on the vertical direction prevents the green curve to be set at the "zero" of the Y-axis. The yellow curve shows the shape for the signal reflection of a good pair of tracks, while the "common mode TDR" curve is close to zero, as

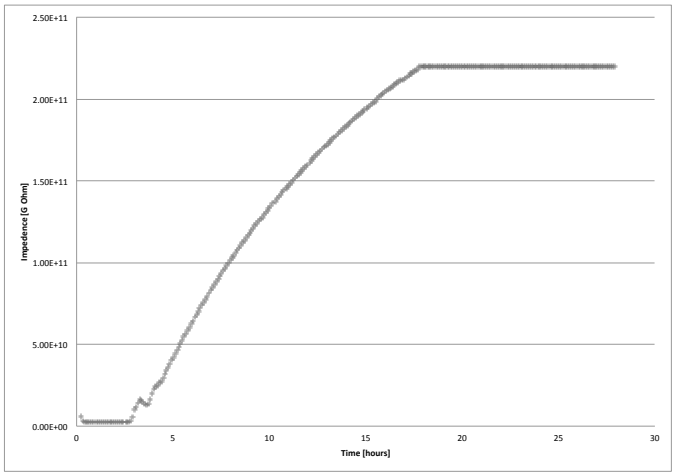

Figure 5.13: Plot of the parasitic resistance between adjacent tracks of the PEN-Cu tapes. After few hours, it reaches a value larger than the instrumental full-scale limit of 200 GΩ.

proof of the good quality of both tracks. Fig. 5.15 shows instead the plot for a broken track: it is clear from the shape of the "common mode TDR" curve, which drifts away from the null value, that there is a problem in the observed tracks. With a closer inspection of the tape with a microscope, it was easy to find an interruption in the copper track (see Fig 5.16). The TDR technique resulted to be an excellent tool for the diagnostic of the quality of the tapes, allowing to discover defects in the tracks that would not have been noticed with a simple visual inspection.

5.2.3 Bonding on Copper pads

One of the most difficult aspects of the CUORE-0 and CUORE assembly line are the bonding operations of the thermistors and of the heaters to the pads of the PEN-Cu tapes. Due the radioactivity constraints on the materials, it was not possible to realize on the PEN-Cu tape side more standard golden pads because the gold deposition techniques resulted to be radioactive. Moreover, R&D bonding test revealed that an oxidized copper surface prevents the bonding of the gold wire on the pads. For this reason, many test have been performed to finalize the protocol for the preparation of the tapes in order to have a de-oxidized copper pad surface. The procedure

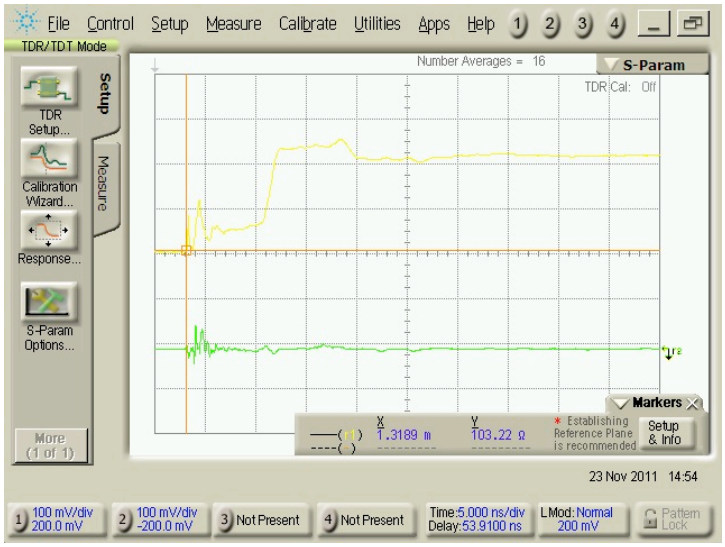

Figure 5.14: Signal of "differential TDR" (yellow) and "common mode TDR" (green). On the Y-axis is shown the signal amplitude (100 mV/div) and on the X-axis the reflection time (5 ns/div). The common mode curve is close to zero, indication of the good quality of the tracks.

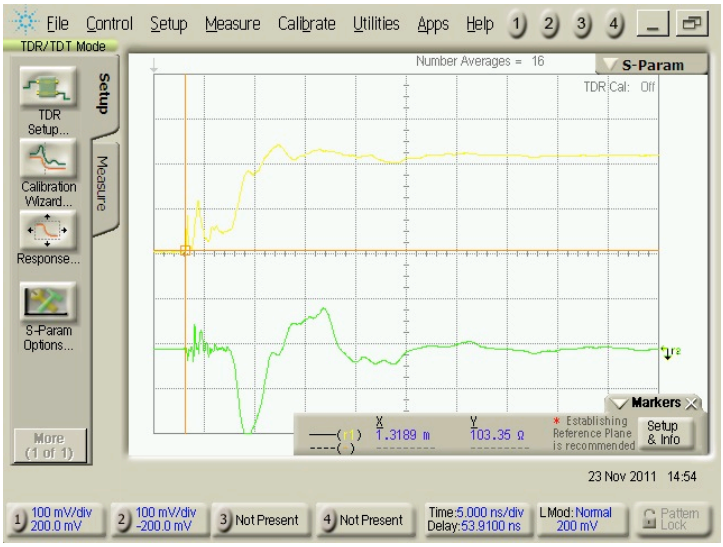

Figure 5.15: Signal of "differential TDR" (yellow) and "common mode TDR" (green). On the Y-axis is shown the signal amplitude (100 mV/div) and on the X-axis the reflection time (5 ns/div). The common mode curve drifts away from zero, clear indication of a problem in the track.

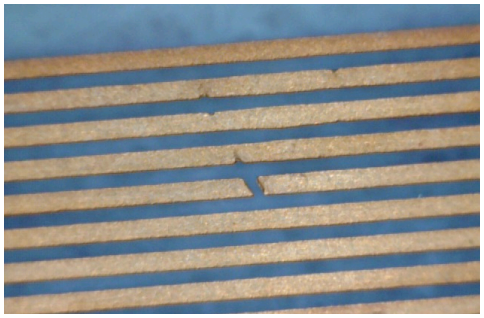

Figure 5.16: Example of a broken copper track.

has been studied following the constraint due to the non-standard features of the item: a thin layer of copper (only 17μm) arranged in 1.4 m long tapes.

In order to remove the oxidized layer that unavoidably grows on the copper pads two kind of reagents were take into account: nitric acid (HNO_3)and citric acid ($C_6H_8O_7$). If nitric acid, on one side, has better properties in etching the surface, on the other hand it could be too aggressive for the thin copper layer of the PEN-Cu tapes. Moreover, if the removal of this acid from the surface would be not perfect, the even small residual traces could potentially produce a long term corrosion of the track. For this reason citric acid was chosen, having good properties in etching the copper surface without being as aggressive as the nitric acid.

Several tests were performed in order to establish the best parameters for the treatment of the pad surface. The dependence of the copper surface erosion rate as a function of citric acid concentration, temperature and time was studied. The final procedure foresees a treatment with a 5% solution of citric acid, at a temperature of 60°C, for 1 hour. In this way a layer of $\sim$0.01μm is removed from the tapes and the consequent bonding tests performed on these samples result satisfactory (Fig. 5.2.3).

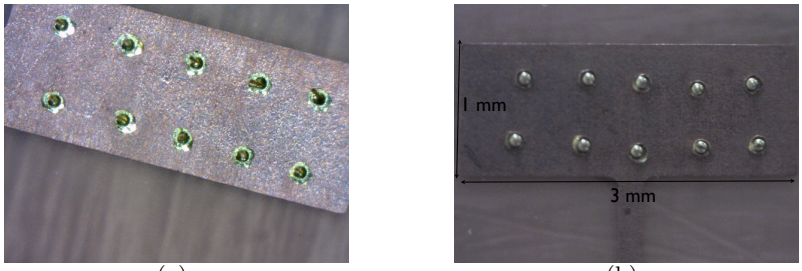

(a) (b)

Figure 5.17: Examples of good bonding on pads: the gold ball are well bonded to the copper surface.

After the good results on the sample, the same operations were also performed on the entire tapes which will be used in CUORE-0 . Only the surface of the pads shall be affected by the treatment, consequently only the 80 cm of the tape looking onto the tower have to be handled. A dedicated system was set-up: Fig. 5.19(a) shows the box containing tapes and citric acid solution, and the heater necessary to keep the temperature at a constant value, to ensure an uniform treatment of the tapes surfaces. After the acid treatment, several rinses with ultra-pure water are required in order to completely remove any residual of the solution. The tapes are then

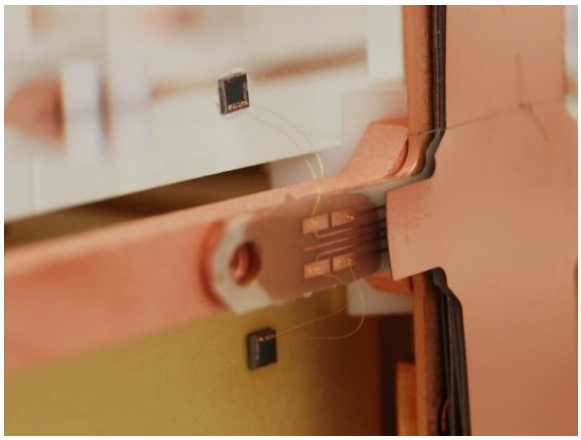

Figure 5.18: Result of a bonding test operated on the mock up tower during the commissioning of the assembly line. In the picture are visible the gold wires connecting the sensors, glued on fake crystals, and the copper pads.

dried with a nitrogen flux, to prevent further oxidation of the surface. This procedure was successfully optimized and tested during the commissioning of the CUORE Tower Assembly Line. To totally exploit the copper surface treatment, these operations have to be performed few days before the start of the bonding operations. A dedicated set of tool were designed and realized in order to prepare and handle the packs of tapes needed for the entire tower. All the operation were performed under a laminar flow cabinet, in order to prevent re-contamination of surfaces. Dedicated clean PTFE spool have also been realized in order to roll up and handle the 1.4m long tapes. Fig. 5.19(b) shows the final PTFE spool housing the tapes pack, ready to be attached to the wire trays.

5.3 CUORE-0 sensitivity

Although the exact background rate that will be seen in CUORE-0 will not be known until the taking data will begin, based on simple scaling arguments, CUORE-0 can be considered a sensitive 0νDBD experiment Even if in the CUORE-0 tower the total amount of copper facing the crystals will be only slightly reduced with respect to CUORICINO , its surface will be treated with the new procedure studied for CUORE , aiming to a reduction at least of a factor 2 of the background in the 0νDBD region of

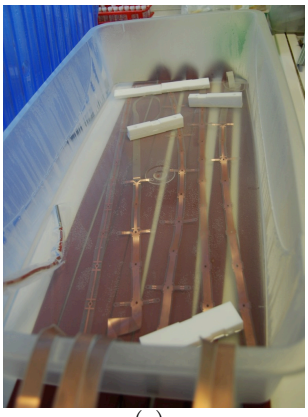

(a)

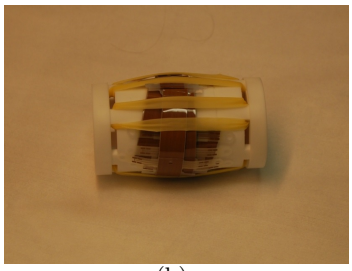

(b)

Figure 5.19: (a): detail of the operation of treatment of the PEN-Cu tapes with citric acid; (b): PTFE spool housing the CUORE-0 tapes pack.

interest. CUORE-0 will be operated in the CUORICINO cryostat and consequently the gamma background from contamination in the cryostat shields will remain approximately the same as in CUORICINO . Considering that the irreducible background for CUORE-0 comes from the 2615 keV ^{208}Tl line due to ^{232}Th contaminations in the cryostat, in the case that all other background sources (i.e. surface contaminations) will be rendered negligible, this would imply a lower limit of $\sim$0.05 counts/keV/kg/y on the expected background. Similarly, an upper limit of 0.11 counts/keV/kg/y follows from scaling the CUORICINO background in the conservative case of a factor of 2 improvement in crystal and copper contamination.

A plot of the expected 1σ sensitivity (comparable to a 68% C.L. sensitivity) of CUORE-0 as a function of live time in these two bounding cases is shown in Fig. 5.20. The anticipated total live time of CUORE-0 is approximately two years; the 1σ sensitivity for this live time is between $6.6{\cdot}10^{24}$ y (at the 0.11 counts/keV/kg/y background level) and $9.4{\cdot}10^{24}$ y (at the 0.05 counts/keV/kg/y background level).

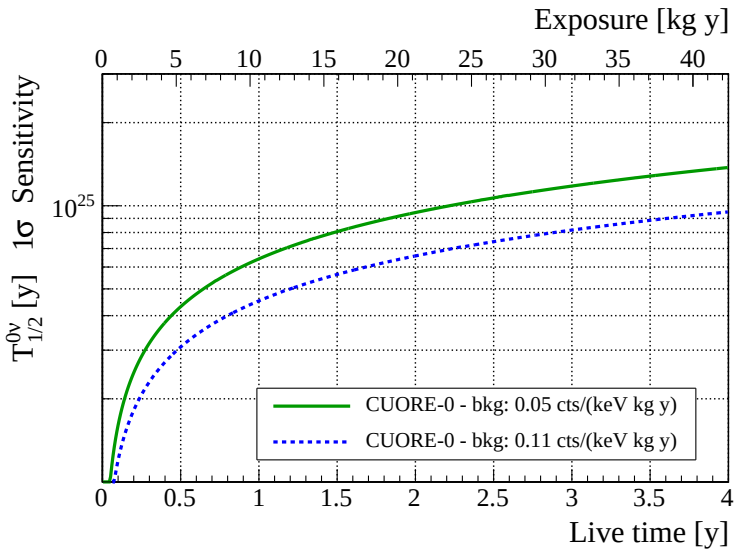

Figure 5.20: CUORE-0 sensitivity at 1σ for two different values of the background rate in the region of interest, 0.05 counts/keV/kg/y (solid green line) and 0.11 counts/keV/kg/y (dotted blue line), representing the range into which the CUORE-0 background is expected to fall.

Chapter 6

The CUORE suspension

The highly demanding technical specifications of the CUORE experiment make its cryogenic system a challenge in the field of large mass cooling. The large detector mass, the low working temperature and the low background level result in very stringent requirements for the construction of the whole cryogenic system. Moreover, the detector has to be mechanically decoupled from the outside, to minimize the noise due to the propagation of external vibrations to the crystals which would spoil the bolometers energy resolution. The suspension system must be realized paying extreme attention to the mechanical, thermal and radiopurity properties of the material components.

In this Chapter the features of the detector suspension designed for CUORE will be described, including the characterization of materials and the characterization of the suspension system through vibration measurement campaigns.

6.1 The detector suspension: an overview

The CUORE detector suspension is a two-stages low frequency isolation system, designed to minimize the transmission to the bolometers of mechanical vibrations due to seismic noise and to the operation of cryocoolers and pumps.

The crystal vibrations must be avoided because they generate energy dissipation changing the detector temperature. Having these temperature instabilities have a frequency spectrum similar to the one of the signal, they are a very dangerous source of noise.

The detector suspension must thus provide load path for the detector while minimizing the heat input and the vibration transmission.

The detector support layout is shown in Fig. 6.1. It includes the concrete foundation, installed on the top of a series of elastomers isolators, the column supports for the detector and the main support plate (MSP), which rests on the top of the columns.

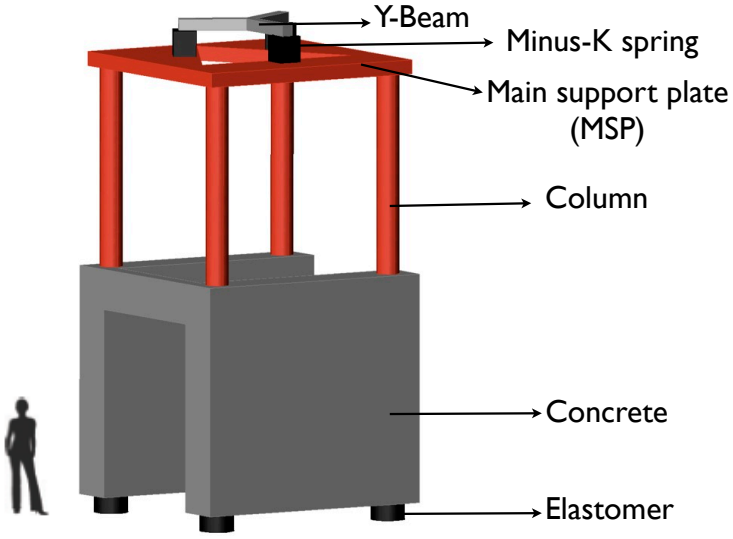

Figure 6.1: Sketch of the detector support layout: the concrete foundation is installed on the top of four elastomers. Above the concrete there are the column supports and the main support plate (MSP). On the MPS are placed the three Minus-k spring and the "Y-beam". The detector suspension will be hung from the "Y-beam".

The first section of the suspension operates at room temperature and consists of three Minus-K springs, placed on the MSP. In a Minus-K spring the vertical motion isolation is provided by a stiff spring that supports the weight load (the Y-beam mass and the detector mass), combined with a negative-stiffness mechanism. The net vertical stiffness is made very low without affecting the static load-supporting capability of the spring. Beam-columns connected in series with the vertical-motion isolator provide also horizontal motion isolation. The net result is a compact passive isolator capable of very low vertical and horizontal natural frequencies and very high internal structural frequencies. The commercial soft Minus-K Springs system used in CUORE implements a position feedback device and it is damped

to avoid high mechanical Q effects [104]. It is tuned to have fundamental resonance frequencies around 0.5 Hz for all degrees of freedom.

The second section of the suspension is directly connected to the Y-beam. This is a cryogenic suspension system, made out of three composite cables, which support the whole detector mass, bypassing the different cryogenic shields (see Fig. 6.2). The system is passive, with no damping, and has been designed according to the requirements imposed from mechanics, cryogenics and radioactivity. The suspension system has to meet at the same time high tensile properties (it holds the detector mass of $\sim$1.2 ton), low thermal conductivity (the detector has to operate at T$\sim$10mK) and low radioactive contamination, being close to the crystals. To satisfy all these constraint, the cable are built using three different materials: stainless steel tie bars, Kevlar 49 ropes and copper bars. The composite rods are made in the upper part of several AISI 316 LN stainless steel rods, with three copper thermal links connecting to 40K, 4K and 600mK flanges. After the 600mK thermal link it is placed a Kevlar rope section, which strongly reduces the thermal conductivity of the suspension. In addition, since the Kevlar rope is not rigid, it helps to damp the vibrations along the suspension. The last segment of the suspension is a high-purity copper rod, completely below the mixing chamber, which ensures the radiation purity required in close proximity to the detector. Soft mechanical contacts have been selected to implement the thermalizations in order to limit heat loads.

For the inner top lead shield it is foreseen a similar suspension scheme: the lead suspension is hung from the 300K flange and not to the Y-beam to guarantee the best mechanical decoupling of the detector from the cryostat assembly.

The detector suspension has been pre-assembled in the CUORE hut and an extensive campaign of vibration transmission measurements has been performed. Moreover, the Kevlar section of the suspension has been carefully investigated for what concerns the Kevlar properties at low temperature. These topics will be presented in detail in the next sections.

6.2 Characterization of the detector suspension

The characterization of the detector suspension started in November 2010 with a series of vibration measurements performed on the Y-beam, which has been the first cryostat component installed in his final position at LNGS. Afterwards, the detector suspension has been pre-assembled and a second series of vibration measurements has been performed.

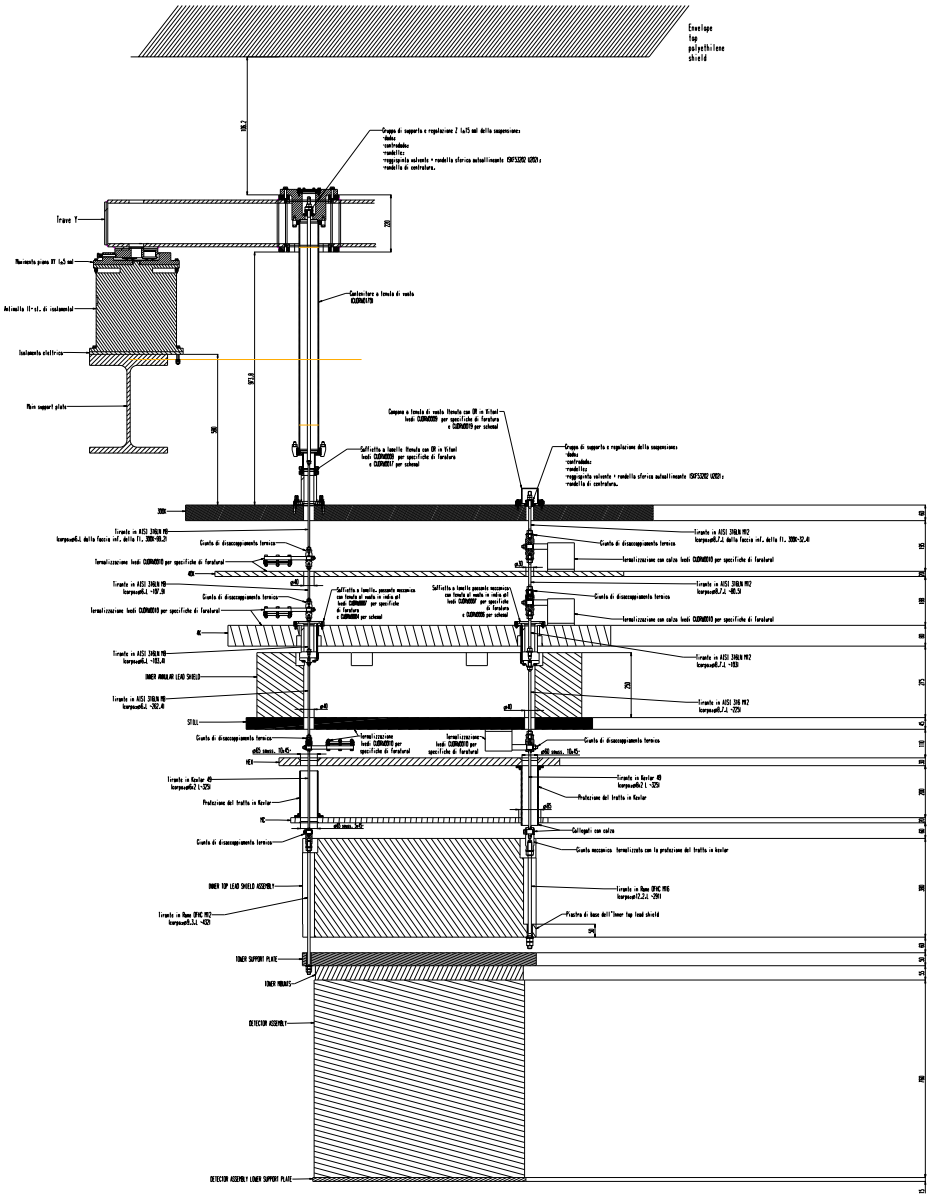

Figure 6.2: Schematic of the suspension system for the detector (left side) and for the lead shield just above the detector cryostat (right side).

6.2.1 Y-beam vibration measurements

The Y-beam is a crucial part of the CUORE active mass suspension: it is connected to the main support frame by three Minus-K springs, which have a cut frequency of 0.5Hz. To be sure that the cut is actually effective, it is necessary to know the proper frequencies of the Y-beam: a different transfer function from the expected one could arise if the Y-beam proper frequency is close to the Minus-K cut. The best condition to perform any vibration transfer measurement is obviously the final configuration. Anyhow several measurements with partial set-ups have been performed. The first measurement campaign was held with the goal to identify the first proper frequency of the Y-beam without any load and without unblocking the minus-K springs.

The Y-beam has been installed on the Minus-K springs on the main support frame. The Minus-K springs were in the "blocked" configuration: they can be "un-blocked" only when loaded with a weight of the same order of magnitude of the design operating value (i.e.$\sim$1.2 ton, the CUORE detector mass), otherwise their mechanism could be damaged. Fig. 6.3 shows a picture of the experimental set-up arranged on the second floor of the CUORE hut.

To perform the measurements, several Brüel & Kjær accelerometers have been used, coupled with proper pre-amplifiers and a National Instruments based acquisition system. Measurements of the ambient noise as well measurements with a known vibration source have been performed. A Brüel & Kjær 4810 shaker has been used as vibration source. The shaker was fixed to the Y-beam with a dedicated bolted bracket. In this way it was possible to excite the Y-beam both in vertical and in horizontal direction. The accelerometers have been fixed to the beam either with magnets or with wax. The different accelerometers have been equalized performing a series of calibration measurements. After this calibration, all the readouts could be compared on the same scale. The first measurement analyzed was the ambient noise. For a mechanical system, all the resonance modes are somehow coupled, so the ambient noise is in principle capable to excite all the proper modes. The attention was focused on the first 100Hz, where the problems could arise. The spectrum for all the 6 accelerometers is given in Fig. 6.4.

The power spectrum of Fig. 6.4 shows two main regions of interest and other three frequencies at which minor structures have been detected. The first region is around 20Hz, slightly lower for the horizontal direction than for the vertical. The second structure is at around 70 Hz, more evident in

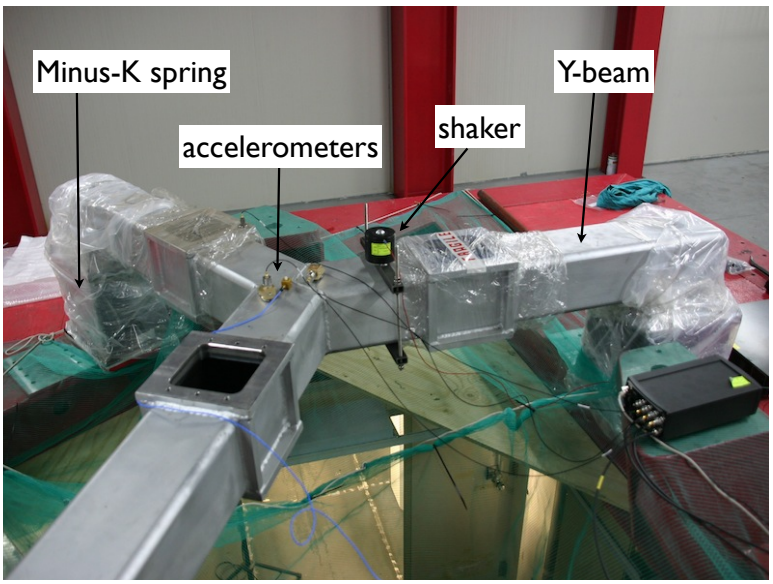

Figure 6.3: Arrangement of the Y-beam, Minus-K springs, shaker and accelerometers during the measurements.

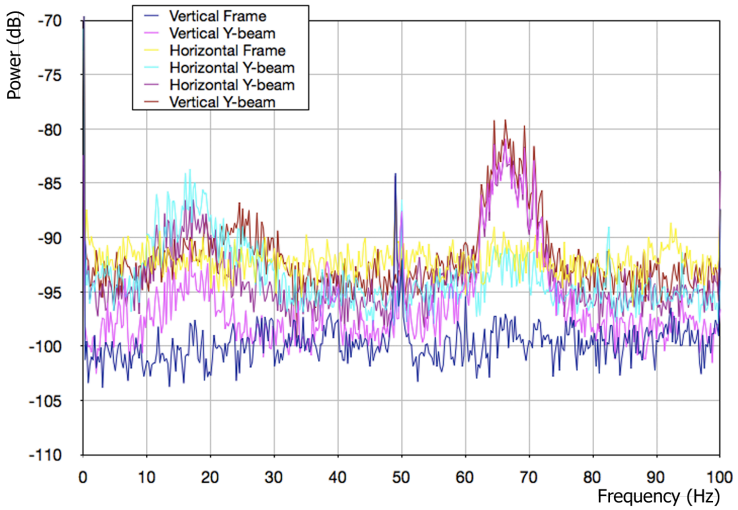

Figure 6.4: Power spectrum for all the accelerometers without any solicitations. Two structures are evident around 20 and 70Hz.

the vertical direction rather than in the horizontal. The structure around 50Hz has been identified as electromagnetic noise. Furthermore additional structures at few Hz and at around 90Hz have been investigated.

For the 70Hz region, several measurements were performed, both with the shaker placed in horizontal and in vertical direction, connected to the Y-beam. Tuning the forcing frequency around the expected one several structures were found. In particular, with the shaker in vertical direction, two resonances were found at 72.6 Hz and 77.2 Hz respectively. The first resonance is shown in Fig. 6.5. A similar resonance was found at ∼94 Hz, with the shaker in the horizontal direction. The source of those resonance has been identified as the natural frequencies of the Y-beam.

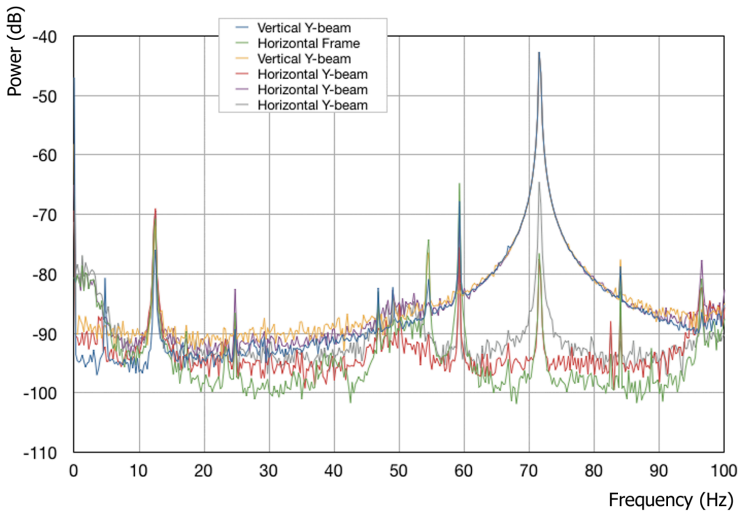

Figure 6.5: Power spectrum for all the accelerometers with a vertical excitation at 72.6Hz. It is evident how several sub-leading oscillations are excited.

Regarding the ∼20Hz resonance, the region was also studied with the shaker placed in both horizontal and vertical directions on the Y-beam. This resonance is sufficiently close to the Minus-K cut to be potentially harmful for the system. Consequently the maximum effort was dedicated to identify which was the part which was actually resonating. Placing the accelerometers in several different positions it was possible to proof that the maximum oscillation was measured on the Minus-K spring themselves:

the explanation was found in the fact that the Minus-K springs in "blocked" configuration are not sufficiently rigid to be considered as a good mechanical constraint for the Y-beam. This resonance can therefore be interpreted as an eigenfrequency of the entire main detector support. The frequency response was studied in detail and showed up an horizontal resonance at 23.6Hz. This resonance was evidenced with a variable solicitation in the range 20 - 40 Hz in horizontal direction, close to the centre of the Y-beam. Generally the same response was detected for all the accelerometers placed in the horizontal plane, both parallel and perpendicular to the excitation. The measurement of the response to this excitation is presented in Fig. 6.6.

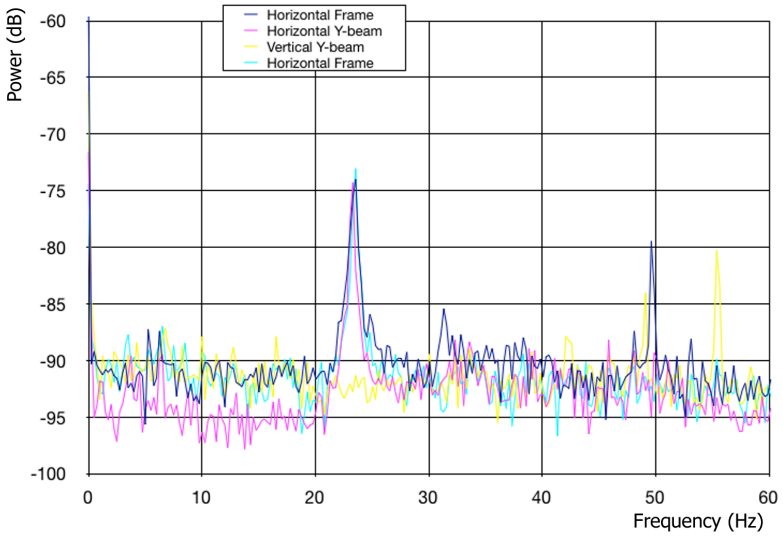

Figure 6.6: Power spectrum for different accelerometers with an excitation sweeping between 20 and 40Hz in horizontal direction. The resonance at 23.6Hz has been identified and related to the minus-K springs stiffness.

The last region of frequency analyzed in detail was the one at few Hertz. This region required a careful study, being very close to the minus-K cut-off. This frequency cannot be excited with the shaker Brüel & Kjær 4810, consequently it was decided to study the effects of a "manual" excitation. The results were evident: the entire support frame oscillates at a low frequency, due to the fact that the main detector support is installed on the top of a

series of elastomers. The frequencies values are 3Hz and 5.5Hz (Fig. 6.7).

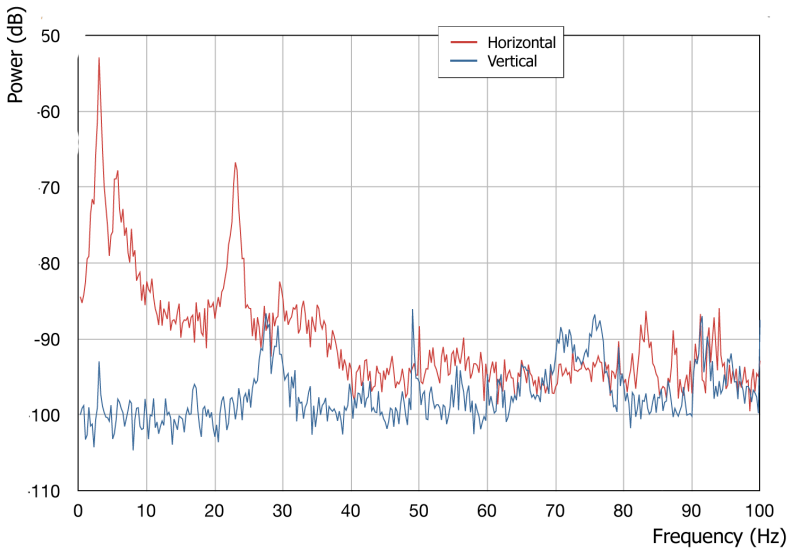

Figure 6.7: Power spectrum for a vertical and a horizontal accelerometer after a mechanical excitation of the platform. At 3Hz and 5.5Hz two resonances are visible and due to the elastomers at the bottom of the main detector support. At higher frequency the resonances already discussed are also visible.

The first measurement campaign performed was therefore not conclusive, but gave a reasonable confidence that there are no eigenfrequencies of the Y-beam lower than 70Hz. Another important aspect which was identified with this measurement is the pendulum-like behavior of the support as a whole. This behavior could change significantly when the detector will be installed with all the lead shields, i.e. when some weight will be attached directly to the main detector support.

6.2.2 Vibration measurements of the detector suspension

After the first preliminary measurement campaign, the whole suspension system has been installed in the CUORE hut and loaded with a lead dummy, simulating the real detector weight. With the proper load, it was also possible to un-block the Minus-k springs and proceed with the characterization

of the mechanical system.

Pictures of the mounted suspension are shown in Figures.6.8(a) and 6.8(b).

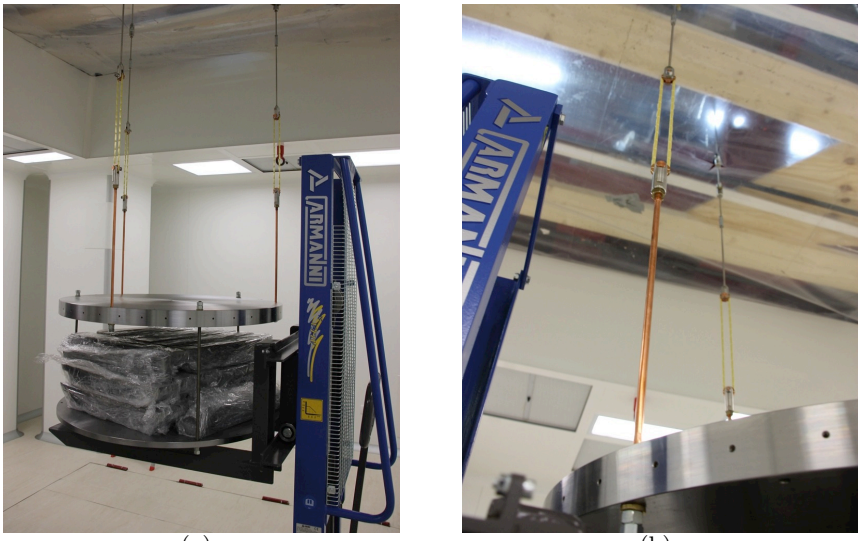

(a) (b)

Figure 6.8:

The same instrumentation described in Sect. 6.2.1 was used to perform the measurements. Different configurations have been considered, in order to identify the effect of the Minus-K springs on the vibration transmission along the detector suspension. The accelerometers have been installed in three positions: on the Main Support Plate (MSP), on the Y-beam and on the detector upper plate, both in horizontal and in vertical direction, both with and without mechanical solicitation of the MSP and of the Y-beam.

At first, it was considered the only effect of the Minus-K springs: two accelerometers were placed on the MSP (one in vertical and one in horizontal direction) and other two in vertical and horizontal direction on the Y-beam. The result, without excitations, is shown in Fig. 6.9. The Minus-K springs give a $\sim$35dB attenuation. The power spectrum is not deformed and it is flat. It is important to note that the MSP is mounted on top of a first stage of vibration damping, the elastomers, which acts as a low pass filter, exactly as the Minus-K.

The vibration transmission to the detector is shown in Fig. 6.10

On the detector it can be found, almost unchanged, the same vibration

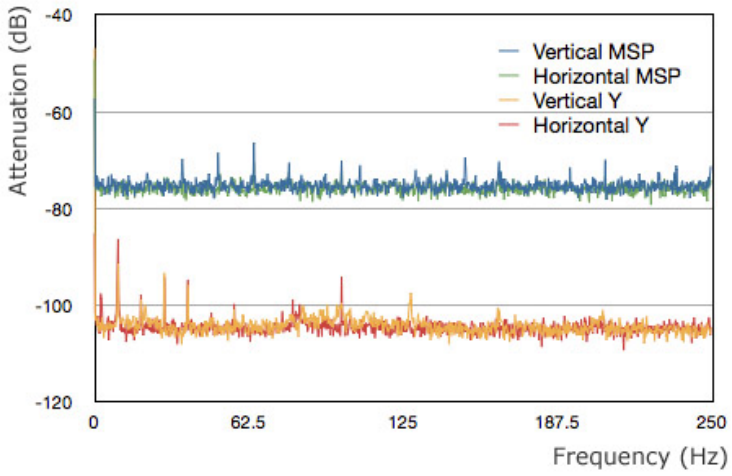

Figure 6.9: Comparison of the vibration spectrum, not forced, before the Minus-K springs (on the MSP, graphs blue and green) and after (on the Y-beam, graphs yellow and red).

spectrum measured on the Y- Beam. Some structure on the Y-Beam and detector spectra can be identified, but always smaller than the noise measured on the MSP. These structures can be compared to the ones measured in the previous campaign of measurements (see Fig. 6.6): the "bumps" on the detector spectrum and Y-beam correspond to the eigenfrequencies of the structure already identified in the past, with a significant attenuation due to the Minus-K springs.

Additionally it was also performed a number of measurements by acting a series of mechanical pulses on the MSP. These pulses generated a broad spectrum mechanical noise capable to transfer energy to the proper modes of the structure. The low frequency region of the acquired spectra are shown in Fig. 6.11. From Fig. 6.11 can be seen how the vertical modes on the detector are excited both by the vertical and horizontal modes of the Y-beam (top panel) and how the suspension plus detector system behaves as a pendulum, damping the horizontal oscillations (bottom panel).

From this measurement campaign, the following considerations can be done:

- the Minus-K springs work properly and guarantee a 35dB isolation with respect to the MSP. This number will be also a comparison value

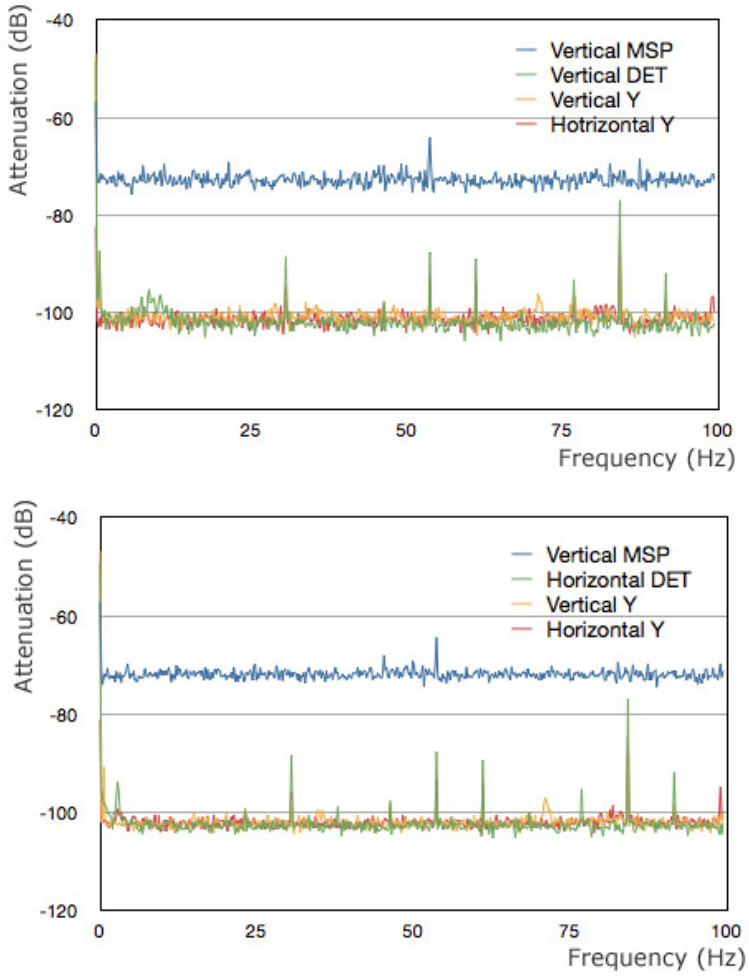

Figure 6.10: Comparison of the vibration spectrum (not forced) measured on the MSP(blue), on the Y-beam (red and yellow) and on the detector (green). On the top, the accelerometer is placed on the detector in the vertical direction, while in the bottom spectrum the accelerometer on the detector plate is in the horizontal direction.

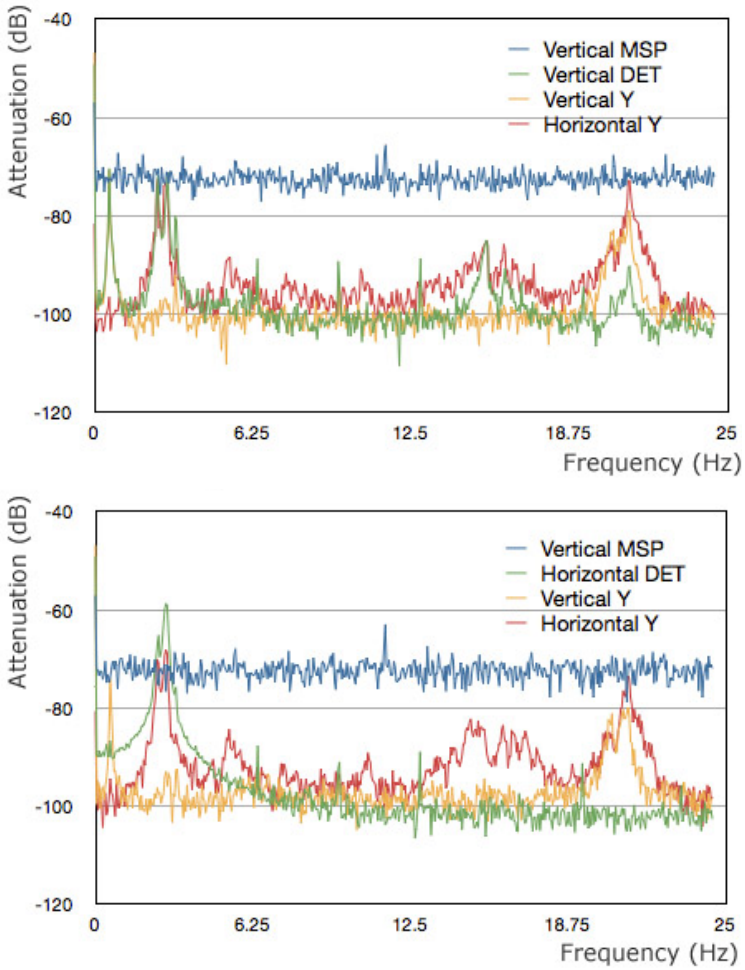

Figure 6.11: Comparison of the vibration spectrum (not forced) measured on the MSP(blue), on the Y-beam (red and yellow) and on the detector (green). On the top, the accelerometer is placed on the detector in the vertical direction, while in the bottom spectrum the accelerometer on the detector plate is in the horizontal direction.

for next measurements, when the bellows and the thermal joints will be attached to the suspension.

- The vibrations seen by the detector are very similar to what we can measure on the Y-beam. This will be very important for the monitoring of the detector during data taking, because the status of the vibrations on the detectors will be deducted only by measuring the vibrations on the Y-beam.

- The horizontal vibrations on the detector are damped by the detector plus suspension system. This aspect has to be taken into account for the evaluation of the effect of the vibrations on the crystals.

Further measurements will be done, including mechanical short-circuits bellows and thermal joints, during the mounting of the detector suspension in the final set-up, when also the cryostat plates will be assembled. Even if only with the final configuration it will be possible to understand the effective performances of the suspension, the results of the preliminary measurements are definitely satisfactory.

6.3 The Kevlar tie rods

Kevlar[1] 49 (Polyparaphenylene terephthalamide) is a commercial para - aramid synthetic fiber (see Fig. 6.12(a)). This material is widely used in cryogenic environments due to its excellent mechanical and thermal performances, in particular the low thermal conductivity [105] and the high tensile strength [106]. Due to these features, Kevlar 49 ropes were chosen for the construction of the CUORE suspension in the section between the 600mK plate and the Mixing Chamber of the cryostat. Kevlar 49 ropes strongly reduce the thermal conductivity, ensuring at the same time the required thermal insulation and mechanical stiffness. Its radioactivity is not a primary issue due to the small quantities used and its location above the top lead shield.

The information given in literature regarding the cryogenic mechanical properties of Kevlar is very limited. A characterization of its tensile strength and of its creep at low temperatures was then mandatory.

A few tie rods prototypes were realized for the ultimate tensile strength test at low temperature (4K). Each tie rod was made of 30 single rope winding. The measurements were performed at the L.A.S.A. (Laboratorio

[1]Kevlar is a registered trademark of the Dupont Corporation, Cortland, NY, USA.

(a)

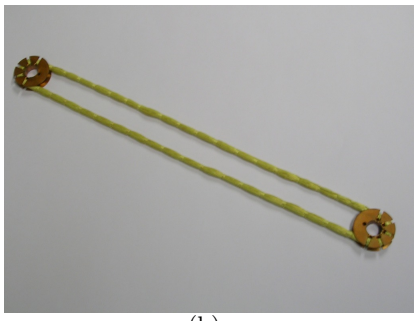

(b)

Figure 6.12: (a): the Kevlar fiber which will be used for the construction of the CUORE suspension. (b): Prototype of the rope used for the CUORE suspension test.

Acceleratori e Superconduttività Applicata, INFN and Physics Dept. of University of Milan) using a Instron 6027 machine for the monitoring of the strain behavior. The results for the five samples tested are shown in Fig. 6.13. The average tensile strength value of the single Kevlar fiber was measured equal to 185N. Considering that the three tie rods which will be used in CUORE have to support a total load of ∼1200 kg, (4033 N for each tie rod), and assuming a safety factor of 7, the final number of fibers for each tie rods has been set to (4033/185) ×7=153. In an extra-conservative approach the number of fibers in the final CUORE tie rods has been set to 160. An example of tie rod which will be used for the CUORE detector suspension is shown in Fig. 6.12(b). It is composed of 80 single fibers winding, equivalent to 160 fibers. Each of them is 32 cm long.

6.3.1 Kevlar creep at low temperature

Considering that the data taking of the CUORE experiment will last 5 years as minimum, it was decided to realize an experimental setup to test the long-term tensile strength of the Kevlar single fibers and to study a time dependent plastic deformation at constant load and at low temperature.

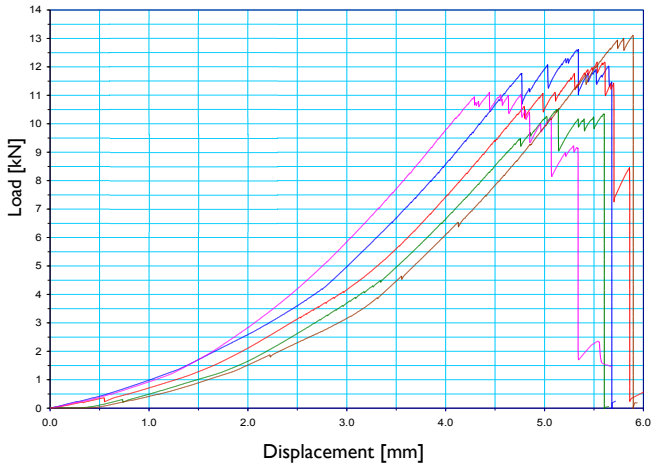

Figure 6.13: Stress - strain curves measured on the Kevlar tie rods prototypes. Each tie rod is constituted of 30 single rope winding, and the corresponding average tensile strength on the single rope is 185N.

Experimental realization

In order to measure the length variation of the Kevlar cord under stress at low temperature, a dedicated cylindrical capacitor has been designed and realized. The capacitance variation, proportional to the Kevlar length variation, was measured using the commercial instrument NS2000 manufactured by Queensgate [107]. This device is a non contact capacitive displacement measuring system which operates by comparing the impedance of the sensing electrodes with a fixed internal reference capacitance C_{ref}=10pF.

The specifications of the cylindrical capacitor have been carefully investigated in order to have a "work-capacitance" value at low temperature (4K) of the same order of magnitude of the one of the instrument (10pF).

To establish the correct dimensions of the capacitor components, the very simple model shown in Fig. 6.14 has been considered.

The capacitor is composed by an inner copper cylinder of radius R_1, covered by a layer $\Delta\epsilon$ of PTFE (Teflon) and enclosed by an outer copper cylinder with radius R_2. In this configuration, g is the gap between the outer surface of the dielectric and the outer copper cylinder of radius R_2. Due to mechanical construction constraints, it is necessary to limit the geometrical parameters as follows: $R_2 \leq 5$mm, $R_1 \geq 1$mm and g=10μm. The small value

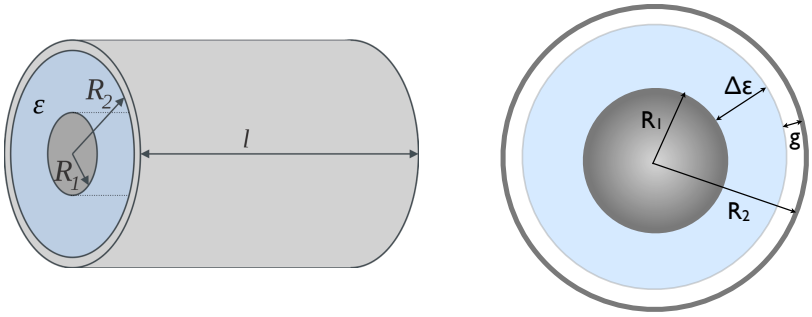

Figure 6.14: Sketch of the cylindrical capacitor.

of the gap in necessary to minimize the possibility of mis-alignment between the two cylindrical electrodes, potentially caused by the thermal contraction of the materials during the cooling down of the setup. The PTFE dielectric layer is necessary to minimize the range of this displacement and avoid electrical shorts between the internal and external electrodes.

The maximum difference in the capacitance due to radial-displacement has been evaluated keeping fixed the values of R_2 and g, for each different combination of R_1 and $\Delta\epsilon$: the capacitance (for unit of length) has been evaluated in the standard configuration (null displacement) and in the "worst" configuration (displacement equal to the gap g). The difference between these values has been plotted as a function of R_1 and $\Delta\epsilon$. An example is shown in Fig. 6.15.

It can be noted from Fig. 6.15 that the variation in the capacitance value (which can be also of the order of some pF) is less important if the dielectric layer is much greater than the internal radius R_1 of the capacitor.

To define the best configuration of the capacitor, it has to be considered also that the thermal contraction of copper from 300K to 4K implies dimensional variations of the order of 0.35% while the thermal contraction of PFTE, for the same temperature range, is slightly higher (∼2.2%).

It is therefore necessary to chose a thin layer $\Delta\epsilon$ of PTFE to minimize the effect of different thermal contractions of materials. Moreover, in order to minimize the edge effects, it is necessary that the axial length of the capacitor is high enough with respect to the radius (R/l <1 in Fig. 6.14).

Based on these considerations, aiming to obtain a "work capacitance" of the same order of magnitude of the reference capacitance C_{ref} of the instrument, the following parameters have been chosen: R_2=3 mm, R_1=1.7

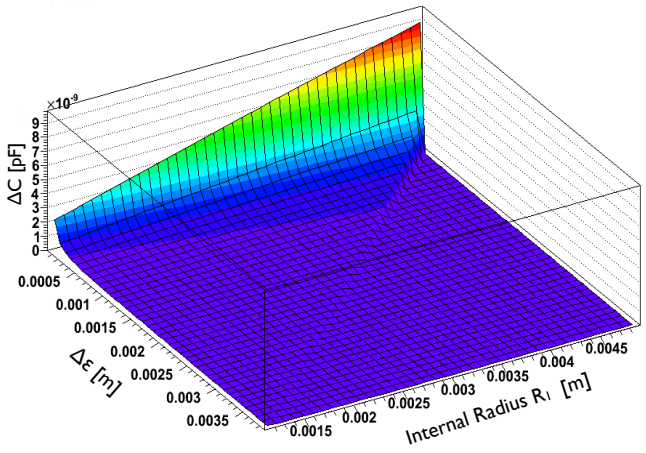

Figure 6.15: Plot of the maximal difference in the capacitance due to a mis-alignment of the cylindrical electrodes.

mm, $\Delta\epsilon$=1.29 mm and g=10μm. The capacitors realized in the mechanical workshop of the University of Genoa are shown in Fig. 6.16. For studying the reproducibility at various configurations, three different capacitors, C1, C2 and C3 have been realized, all three with the same features.

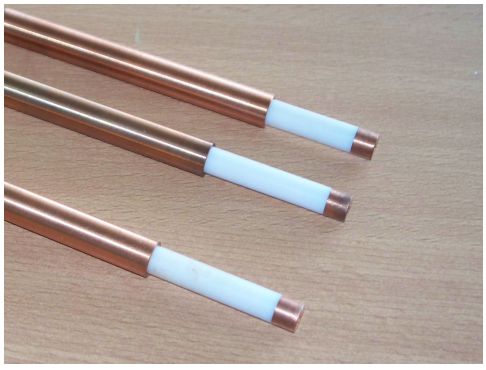

Figure 6.16: The three capacitors realized for the low temperature characterization of the single Kevlar fiber. The two cylindrical electrodes are made of copper, and are separated by a layer of PTFE.

In order to associate an axial displacement to the measured voltage vari-

ation, all the 3 capacitors were calibrated at room temperature. The displacement was controlled using a micrometer and the voltage output was recorded over a range of 2 cm. The obtained conversion factors, assuming in first approximation a linear dependance of the voltage from the displacement, are reported in Table 6.1.

Capacitor	Calibration factor [V/mm]
C1	0.25
C2	0.26
C3	0.23

Table 6.1: Calibration factors, evaluated at room temperature, used for the conversion of the measured voltage of the capacitors into a spatial displacement.

The Kevlar cord was then assembled to the capacitor as shown in the sketch of Fig. 6.17(a). With a reference to the Fig. 6.17(a), the cord is fixed using an epoxy glue, at one side (position A) to the bottom of the external copper cylinder, and at the other side (position B), at the top of the inner cylinder, for a total sensible length of ∼50 cm. The Kevlar fiber continues after the position B and is connected to a load at its end. In this way the setup can measure variations of capacitance (i.e. voltage ΔV) according to a variation of length ΔL: the measured voltage variation is thus a measurement of the extension of the Kevlar sample and an indication of the fiber creep. A detail of the experimental setup is shown in Fig 6.17(b). The same assembly procedure was adopted for all the three capacitors. The capacitor sensors were then enclosed in a refrigerator dewar and cooled down to the temperature of 4K. The complete setup is shown in Fig. 6.18. The readout signals cables exit from the dewar and are connected to the capacimeter (the black box in Fig.6.18 on the top of the dewar). Also the Kevlar fibers come out from the dewar and are connected to the loads, as can be seen in Fig.6.18. Operating Helium refill of the dewar every 3-4 days, the system was kept in this standard low-temperature configuration for several months. A National Instruments based acquisition system was used to record the voltage output of the capacimeter and to monitor the temperature and the helium level in the dewar.

The load applied on the fibers was chosen according to the CUORE specification. As described in the previous section, each CUORE tie rod will hold 4033N; being each tie rod made of 160 winding fibers, each single

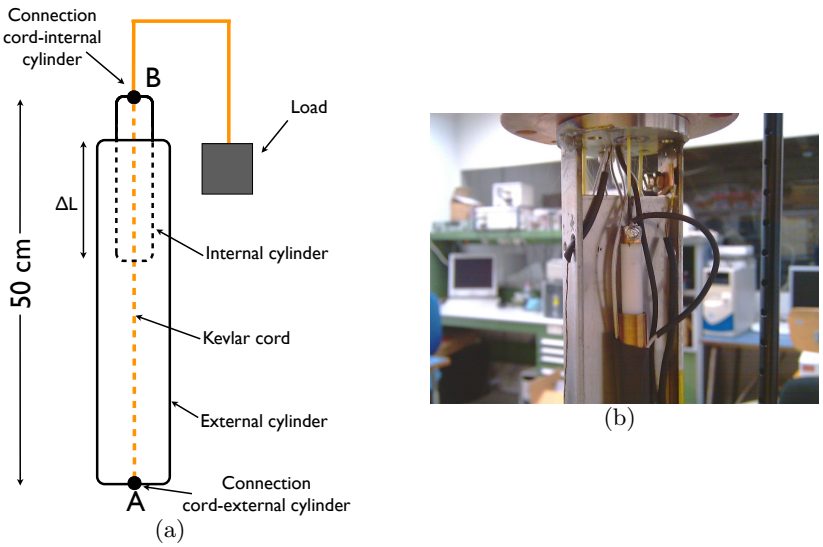

Figure 6.17: (a): sketch (not in scale) of the measuring technique. (b): detail of the experimental setup.

fiber will hold (4033/160)N=26N. For this reason, the capacitor C2 was loaded with the CUORE nominal value of 2.5 kg, while C1 and C3 were loaded with a mass of 2.7kg, 10% greater than the CUORE nominal value for the introduction of a further safety factor.

6.3.2 Data analysis and results

The system was kept in stable conditions for approximately 8 months, in order to study the long-term performances of the Kevlar fibers. The data recorded from capacitors C1, C2 and C3 are respectively shown in Figures 6.19, 6.20 and 6.21. In the plots are clearly visible the perturbation induced in the apparatus by the Helium refill of the dewar which were performed about twice a week.

Moreover, in each plot two structures can be observed at approximately 30 and 50 days since the beginning of the measurement: they are related to a problem occurred during the summer holidays in the air conditioning system of the room where the tests were carried out (the instrument for the capacitance monitoring is indeed very sensitive to temperature variation of the environment). After the repair of the air conditioning system, the measurement returned to a stable condition. The discontinuities in the data

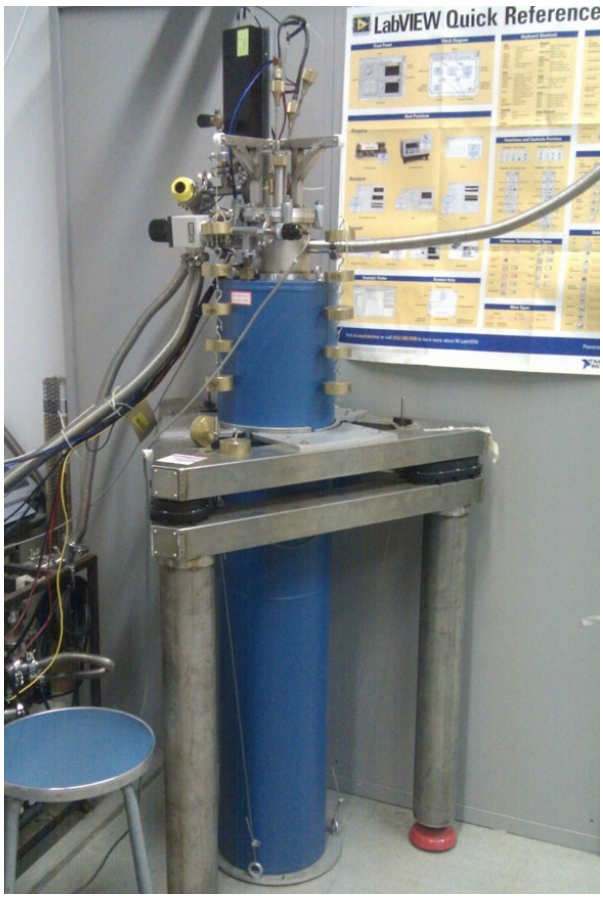

Figure 6.18: Experimental setup for the measurement of the Kevlar creep. The three capacitors are arranged inside the dewar refrigerator.

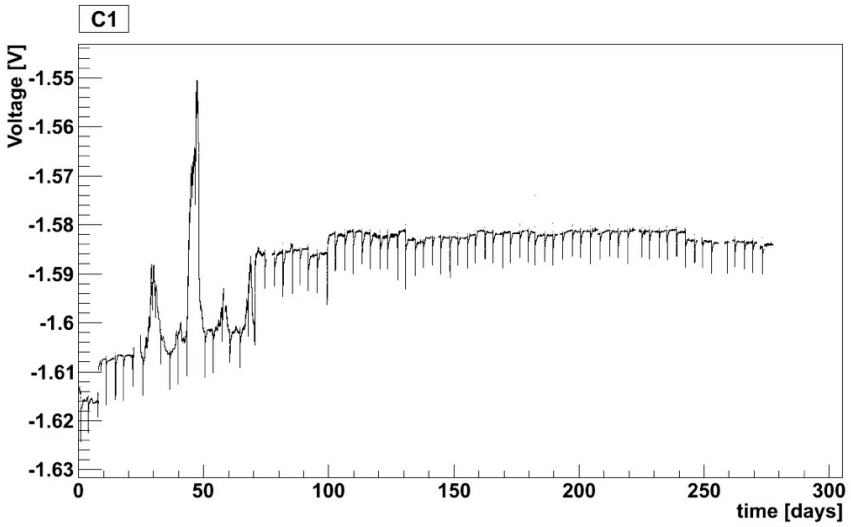

Figure 6.19: Plot of the voltage measured from the capacitor C1 during the data taking. The "spikes" represent the perturbation due to the Helium refill of the dewar.

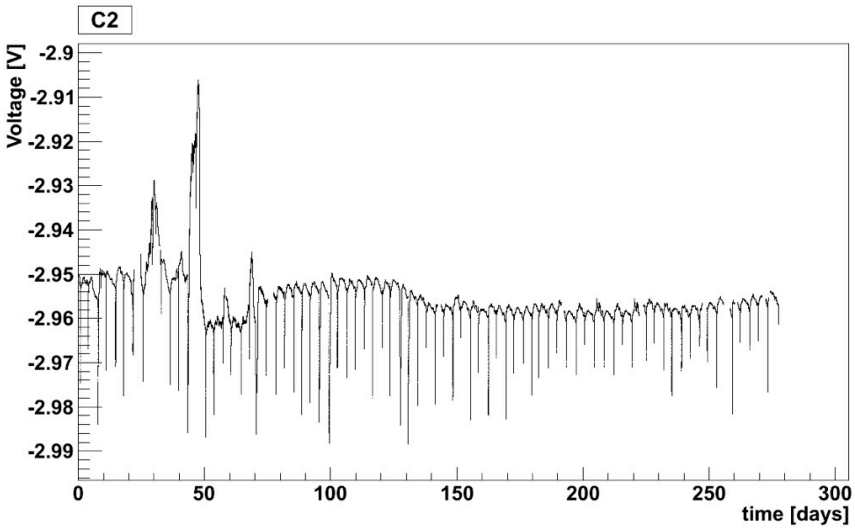

Figure 6.20: Plot of the voltage measured from the capacitor C2 during the data taking. The "spikes" represent the perturbation due to the Helium refill of the dewar.

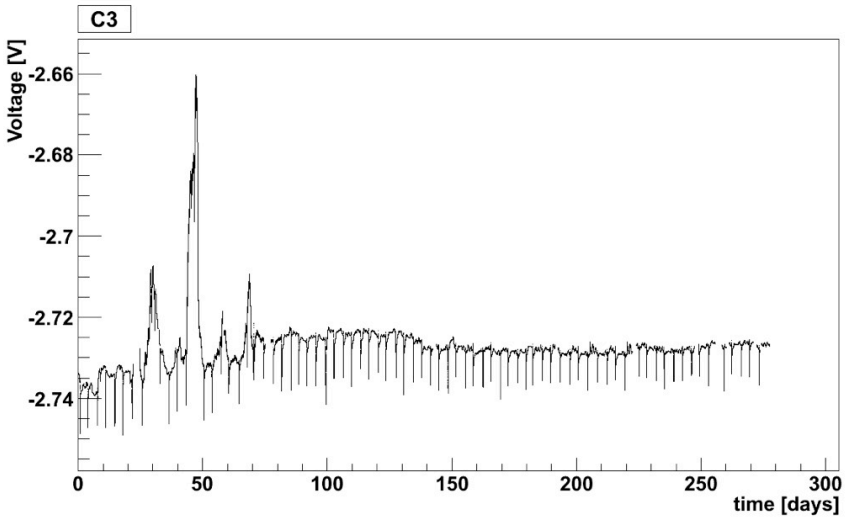

Figure 6.21: Plot of the voltage measured from the capacitor C3 during the data taking. The "spikes" represent the perturbation due to the Helium refill of the dewar.

due to Helium refill have been removed, and for each time interval between two refills the average voltage value has been evaluated. The result of this procedure is shown in Figures 6.22, 6.23 and 6.24 respectively for capacitors C1, C2 and C3.

Due to the trouble occurred at the air-conditioning system, two different approaches have been adopted for the analysis of data: a more conservative one, considering the total acquired statistic (from days 0 to 235) and a second one, considering only the sub-set of data after the repair of the air-conditioning system (from day 74 to 235).

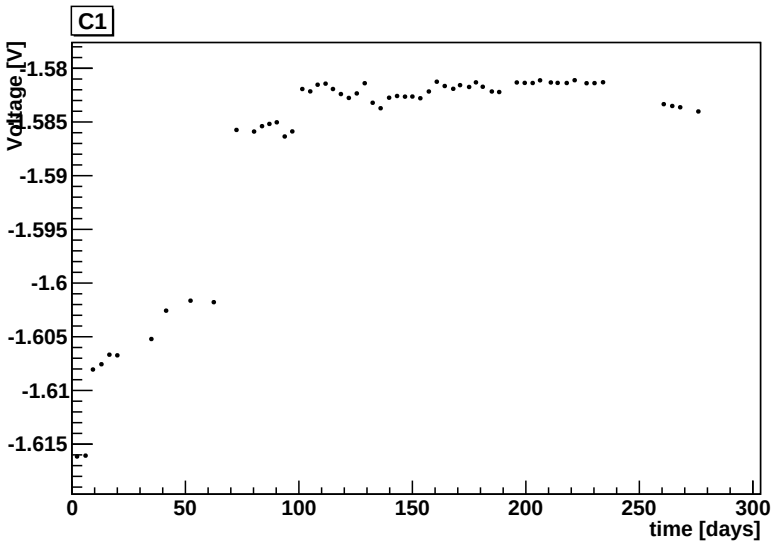

Figure 6.22: Plot of the voltage measured from the capacitor C1 during the data taking after the removal of the perturbation induced from the Helium refill of the system.

To estimate the capacitance variation, namely the voltage variation which corresponds to the extension of the Kevlar cord, the voltage values at the beginning and at the end of the measurement have been evaluated. As mentioned before, two different configuration have been considered: Tab. 6.2 shows the values for the most conservative approach, considering the time interval since the beginning of data taking, while Tab. 6.3 shows the values considering only the time interval from day 74 to 235.

The tables show also the values for the absolute and relative extension of the Kevlar cord in both approaches.

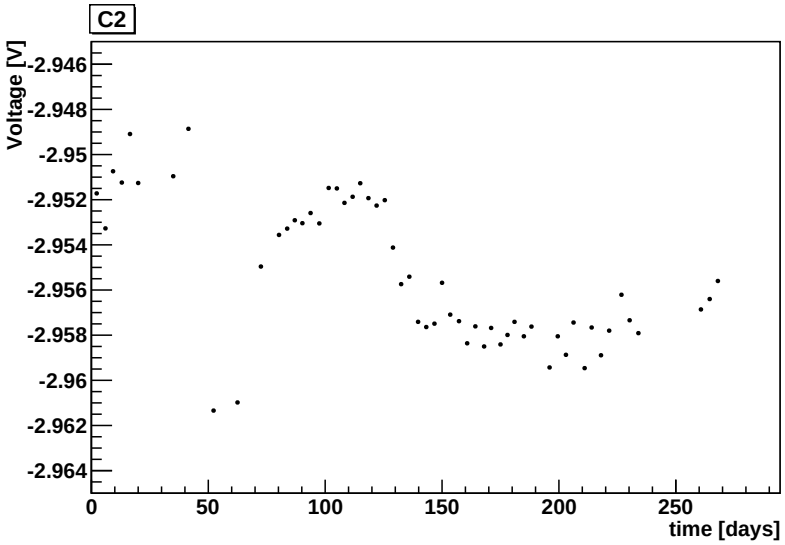

Figure 6.23: Plot of the voltage measured from the capacitor C2 during the data taking after the removal of the perturbation induced from the Helium refill of the system.

	load [kg]	day 0 [V]	day 235 [V]	ΔV (0-235)d [V]	ΔL (0-235)d [mm]	ΔL/L [%]
C1	2.7	-1.616	-1.581	0.035	0.139	0.028
C2	2.5	-2.952	-2.958	0.006	0.024	0.005
C3	2.7	-2.737	-2.728	0.010	0.041	0.008

Table 6.2: Measured voltage values and corresponding length variations for each capacitor, in the most conservative hypothesis, corresponding to the time interval (0-235).

	load [kg]	day 74 [V]	day 235 [V]	ΔV (74-235)d [V]	ΔL (0-235)d [mm]	ΔL/L [%]
C1	2.7	-1.586	-1.581	0.004	0.018	0.004
C2	2.5	-2.955	-2.958	0.003	0.011	0.002
C3	2.7	-2.725	-2.728	0.003	0.013	0.003

Table 6.3: Measured voltage values and corresponding length variations for each capacitor, considering the time interval from day 74 to 235.

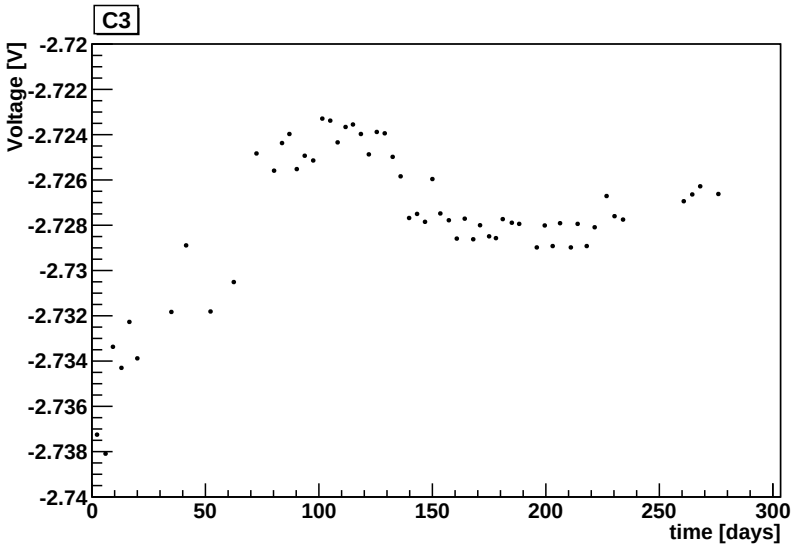

Figure 6.24: Plot of the voltage measured from the capacitor C3 during the data taking after the removal of the perturbation induced from the Helium refill of the system.

The worst configuration corresponds to the capacitor C1, stressed with a load of 2.7kg: in this case the total extension of the cord since the beginning (day 0) to the end of the measurement (day 235) is of 0.139 mm over 500 mm, corresponding to a relative factor of 0.028%. While if it is considered only the last subset of data, from day 74 to day 235, the corresponding extension in about one order of magnitude smaller, 0.018 mm over 500 mm (0.004%).

As mentioned before, the CUORE experiment is supposed to operate for 5 years at least. It is therefore interesting to estimate the potential extension of the Kevlar single fiber which will be used to build the detector suspension.

Adopting the simplification to consider the dependency of the deformation constant and linear with respect to the time, it is possible to foresee which could be the values of the extension of the CUORE tie rods (320 mm long) at the end of the experiment. The calculated values are reported in Tab. 6.4.

Capacitor	load [kg]	5 years extension (0-234)d [mm]	5 years extension (74-235)d [mm]
C1	2.7	0.69	0.31
C2	2.5	0.12	0.05
C3	2.7	0.21	0.09

Table 6.4: Values of the potential extension of the CUORE Kevar tie rods after 5 years. The values are extrapolated from the results of Tables 6.2 and 6.3.

In the worst scenario, the single Kevlar fiber will elongate ∼0.7 mm, a value which is compliant to the CUORE construction specifications, despite has been evaluated under very conservative assumptions.

Conclusions

The two central topics presented in this PhD thesis are the measurements performed on the CUORE crystals and the characterization of the detector suspension.

In this thesis the results of the radiopurity measurements of the first 18 CUORE crystals have been presented. The CCVRs background rate shows a reduction with respect to the one measured in CUORICINO in all the energy regions considered. The bulk activity of ^{210}Po is measured to be within the limit specified in the contract with the crystals producer. No indication of a bulk contamination from uranium and thorium decay chains, as well as from ^{210}Pb (out of equilibrium), was detected. The upper limits are calculated to be within the contract specification. No indication of a surface contamination from uranium and thorium decay chains was found. Upper limits at 90% C.L. were calculated for surface contamination from several nuclides and for different contamination depths. An extrapolation to CUORE background from both bulk and surface contaminations was performed, in the most conservative assumption that the CCVRs observed background is entirely due to the bulk and the surface contamination respectively. The upper limits to the CUORE background index in the energy region around the ^{130}Te Q-value due to crystal bulk and surface contaminations were determined to be respectively $1.1 \cdot 10^{-4}$ counts/keV/kg/y and $4.2 \cdot 10^{-3}$ counts/keV/kg/y. Both these value are compliant with the CUORE goal of 10^{-2} counts/keV/kg/y.

The other topic of this PhD thesis is the characterization of the suspension system. At first, a series of vibration measurements were performed on the Y-Beam, with the goal to identify its low frequency resonances. The first resonance of the Y-Beam has been identified at the frequency of $\sim$70 Hz: this value, far from the Minus-K springs cut-off, should guarantee an effective vibration reduction. This reduction was confirmed during the second measurement campaign, when the whole suspension has been installed and loaded with a lead dummy, simulating the detector weight. The mea-

surement performed demonstrated the isolation efficiency of the detector suspension system. Moreover, an experimental setup was realized to characterize the low temperature properties of Kevlar 49, a synthetic fiber that will be used for the construction of the CUORE suspension. The results obtained on the long-term tensile strength indicate that the material is suitable for the realization of the suspension tie rods.

Bibliography

[1] M. Peskin and D. Schroeder, *Introduction to quantum field theory*. Advanced Book Program, Addison-Wesley Pub. Co., 1995.

[2] B. T. Cleveland *et al.*, "Measurement of the solar electron neutrino flux with the Homestake chlorine detector," *Astrophys. J.*, vol. 496, pp. 505–526, 1998.

[3] W. Hampel *et al.*, "GALLEX solar neutrino observations: Results for GALLEX IV," *Phys. Lett.*, vol. B447, pp. 127–133, 1999.

[4] J. N. Abdurashitov *et al.*, "Measurement of the solar neutrino capture rate with gallium metal," *Phys. Rev.*, vol. C60, p. 055801, 1999.

[5] Y. Fukuda *et al.*, "Measurements of the solar neutrino flux from Super-Kamiokande's first 300 days," *Phys.Rev.Lett.*, vol. 81, pp. 1158–1162, 1998.

[6] Q. Ahmad *et al.*, "Direct evidence for neutrino flavor transformation from neutral current interactions in the Sudbury Neutrino Observatory," *Phys.Rev.Lett.*, vol. 89, p. 011301, 2002.

[7] S. Ahmed *et al.*, "Measurement of the total active B-8 solar neutrino flux at the Sudbury Neutrino Observatory with enhanced neutral current sensitivity," *Phys.Rev.Lett.*, vol. 92, p. 181301, 2004.

[8] S. Abe *et al.*, "Precision Measurement of Neutrino Oscillation Parameters with KamLAND," *Physical Review Letters*, vol. 100, p. 221803, 2008.

[9] G. Fogli *et al.*, "Evidence of θ_{13} from global neutrino data analysis," *Phys.Rev.*, vol. D84, p. 053007, 2011.

[10] D. Kielczewska, "Oscillatory signature in atmospheric neutrinos," *Int. J. Mod. Phys.*, vol. A20, pp. 3102–3105, 2005.

[11] M. Ahn *et al.*, "Measurement of Neutrino Oscillation by the K2K Experiment," *Phys.Rev.*, vol. D74, p. 072003, 2006.

[12] P. Adamson *et al.*, "Measurement of Neutrino Oscillations with the MINOS Detectors in the NuMI Beam," *Phys.Rev.Lett.*, vol. 101, p. 131802, 2008.

[13] M. Apollonio *et al.*, "Limits on Neutrino Oscillations from the CHOOZ Experiment," *Phys. Lett.*, vol. B466, pp. 415–430, 1999.

[14] F. Boehm *et al.*, "Final results from the Palo Verde Neutrino Oscillation Experiment," *Phys. Rev.*, vol. D64, p. 112001, 2001.

[15] K. Abe *et al.*, "Indication of Electron Neutrino Appearance from an Accelerator-produced Off-axis Muon Neutrino Beam," *Phys.Rev.Lett.*, vol. 107, p. 041801, 2011.

[16] P. Adamson *et al.*, "Improved search for muon-neutrino to electron-neutrino oscillations in MINOS," *Phys.Rev.Lett.*, vol. 107, p. 181802, 2011.

[17] S. R. Elliott *et al.*, "Experimental investigation of double-beta decay in ^{82}Se," *Phys. Rev. Lett.*, vol. 56, pp. 2582–2585, Jun 1986.

[18] A. Balysh *et al.*, "Double beta decay of ^{48}ca," *PHYS.REV.LETT.*, vol. 77, p. 5186, 1996.

[19] V. Brudanin *et al.*, "Search for double beta decay of Ca-48 in the TGV experiment," *Phys.Lett.*, vol. B495, pp. 63–68, 2000.

[20] R. L. Flack, "Results from NEMO-3," *J.Phys.Conf.Ser.*, vol. 136, p. 022032, 2008.

[21] F. T. Avignone, "Double-beta decay: Some recent results and developments," *Prog. Part. Nucl. Phys.*, vol. 32, pp. 223–245, 1994.

[22] A. Morales, "Review on double beta decay experiments and comparison with theory," *NUCL.PHYS.PROC.*, vol. 77, p. 335, 1999.

[23] C. Dorr and H. Klapdor-Kleingrothaus, "New Monte-Carlo simulation of the HEIDELBERG-MOSCOW double beta decay experiment," *Nucl.Instrum.Meth.*, vol. A513, pp. 596–621, 2003.

[24] R. Arnold *et al.*, "First results of the search for neutrinoless double-beta decay with the nemo 3 detector," *Phys. Rev. Lett.*, vol. 95, p. 182302, Oct 2005.

[25] S. R. Elliott *et al.*, "Double beta decay of ^{82}Se," *Phys. Rev. C*, vol. 46, pp. 1535–1537, Oct 1992.

[26] R. Arnold *et al.*, "Double beta decay of Se-82," *Nucl.Phys.*, vol. A636, pp. 209–223, 1998.

[27] R. Arnold *et al.*, "Double beta decay of Zr-96," *Nucl.Phys.*, vol. A658, pp. 299–312, 1999.

[28] D. Dassie *et al.*, "Two neutrino double beta decay measurement of Mo-100," *Phys.Rev.*, vol. D51, pp. 2090–2100, 1995.

[29] A. S. De Silva *et al.*, "Double beta decays of Mo-100 and Nd-150," *Phys.Rev.*, vol. C56, pp. 2451–2467, 1997.

[30] H. Ejiri *et al.*, "Double beta decays of Cd-116," *J.Phys.Soc.Jap.*, vol. 64, pp. 339–343, 1995.

[31] F. A. Danevich *et al.*, "Search for 2 beta decay of cadmium and tungsten isotopes: Final results of the solotvina experiment," *Phys.Rev.*, vol. C68, p. 035501, 2003.

[32] R. Arnold *et al.*, "Double-beta decay of Cd-116," *Z.Phys.*, vol. C72, pp. 239–247, 1996.

[33] C. Arnaboldi *et al.*, "A Calorimetric search on double beta decay of Te-130," *Phys.Lett.*, vol. B557, pp. 167–175, 2003.

[34] V. Tretyak, "Recent results of the NEMO 3 experiment," *AIP Conf.Proc.*, vol. 1180, pp. 135–139, 2009.

[35] N. Ackerman *et al.*, "Observation of Two-Neutrino Double-Beta Decay in Xe-136 with EXO-200," *Phys. Rev. Lett.*, vol. 107, p. 212501, 2011.

[36] "Measurement of the Double-Beta Decay Half-life of ^{136}Xe in KamLAND-Zen," 2012.

[37] V. Artemiev *et al.*, "Half-life measurement for ^{150}Nd $2\beta2\nu$ decay in the Time Projection Chamber experiment," *Physics Letters B*, vol. 345, pp. 564–568, Feb. 1995.

[38] J. Argyriades *et al.*, "Measurement of the Double Beta Decay Half-life of Nd-150 and Search for Neutrinoless Decay Modes with the NEMO-3 Detector," *Phys.Rev.*, vol. C80, p. 032501, 2009.

[39] F. T. Avignone *et al.*, "Double Beta Decay, Majorana Neutrinos, and Neutrino Mass," *Rev.Mod.Phys.*, vol. 80, pp. 481–516, 2008.

[40] I. Ogawa *et al.*, "Search for neutrino-less double beta decay of Ca-48 by CaF-2 scintillator," *Nuclear Physics A*, vol. 730, pp. 215–223, 2004.

[41] H. V. Klapdor-Kleingrothaus *et al.*, "Latest Results from the Heidelberg-Moscow Double Beta Decay Experiment," *Eur. Phys. J.*, vol. A12, pp. 147–154, 2001.

[42] H. V. Klapdor-Kleingrothaus *et al.*, "Search for neutrinoless double beta decay with enriched 76Ge in Gran Sasso 1990-2003," *Physics Letters B*, vol. 586, pp. 198–212, 2004.

[43] R. Arnold *et al.*, "First results of the search of neutrinoless double beta decay with the NEMO 3 detector," *Physical Review Letters*, vol. 95, p. 182302, 2005.

[44] R. Arnold *et al.*, "Double beta decay of Zr-96," *Nucl. Phys.*, vol. A658, pp. 299–312, 1999.

[45] F. A. Danevich *et al.*, "Search for 2 beta decay of cadmium and tungsten isotopes: Final results of the Solotvina experiment," *Physical Review C*, vol. 68, p. 035501, 2003.

[46] E. Andreotti *et al.*, "^{130}Te Neutrinoless Double-Beta Decay with Cuoricino," *Astropart.Phys.*, vol. 34, pp. 822–831, 2011.

[47] R. Bernabei *et al.*, "Investigation of beta beta decay modes in Xe-134 and Xe- 136," *Physics Letters B*, vol. 546, pp. 23–28, 2002.

[48] J. Argyriades, "Measurement of the Double Beta Decay Half-life of 150-Nd and Search for Neutrinoless Decay Modes with the NEMO-3 Detector," 2008.

[49] A. Strumia and F. Vissani, "Neutrino masses and mixings and...," 2006.

[50] J. Menendez *et al.*, "Disassembling the Nuclear Matrix Elements of the Neutrinoless beta beta Decay," *Nucl.Phys.*, vol. A818, pp. 139–151, 2009.

[51] F. Simkovic *et al.*, "Anatomy of nuclear matrix elements for neutrinoless double-beta decay," *Phys.Rev.*, vol. C77, p. 045503, 2008.

[52] J. Barea and F. Iachello, "Neutrinoless double-beta decay in the microscopic interacting boson model," *Phys.Rev.*, vol. C79, p. 044301, 2009.

[53] T. R. Rodriguez and G. Martinez-Pinedo, "Energy density functional study of nuclear matrix elements for neutrinoless $\beta\beta$ decay," *Phys.Rev.Lett.*, vol. 105, p. 252503, 2010.

[54] V. Rodin, "Status of calculations of $M^{0\nu}$," *Conference TAUP 2011, Munich, Germany*, 2011.

[55] S. R. Elliott and P. Vogel, "Double beta decay," *Ann. Rev. Nucl. Part. Sci.*, vol. 52, pp. 115–151, 2002.

[56] F. T. Avignone *et al.*, "Next generation double-beta decay experiments: Metrics for their evaluation," *New J. Phys.*, vol. 7, p. 6, 2005.

[57] M. Gunther *et al.*, "Heidelberg - Moscow beta beta experiment with Ge-76: Full setup with five detectors," *Phys. Rev.*, vol. D55, pp. 54–67, 1997.

[58] C. E. Aalseth *et al.*, "Recent results of the IGEX Ge-76 double-beta decay experiment," *Phys. Atom. Nucl.*, vol. 63, pp. 1225–1228, 2000.

[59] H. V. Klapdor-Kleingrothaus and I. V. Krivosheina, "The evidence for the observation of 0nu beta beta decay: The identification of 0nu beta beta events from the full spectra," *Mod. Phys. Lett.*, vol. A21, pp. 1547–1566, 2006.

[60] L. Baudis *et al.*, "Limits on the Majorana neutrino mass in the 0.1eV range," *Phys.Rev.Lett.*, vol. 83, pp. 41–44, 1999.

[61] H. Klapdor-Kleingrothaus *et al.*, "Evidence for neutrinoless double beta decay," *Mod.Phys.Lett.*, vol. A16, pp. 2409–2420, 2001.

[62] C. Aalseth *et al.*, "Comment on 'Evidence for neutrinoless double beta decay'," *Mod.Phys.Lett.*, vol. A17, pp. 1475–1478, 2002.

[63] F. Feruglio *et al.*, "Neutrino oscillations and signals in beta and $0\nu2\beta$ experiments," *Nucl.Phys.*, vol. B637, pp. 345–377, 2002.

[64] H. Klapdor-Kleingrothaus *et al.*, "Data acquisition and analysis of the Ge-76 double beta experiment in Gran Sasso 1990-2003," *Nucl.Instrum.Meth.*, vol. A522, pp. 371–406, 2004.

[65] H. V. Klapdor-Kleingrothaus and I. V. Krivosheina, "The evidence for the observation of $0\nu\beta\beta$ decay: The identification of $0\nu\beta\beta$ events from the full spectra," *Mod. Phys. Lett.*, vol. A21, pp. 1547–1566, 2006.

[66] C. Aalseth *et al.*, "The IGEX Ge-76 neutrinoless double beta decay experiment: Prospects for next generation experiments," *Phys.Rev.*, vol. D65, p. 092007, 2002.

[67] R. Arnold *et al.*, "Technical design and performance of the NEMO 3 detector," *Nucl. Instrum. Meth.*, vol. A536, pp. 79–122, 2005.

[68] J. Argyriades *et al.*, "Measurement of the two neutrino double beta decay half-life of Zr-96 with the NEMO-3 detector," *Nucl.Phys.*, vol. A847, pp. 168–179, 2010.

[69] I. Abt *et al.*, "A New Ge-76 double beta decay experiment at LNGS: Letter of intent," 2004.

[70] C. Aalseth *et al.*, "The Majorana Project," *J.Phys.Conf.Ser.*, vol. 203, p. 012057, 2010.

[71] C. Aalseth *et al.*, "The MAJORANA demonstrator: An R&D project towards a ton-scale germanium neutrinoless double-beta decay search," *AIP Conf.Proc.*, vol. 1182, pp. 88–91, 2009.

[72] R. Ardito *et al.*, "CUORE: A cryogenic underground observatory for rare events," 2005. [arXiv:hep-ex/0501010].

[73] M. Danilov *et al.*, "Detection of very small neutrino masses in double-beta decay using laser tagging," *Phys. Lett.*, vol. B480, pp. 12–18, 2000.

[74] A. Terashima *et al.*, "R&D for possible future improvements of KamLAND," *J. Phys. Conf. Ser.*, vol. 120, p. 052029, 2008.

[75] R. Arnold *et al.*, "Probing New Physics Models of Neutrinoless Double Beta Decay with SuperNEMO," *Eur.Phys.J.*, vol. C70, pp. 927–943, 2010.

[76] J. Maneira, "Status and prospects of SNO+," *Nucl.Phys.Proc.Suppl.*, vol. 217, pp. 50–52, 2011.

[77] I. Ogawa *et al.*, "Study of Ca-48 double beta decay by CANDLES," *J.Phys.Conf.Ser.*, vol. 312, p. 072014, 2011.

[78] C. Kittel, *Introduction to solid state physics*. Wiley series on the science and technology of materials, Wiley, 1956.

[79] N. F. Mott and J. H. Davies, "Metalinsulator transition in doped semiconductors," *Philosophical Magazine B*, vol. 42, pp. 845–858, 1980.

[80] A. Miller and E. Abrahams, "Impurity Conduction at Low Concentrations," *Physical Review*, vol. 120, pp. 745–755, Nov. 1960.

[81] K. M. Itoh *et al.*, "Hopping Conduction and Metal-Insulator Transition in Isotopically Enriched Neutron-Transmutation-Doped ^{70}Ge:Ga," *Phys. Rev. Lett.*, vol. 77, pp. 4058–4061, Nov 1996.

[82] E. Fiorini and T. Niinikoski, "Low temperature calorimetry for rare dacays," *Nucl.Instrum.Meth.*, vol. A224, p. 83, 1984.

[83] A. Alessandrello *et al.*, "A New search for neutrinoless beta beta decay with a thermal detector," *Phys.Lett.*, vol. B335, pp. 519–525, 1994.

[84] A. Alessandrello *et al.*, "Preliminary results on double beta decay of Te-130 with an array of twenty cryogenic detectors," *Phys.Lett.*, vol. B433, pp. 156–162, 1998.

[85] A. Alessandrello *et al.*, "New experimental results on double beta decay of Te-130," *Phys.Lett.*, vol. B486, pp. 13–21, 2000.

[86] S. P. Ahlen *et al.*, "Study of penetrating cosmic ray muons and search for large scale anisotropies at the Gran Sasso Laboratory," *Physics Letters B*, vol. 249, pp. 149–156, 1990.

[87] P. Belli *et al.*, "Deep Underground Neutron Flux Measurement With Large Bf-3 Counters," *Il Nuovo Cimento A*, vol. 101, pp. 959–966, 1989.

[88] E. Andreotti *et al.*, "Muon-induced backgrounds in the Cuoricino experiment," *Astropart.Phys.*, vol. 34, pp. 18–24, 2010.

[89] M. Redshaw *et al.*, "Masses of Te-130 and Xe-130 and Double-beta-Decay Q Value of Te-130," *Phys.Rev.Lett.*, vol. 102, p. 212502, 2009.

[90] A. Alessandrello *et al.*, "A Cryogenic tellurium detector for rare events and gamma-rays," *Phys.Lett.*, vol. B247, pp. 442–447, 1990.

[91] A. Alessandrello *et al.*, "Production of high purity TeO_2 single crystals for the study of neutrinoless double beta decay," *Journal of Crystal Growth*, vol. 312, pp. 2999–3008, 2010.

[92] Y. Chu *et al.*, "Growth of the high quality and large size paratellurite single crystals," *Journal of Crystal Growth*, vol. 295, pp. 158–161, 2006.

[93] Y. Chu *et al.*, "Growth of $\varnothing 4$" $Li_2B_4O_7$ single crystals by multi-crucible Bridgman method," *Journal of Crystal Growth*, vol. 264, pp. 260–265, 2004.

[94] G. Harman, *Wire bonding in microelectronics: materials, processes, reliability, and yield*. Electronic packaging and interconnection series, McGraw-Hill, 1997.

[95] A. Alessandrello *et al.*, "Methods for response stabilization in bolometers for rare decays," *Nucl.Instrum.Meth.*, vol. A412, pp. 454–464, 1998.

[96] "Three Tower Test: copper surface treatments for low background DBD experiments with TeO_2 bolometers," *Paper in preparation*.

[97] P. Astone *et al.*, "Long-term operation of the Rome EXPLORER cryogenic gravitational wave detector," *Phys. Rev. D*, vol. 47, pp. 362–375, Jan 1993.

[98] C. Arnaboldi *et al.*, "The front-end readout for cuoricino, an array of macro-bolometers and MIBETA, an array of μ-bolometers," *Nuclear Instruments and Methods in Physics Research Sec.A*, vol. 520, pp. 578–580, 2004.

[99] E. Gatti and P. Manfredi, "Processing the signals from solid-state detectors in elementary-particle physics," *La Rivista del Nuovo Cimento (1978-1999)*, vol. 9, pp. 1–146, 1986. 10.1007/BF02822156.

[100] C. Arnaboldi *et al.*, "The temperature stabilization system of Cuoricino: An array of macro bolometers," *IEEE Trans. Nucl. Sci.*, vol. 52, pp. 1630–1637, 2005.

[101] F. Bellini *et al.*, "Monte Carlo evaluation of the external gamma, neutron and muon induced background sources in the CUORE experiment," *Astropart.Phys.*, vol. 33, pp. 169–174, 2010.

[102] K. Nakamura *et al.*, "Review of Particle Physics (Particle Data Group)," *J. Phys.*, vol. G 37, 2010.

[103] N. Mackay and S. Penstone, "High sensitivity narrow-band time-domain reflectometer," *IEEE Trans. Instrum. Meas.*, vol. 23, 2, pp. 155–158, 1974.

[104] "http://www.minusk.com,"

[105] G. Ventura *et al.*, "Low temperature thermal conductivity of kevlar," *Cryogenics*, vol. 40, pp. 489–491, 2000.

[106] R. Reed and M. Golda *Cryogenics*, vol. 34, p. 909, 1994.

[107] "http://www.nanopositioning.com,"